THÈSE DE DOCTORAT
DE L'INSTITUT NATIONAL DES SCIENCES APPLIQUÉES DE RENNES

Spécialité :
ÉLECTRONIQUE

Pour obtenir le grade de :
DOCTEUR DE L'INSA DE RENNES

Présentée par :
Anthony BOURGES

Faisabilité d'un radar à ondes de surface sur bouées - Problématique de la déformation du réseau d'antennes et réalisation d'une bouée

Soutenue le :
7 novembre 2008

Devant le jury composé de :

Rapporteurs :	
Pr. Jean-Yves DAUVIGNAC	Université de Nice Sophia Antipolis
Pr. Marc HELIER	Université Pierre et Marie Curie
Examinateurs :	
Pr. Pierre FLAMENT	Université de Hawaii
Dr. Randy HAUPT	Pennsylvania State University
Pr. Raphael GILLARD, co-encadrant	INSA de Rennes
Dr. Régis GUINVARC'H, co-encadrant	SONDRA/Supelec
Pr. Bernard UGUEN, Directeur de thèse	Université de Rennes 1

Remerciements

Ayant effectué ma thèse au sein du laboratoire SONDRA dans d'excellentes conditions, je souhaiterais tout d'abord remercier les quatre partenaires qui en sont à l'origine : la DSTA et NUS pour Singapour, Supélec et l'ONERA pour la France, ainsi que Marc Lesturgie, Directeur du laboratoire.

Merci à M. Pierre Flament, Professeur à l'Université de Hawaii, d'avoir accepté de présider le jury de cette thèse, et à MM. les Professeurs Marc Hélier de l'Université de Pierre et Marie Curie, Paris 6 et Jean-Yves Dauvignac, Professeur à l'Université de Sophia Antipolis d'avoir accepté d'être les rapporteurs de ce manuscrit. Leurs remarques et suggestions lors de la lecture de mon rapport m'ont permis d'apporter des améliorations à la qualité de ce dernier. J'ai été également très sensible à la présence dans ce jury de Monsieur Randy Haupt de l'Université de Pennsylvanie.

J'aimerais aussi remercier chaleureusement MM. Bernard Uguen et Raphaël Gillard, Professeurs à l'Université de Rennes 1 et à l'INSA de Rennes. Qu'ils reçoivent toute l'expression de ma reconnaissance pour m'avoir encadré sur ce sujet de thèse, pour leur dynamisme et leurs compétences scientifiques qui m'ont permis de mener à bien cette étude.

Mon cher Régis, grand maître Shaolin, Breton devant l'Eternel, merci pour ton aide, ta présence quotidienne, ton soutien et ton amitié. Des moments studieux à ceux qui l'étaient un peu moins, de Chichen Itza à Monument Valley, tu m'as beaucoup apporté. Merci pour ces quatre années d'aventure exceptionnelles.

Merci à l'équipe basse fréquence du DEMR de l'ONERA à Palaiseau pour leur aide. Tout particulièrement merci à Gilbert Auffray d'avoir persévéré malgré les retours peu encourageants des premières manips. Merci, à Michel Menelle et à Bruno Urbani pour leur petit séjour sibérien dans les Landes : planter des antennes n'a pas été facile... heureusement, il y avait les travers de porc du Rancho pour nous récompenser de tous ces efforts. Merci à M. Jean-Yves Le Balier pour nous avoir prêté son bateau et à Yann Mourot qui a accepté de braver avec moi les éléments déchaînés de la baie de Perros Guirec.

Merci à toute la famille Flament qui, un soir de juillet 2007, nous a accompagnés jusqu'au bout de la nuit pour coller le premier prototype de bouée. Merci à Fabrice Ardhuin et Louis Marié d'avoir consacré une partie de leur temps libre à nous aider et à la mairie de Porspoder pour leur collaboration. Merci à Mahdi Ben Jelloul pour s'être jeté en mer d'Iroise sauvant notre câble coaxial des eaux glaciales bretonnes.

Merci à toute l'équipe SONDRA. Merci à l'expérimenté Walid pour ses conseils, à Anne-Hélène pour sa bonne humeur et pour son aide, à Laetitia (un seul stade : allez Toulouse!!!) et un grand merci à Jean-Philippe qui, sur quelques secondes, nous a montré toute l'étendue de sa technique footbalistique.

Merci à la "China Jump generation". Merci à Rémi, nouveau sudiste, ancien collègue puis re-nouveau collègue : je crois qu'on est fait pour vivre ensemble. Merci à François, qui d'un regard (ou d'une lourde chute sur son postérieur) peut briser un porte-savon un peu trop arrogant (He loves Guinness but Guinness does not like him). Et bien sur, j'associe à ce duo nos deux compères de l'époque : Fred et Jordi, amis de la première heure avec qui nous avons beaucoup partagé. Merci à vous quatre, aurais-je osé continuer en thèse sans vous ?

Merci à Captain' Karim, aux yeux rougis de Dany, au Grand duc Philippe, à la sagesse de Rami, à la fashion attitude de Fred, à Shuwen et à Yaël. Merci à la Mairie de Bourg-la-Reine d'avoir planté des buissons près de sa gare RER pour que Fredo puisse se ressourcer (on a la contenance qu'on mérite). Fredo, merci de retenir ton digicode... et Merci pour le reste. Merci à ma binôme Chin pour tous ces échanges culturels et gastronomiques. Merci à Jacques, mon jeune padawan et à Marc mon ex-padawan. Merci Gabriele pour cette rigueur défensive italienne que tu as su nous insuffler. Chiara, vivement qu'on se retrouve à Genoa pour siroter une boisson exotique. Merci à Luc pour ses parties de Badminton endiablées. Comment ne pas rajouter à cette liste ce cher Albert, propriétaire chaleureux du bar du Guichet, qui, grâce à son savant dosage des Picon bières, a su apporter à toute l'équipe un peu de chaleur.

Merci aux nombreux intervenants de la pause café de Supélec.

Merci, aux piliers de la FES (Fédération Epicurienne de Sule), à leur bonne humeur et à leur générosité festive. Merci à Gladine, au Temps des Cerises, à la Peña Feytaire et à l'Aviron Bayonnais. Merci à Mamadou Niang.

Merci à toute ma famille et plus particulièrement à Gégé et à Evelyne, mes fidèles parents et bien sur merci à Fanny, à Marie-Noëlle et à Christian qui ont toujours été derrière moi. Merci à ma douce Julie pour son soutien quotidien. Tu as toujours été présente, même dans les moments difficiles.

Résumé étendu

Introduction

Le radar Hautes Fréquences (HF) à ondes de surface permet de détecter des bateaux à de grandes distances. Il utilise la propagation des ondes le long de la surface de la mer pour détecter des cibles au-delà de l'horizon.

Figure 1: Un réseau de réception côtier d'un radar HFSWR.

Ce radar est idéalement utilisé pour la surveillance maritime des eaux côtières à des distances supérieures à 200 km ou pour la mesure de paramètres océanographiques. Un réseau de réception conventionnel est représenté en Fig. 1.

La thèse présente un nouveau concept de radar HF où le réseau de réception est placé sur des bouées en mer. Cette nouvelle approche permet de déployer des réseaux de plus grandes dimensions pour améliorer les performances de détection du radar.

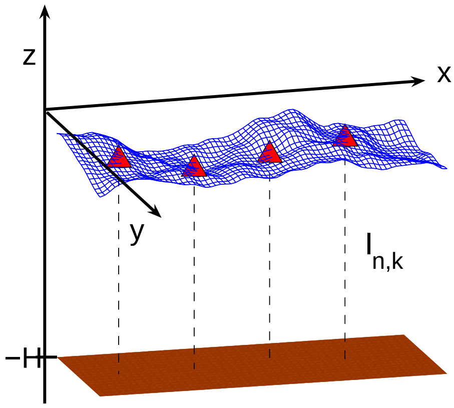

Figure 2: Réseau de réception sur bouées en mer.

Les problématiques afférentes sont évoquées dans le premier chapitre de cette thèse.

Dans le chapitre 2, ce nouveau concept de réseau de réception flottant est présenté en définissant notamment les notions de réseau déformé et non déformé. Le réseau non déformé est utilisé comme référence pour quantifier les perturbations du diagramme de rayonnement associé au réseau déformé, le réseau déformé étant défini comme le réseau flottant sur bouées. Un modèle numérique simple permettant de calculer le mouvement d'une bouée sur une surface de mer discrétisée sera également présenté. Il garantit une corrélation entre la forme de la surface de mer et le mouvement de la bouée.

Dans le chapitre 3, nous étudierons le réseau de réception avec déformations. Les différentes sources de perturbations seront présentées en fonction du type de déplacement (vertical le long de l'axe des z et horizontal le long des axes x et y). Des méthodes de corrections seront ensuite proposées qui consistent en une modification du jeu de poids d'excitation du réseau.

Une étude de la robustesse des algorithmes de détection de directions d'arrivée sera réalisée dans le chapitre 4 en fonction de la déformation du réseau de réception.

Pour finir, une expérimentation avec une antenne flottante est présentée dans le chapitre 5. Elle vise à valider, outre la faisabilité de la mesure, l'allure du signal reçu. En effet, celui-ci pourrait être modulé par les mouvements de la mer.

CHAPITRE 1

Le premier chapitre apporte un certain nombre d'informations sur les différents domaines abordés pour cette étude : les radars HFSWR et leurs applications, les réseaux d'antennes phasés, l'utilisation d'une bouée comme nouveau support d'antenne pour le réseau de réception.

Une deuxième partie évoque les applications possibles d'un tel radar. On distingue deux grands domaines. Le premier concerne la détection de cible dans le cadre de la surveillance de vastes zones maritimes. Le second est la mesure de paramètres océanographiques comme la vitesse du vent, des courants etc... Plusieurs exemples sont donnés dans ce chapitre.

Les radars HFSWR requièrent un déploiement du réseau de réception le long de la côte, près de la mer pour permettre une bonne excitation de l'onde de surface. De plus, pour avoir une bonne précision en détection angulaire, son réseau de réception doit être le plus large possible. Comme le radar travaille dans la bande HF (3-30 MHz), sa longueur d'onde est égale à plusieurs centaines de métres et son réseau de réception est donc de grande dimension.

Un des problèmes rencontrés lors du déploiement d'un tel radar et (particuliérement avec son réseau de réception) est de trouver un emplacement le long de la côte suffisamment large pour l'accueillir.

Une solution alternative au réseau classique est de déplacer le réseau de réception du radar sur des bouées en mer (cf Fig. 2.8). Ainsi, l'emplacement du radar peut être trouvé plus facilement. Malheureusement ce nouveau type de déploiement génère de nouveaux problèmes liés à la déformation du réseau par le mouvement de la mer.

Cette thèse propose une étude de ce nouveau concept. Les perturbations générées par les déformations du réseau seront étudiées. Des méthodes spécifiques de correction pour limiter leurs effets seront ensuite présentées.

CHAPITRE 2

Définition du système : réseau déformé et non déformé

Le réseau non déformé est un réseau régulier composé de N éléments avec un espace interélément de $\lambda/2$, λ étant la longueur d'onde de fréquence de fonctionnement f. Il est disposé le long de l'axe des x.

Nous supposons par ailleurs que chaque antenne est disposée sur une bouée flottant sur la mer. Chaque bouée est ancrée au fond de la mer avec un câble à une profondeur H de la surface de mer de référence (cf Fig. 2 et Fig. 4).

Le réseau déformé est le résultat des mouvements de la mer. Ces mouvements génèrent des perturbations dans le diagramme de rayonnement.

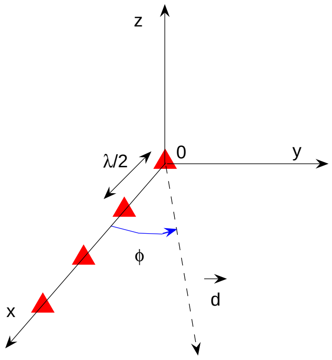

Figure 3: Réseau non déformé.

Modélisation de la surface de mer

Les déplacements des bouées sont calculés à partir d'une modélisation réaliste de la mer.

état de mer	Description	hauteurs typiques des vagues (m)
0	Calm	0
1	Smooth	0 to 0.3
2	Slight	0.3 to 0.9
3	Moderate	0.9 to 1.5
4	Rough	1.5 to 2.4
5	Very Rough	2.4 to 3.6
6	High	3.6 to 6
7	very High	6 to 12
8	Precipitous	12

Table 1: Echelle de Douglas

Les surfaces de mer sont ainsi générées à partir des spectres de mer de Pierson Moskovitz [28]. Différents spectres peuvent être choisis suivant une hauteur de vagues typique. L'échelle de Douglas les classifie en fonction des différents états de mer (cf Table 2.1).

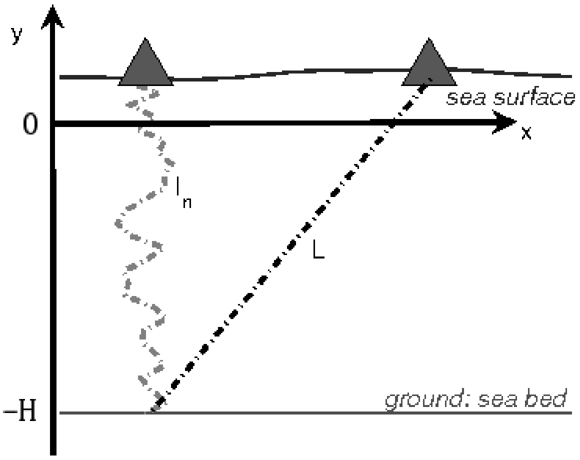

Figure 4: Définition de L, la longueur du câble.

Les surfaces de mer sont de plus calculées pour générer des corrélations entre deux pas temporels successifs. Tous ces éléments sont donnés dans la toolbox Matlab WAFO [14].

Déplacement des bouées

Dans cette partie du chapitre, un algorithme simple est proposé permettant de calculer les différentes positions de la bouée sur la mer. Ces positions sont déduites de la forme de la surface de mer.

Cet algorithme permet de modéliser le déplacement des bouées à partir de la matrice des hauteurs de vagues de la surface de mer et il est utilisé pour quantifier les perturbations générées par le réseau déformé. Il a été précédemment démontré dans [11] et [10] que les mouvements de bouées altèrent les diagrammes de rayonnement. Pour compenser ces problèmes, une méthode de correction a été développée et est présentée dans le chapitre suivante. Nous supposons que les mouvements horizontaux sont négligeables et nous concentrons notre étude sur les déplacements verticaux.

Un exemple de déplacement d'antennes est donné en Fig. 2.10. Elle montre l'évolution temporelle de la bouée autour de sa position initiale.

CHAPITRE 3

Le chapitre 3 présente les perturbations générées par la déformation du réseau (avec un déplacement vertical et horizontal) et leurs méthodes de correction associées.

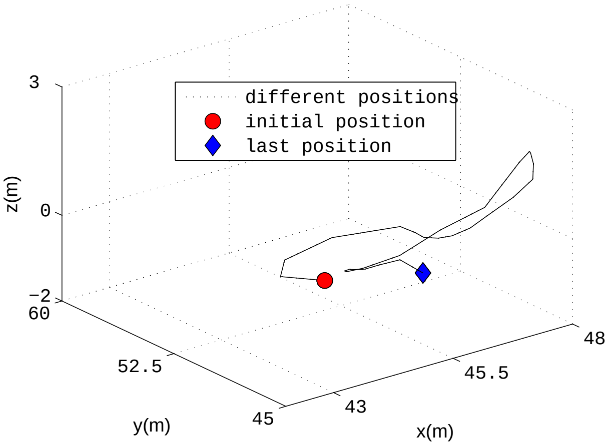

Figure 5: Exemple de déplacement d'antenne.

Réseau de réception avec une déformation verticale

Dans cette partie, les différents éléments du réseau de réception sont des dipôles verticaux. Dans le déplacement vertical [11], les principales perturbations proviennent de la modification du couplage dans le réseau quand les dipôles bougent verticalement.

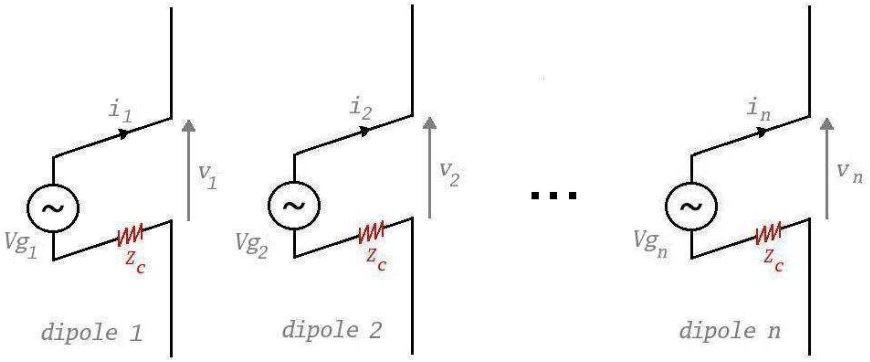

Figure 6: Représentation du couplage d'un dipôle.

$I = [\ i_1,\ i_2,\ \ldots,\ i_N\ ]^T$ est défini comme le vecteur de courants du port de l'antenne qui produit le diagramme de rayonnement désiré (cf Fig. 3.9). La tension $V_g = [\ v_{g1},\ v_{g2},\ \ldots,\ v_{gN}\ ]^T$ peut alors être définie comme :

$$V_g = (Z + Z_g I_d)\, I \tag{1}$$

où Z_g est l'impédance de la source, Z est la matrice impédance (représentant le couplage) et I_d la matrice identité. La connaissance de Z permet alors de calculer les bons coeeficients. Pour simplifier, dans l'exemple suivant, Z est construite comme l'impédance mutuelle de deux dipôles en espace libre pour différents décalages verticaux entre les antennes [23].

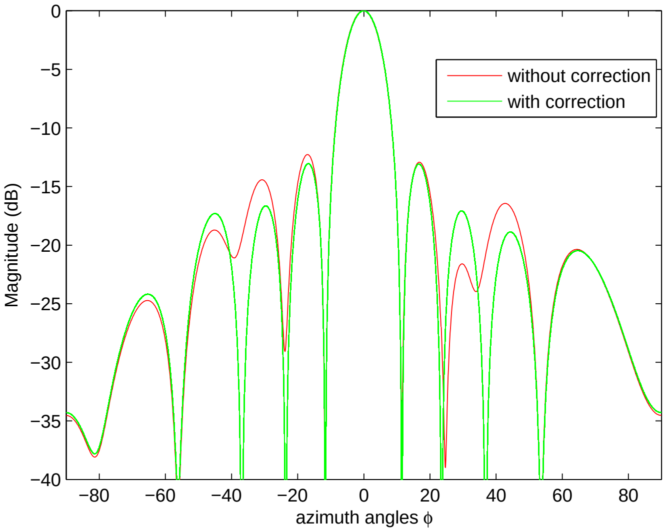

Figure 7: Diagramme de rayonnement d'un réseau uniforme de 10 antennes avec une déformation verticale, avec et sans correction.

La figure 3.10 montre l'effet de la méthode de correction sur un réseau de 10 éléments. Elle compare le diagramme de rayonnement obtenu pour deux tensions différentes V_g. Le cas sans correction correspond à un réseau où les coordonnées de l'antenne sont différentes mais V_g est calculé en utilisant la matrice Z du réseau non déformé.

Le cas avec correction correspond au même réseau mais il est maintenant utilisé avec la matrice Z du réseau déformé. Comme nous l'avons vu, la méthode de correction permet une décroissance significative des lobes secondaires.

Réseau de réception avec une déformation horizontale

En considérant une déformation du réseau d'antennes avec des mouvements horizontaux, le problème est un peu différent. On se place tout d'abord dans le cas d'une déformation longitudinale (le long de l'axe du réseau (O, x)). Les principales perturbations ne résultent pas de la modification du couplage mais de la modification de l'espacement inter élément dans le réseau. Le réseau déformé peut être vu comme un réseau linéaire avec un espacement non régulier entre les éléments. Le couplage est un deuxième effet qui peut être corrigé par la méthode présentée dans la partie précédente. Celle-ci ne sera pas discutée à nouveau ici.

Méthodes de compensation pour la déformation longitudinale

Nous supposons que les positions des antennes sont parfaitement connues. Le principe de la méthode consiste à pondérer les changements des espacements inter éléments par une modification des poids d'excitation. Haupt a étudié le problème réciproque en [17].

Pour la suite, i_n est le courant de l'antenne n pour un réseau non déformé et $\tilde{i_n}$ est le coefficient correspondant utilisé pour le réseau déformé. Les compensations peuvent se résumer en forçant les coefficients pour lesquels les nuls du diagramme de rayonnement correspondent à ceux du réseau non déformé. Un système linéaire est alors obtenu :

$$\sum_{n=1}^{N} \tilde{i}_n e^{jk\tilde{x}_n u_m} = \sum_{n=1}^{N} i_n e^{jkx_n u_m} \quad m = 1, ..., N-1 \tag{2}$$

où $u_m = \cos\phi_m$ et ϕ_m est l'angle azimut du nul m dans le diagramme de rayonnement. Eq. 3.9 représente un système linéaire de $N-1$ équations pour N inconnues. Nous choisissons arbitrairement $\tilde{i}_N = 1$ pour fixer le niveau de proportionnalité de tous les poids $\tilde{i}_n$. Eq. 3.10 est le nouveau système linéaire qui doit être résolu :

$$\sum_{n=1}^{N-1} \tilde{i}_n e^{jk\tilde{x}_n u_m} = \sum_{n=1}^{N} i_n e^{jkx_n u_m} - e^{jk\tilde{x}_N u_m} \quad m = 1, ..., N-1 \tag{3}$$

Eq. 3.10 peut être réécrite avec les représentations matricielles suivantes avec $\tilde{X}_1 = [\ \tilde{x}_1\ \tilde{x}_2\ \ldots\ \tilde{x}_{N-1}\ ]$.

$$\tilde{E}\tilde{I}_1 = EI - A \tag{4}$$

avec

$$U = [\ u_1\ u_2\ \ldots\ u_{N-1}\ ]^T \tag{5}$$

$$E = \exp(jkUX) \tag{6}$$

$$\tilde{E} = \exp\left(jkU\tilde{X}_1\right) \tag{7}$$

où $\tilde{I}_1 = \left[\ \tilde{i}_1\ \tilde{i}_2\ \ldots\ \tilde{i}_{N-1}\ \right]^T$ et $A = \left[\ e^{jk\tilde{x}_N u_1}\ e^{jk\tilde{x}_N u_2}\ \ldots\ e^{jk\tilde{x}_N u_{N-1}}\ \right]^T$. Comme I est connu, nous pouvons facilement calculer $\tilde{I}_1$ avec Eq. 3.15.

$$\tilde{I}_1 = \tilde{E}^{-1}\left(EI - A\right) \tag{8}$$

$\tilde{I}$, qui correspond à tous les poids de la méthode de correction, peut être facilement calculé :

$$\tilde{I} = [\tilde{I}_1^T, 1]^T \tag{9}$$

Dans la partie suivante, la méthode de correction est étendue aux mouvements longitudinaux et transverses.

Méthodes pour la déformation longitudinale et transverse

Les corrections des mouvements transverses et longitudinaux peuvent être réalisées simultanément. Un nouveau système linéaire est alors défini (Eq. 3.17) :

$$\sum_{n=1}^{N} \tilde{i}_n e^{jk(\tilde{x}_n u_m + \tilde{y}_n u'_m)} = \sum_{n=1}^{N} i_n e^{jk x_n u_m} \quad m = 1, ..., N-1 \tag{10}$$

avec $u'_m = \sin\phi_m$.

Pour des déformations longitudinales, le réseau déformé résultant est un réseau linéaire non régulier. Avec les deux déformations longitudinales et transverses, le réseau n'est plus linéaire. Eq. 3.17 est utilisée pour obtenir des nuls dans le diagramme de rayonnement avant ($\phi \in [0, \pi]$). Aucun contrôle sur le diagramme arrière n'est possible, ce qui n'est pas un problème pour nos applications en radar HF. Une nouvelle expression de u'_m est définie :

$$U' = [\ u'_1\ u'_2\ \ldots\ u'_{N-1}\ ]^T \tag{11}$$

La nouvelle matrice $\tilde{E}$ est donnée par :

$$\tilde{E} = \exp\left(jk\left(U\tilde{X}_1 + U'\tilde{Y}_1\right)\right) \tag{12}$$

avec $\tilde{Y}_1 = [\ \tilde{y}_1\ \tilde{y}_2\ \ldots\ \tilde{y}_{N-1}\ ]$ et les courants utilisés par les équations 3.15 et 3.16 où A est maintenant défini par $A = \left[\ e^{jk(\tilde{x}_N u_1 + \tilde{y}_N u'_1)}\ e^{jk(\tilde{x}_N u_2 + \tilde{y}_N u'_2)}\ \ldots\ e^{jk(\tilde{x}_N u_{N-1} + \tilde{y}_N u'_{N-1})}\ \right]^T$. En utilisant cette formulation, un exemple est donné dans la partie suivante.

Résultat pour la méthode de correction horizontale

Trois déplacements sont présentés (générant plus ou moins de perturbations dans le réseau de réception) correspondant à trois états de mer différents (leurs valeurs étant 1, 3 et 6).

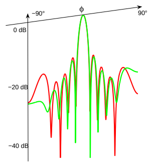

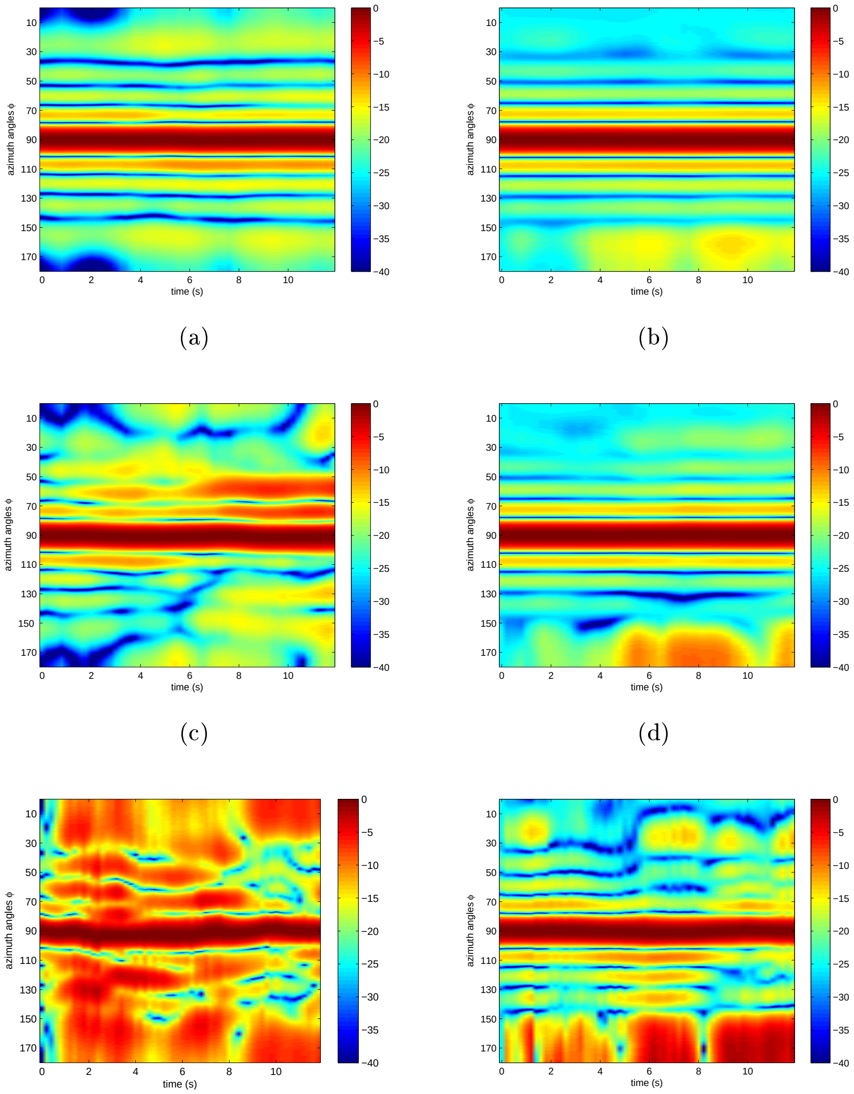

(a) (b)

(c) (d)

(e) (f)

Figure 8: Diagramme sans correction (a) (c) (e) et avec correction (b) (d) (f) pour un état de mer 1: (a) et (b), état de mer 3: (c) et (d), état de mer 6: (e) et (f)

La figure 3.15 représente le diagramme de rayonnement en fonction du temps avec et sans correction. Pour une plus grande clarté, la figure 3.16 représente le même

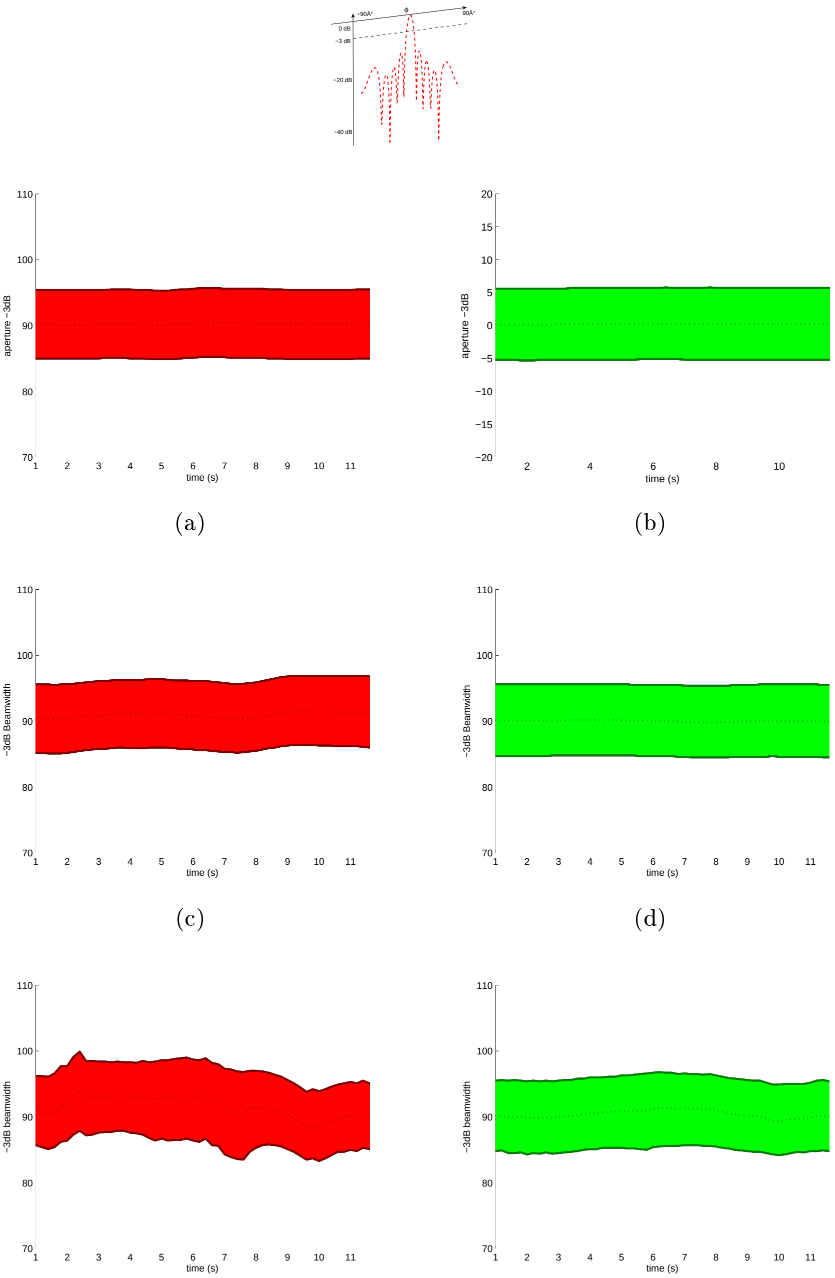

(a) (b)

(c) (d)

(e) (f)

Figure 9: Seuillage du diagramme de rayonnement au-dessus de -3 dB (direction du lobe principale et ouverture à -3 dB): sans correction (a) (c) (e) et avec correction (b) (d) (f) pour un état de mer 1: (a) and (b), état de mer 3: (c) et (d), état de mer 6: (e) et (f)

diagramme de rayonnement quand un seuil à -3 dB est appliqué. Il permet de visualiser la direction du lobe principal et l'ouverture à -3 dB avec et sans correction.

- Pour un état de mer de 1, la mer est lisse (cf Tableau 2.1) et les déformations dans le réseau sont faibles. Le niveau de lobe secondaire augmente dans des directions spécifiques de ϕ (cf Fig. 3.15 (a)). Le lobe principal n'est pas affecté par le mouvement de la mer (cf Fig. 3.16 (a)).

- Pour un état de mer de 3, la mer est modérée et les mouvements génèrent de fortes perturbations dans le diagramme de rayonnement (cf Fig. 3.15 (b)). Les niveaux de lobes secondaires augmentent jusqu'à -6.6 dB (à t=10 s). Pour cet état de mer, le lobe principal n'est pas significativement affecté (cf Fig. 3.16 (b)).

- Pour un état de mer de 6, les perturbations dans le diagramme de rayonnement sont importantes (cf Fig. 3.15 (c) and 3.16 (c)). La direction du lobe principal change significativement et le niveau de lobes secondaires peut être très haut (par exemple, on observe un niveau de lobe secondaire jusqu'à -2.4 dB, à t=10 s).

Cependant, notre méthode de correction a conservé la direction de notre lobe principal et son ouverture à -3 dB (10° avec une direction principale égale à 0° en Fig. 3.16 (b) (d) (f)) comparé aux résultats sans correction (plus de 12° de largeur de lobe principal, sa direction variant de ±5°) et ce quelque soit l'état de mer (jusqu'à 6).

La méthode de correction réduit de plus les niveaux de lobes secondaires pour $[0, \phi_{N-1}[$ (avec un réseau de $N = 10$ antennes, $\phi_{N-1} = 60°$).

Pour ϕ plus large que ϕ_{N-1}, la méthode de correction n'est plus valide. Comme illustration, Fig. 3.18 donne une coupe des résultats obtenus pour $t = 2$ s et un état de mer de 4. In $[0, \phi_{N-1}[$, le niveau maximum des lobes secondaires est égal à -12.59 dB, au lieu de -13 dB pour un réseau non déformé et -9 dB pour $[\phi_{N-1}, \pi]$.

Une méthode a été présentée permettant de corriger les déplacements verticaux et horizontaux d'antennes. La méthode de correction verticale utilise à la connaissance des modifications de la matrice de couplage. La méthode de correction horizontale repose sur le forçage des nuls dans le diagramme de rayonnement d'un réseau déformé, le but étant d'obtenir les mêmes zéros que ceux du réseau non déformé.

Ces méthodes permettent de réaliser des compensations en temps réel de réseau d'antenne de HFSWR déformé. Elles diminuent les lobes secondaires qui apparaissent lorsque le réseau se déforme.

Une comparaison avec des méthodes itératives a montré que, si ces dernières donnent des résultats sensiblement meilleurs, leur temps de calcul est incommensurablement supérieur.

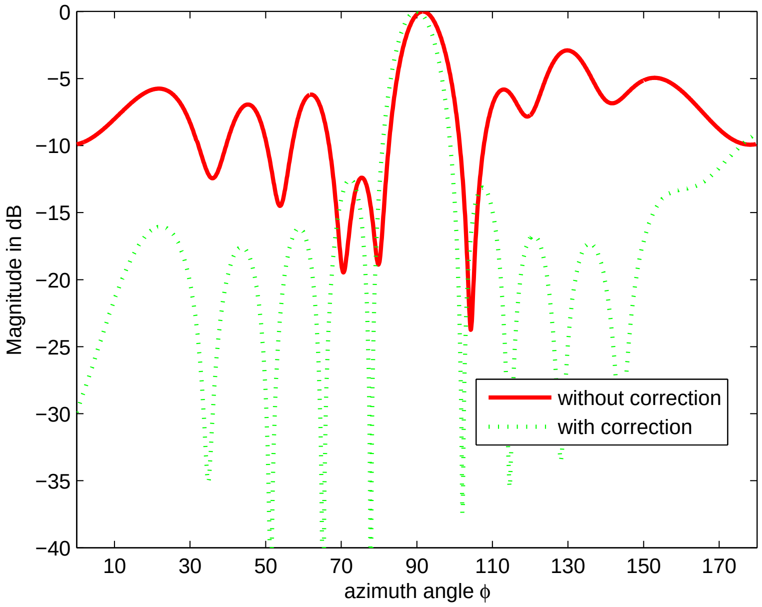

Figure 10: Diagramme de rayonnement avec et sans correction pour un état de mer de 4

CHAPITRE 4

Le chapitre 4 traite de l'estimation de la direction d'arrivée à partir de réseaux d'antennes déformables.

La localisation d'une cible passe par un procédé de traitement d'antenne. Celui-ci permet, à partir des signaux reçus, d'extraire un certain nombre d'informations sur la cible, notamment sa direction d'arrivée (DOA, Direction Of Arrival). De nombreux algorithmes ont été développés en ce sens depuis une trentaine d'années. Le plus connu d'entre eux est certainement l'algorithme MUSIC (ou Multiple Signal Classification). Il permet de déduire les directions d'arrivée de signaux émis par des cibles en extrayant des propriétés de la matrice de corrélation de ces mêmes signaux reçus sur une antenne réseau. Développé pour des antennes dont la position de chaque capteur est connue, il est intéressant de tester sa robustesse sur des antennes dont la position des capteurs n'est pas connue de manière exacte, mais avec une certaine erreur : ceci correspond à notre application, avec une antenne flottante sur une bouée en mer et équipée d'un récepteur de type GPS (l'erreur de position de chaque capteur serait alors égale à l'erreur de précision de la localisation offerte par un tel système).

Dans ce résumé, l'algorithme MUSIC ne sera pas développé. Une série de simulations permettront toutefois d'en tester la robustesse aux erreurs de position des capteurs d'une antenne réseau.

Le programme mettant en oeuvre l'algorithme MUSIC, effectue plusieurs tirages aléatoires des erreurs de position des capteurs (pour une variance donnée). Il donne comme résultat une courbe du pourcentage de détection d'une ou plusieurs cibles en fonction de l'amplitude des déformations.

L'algorithme de Weiss-Friedlander

La méthode de Weiss-Friedlander est basée sur MUSIC en y ajoutant la boucle de double convergence de l'estimation des DOA et de la position des capteurs de l'antenne réseau.

Simulation et résultat

Performances de l'algorithme MUSIC

L'algorithme MUSIC permet d'obtenir un spectre sur lequel la recherche de maxima aboutit à la détection de cibles et à l'obtention de leur direction d'arrivée. Si la détection est optimale et efficace pour une antenne fixe dont la géométrie est parfaitement connue, elle est fortement dégradée lorsque la position des capteurs est approximatif.

Il est donc intéressant de quantifier les limites de fonctionnement de l'algorithme MUSIC en fonction de la déformation du réseau d'antenne. Pour cela, nous allons faire varier l'amplitude des déformations du réseau en faisant varier la variance de la loi normale servant aux tirages aléatoires des erreurs de position. De plus, pour chaque variance, nous allons réaliser 200 tirages aléatoires, afin de moyenner les résultats. Ensuite, nous représenterons l'évolution des détections en fonction des amplitudes des erreurs, représentées par Δr.

Impact de la taille du fenêtrage sur la détection de cibles Le recours à un fenêtrage, même large, permet d'améliorer sensiblement la capacité de détection de l'algorithme. Cette réduction du spectre angulaire à analyser peut être réalisée par une autre méthode de détection de direction d'arrivée, plus grossiére, comme la formation de voie utilisée avant MUSIC. Elle permet de restreindre le spectre angulaire à analyser à un écart angulaire autour de la DOA cherchée.

Pour la suite des simulations de l'algorithme MUSIC, le fenêtrage sera pris à 20°.

Impact du nombre de cibles à détecter Dans le cadre applicatif de notre étude, les limites de l'algorithme MUSIC sont atteintes relativement rapidement. En effet, si l'on veut détecter un nombre important de cibles à tous les coups, les déformations du réseau (non connues de MUSIC) doivent être minimes, c'est à dire en dessous du mètre pour chaque capteur.

Détection de cibles proches Cette étude montre que plus les cibles sont proches, plus les déformations du réseau d'antennes ont un effet dégradant sur la distinction des cibles.

Il semblerait donc que MUSIC soit relativement robuste aux déformations du réseau par rapport à sa capacité à distinguer des cibles proches. Il faut néanmoins nuancer ce constat : le continuum angulaire de précision $0,1°$ utilisé pour les simulations de MUSIC équivaut à un calibrage d'antenne suivant 1800 directions (spectre angulaire $[-90°;90]$ avec un pas de discrétisation de $0,1°$). En pratique, un nombre plus restreint de directions est utilisé pour calibrer les antennes.

Améliorations apportées par la méthode de Weiss-Friedlander

L'algorithme de Weiss-Friedlander trouve de manière itérative une estimation de la position réelle des capteurs et des directions d'arrivée des cibles. Il est habituellement appliqué comme traitement d'antenne lorsque les déformations du réseau sont petites et plus ou moins corrélées entre chaque capteur (déformations du réseau en arc de cercle par exemple). Il est intéressant, dans le cas de notre étude, d'observer son comportement pour des déformations d'ordre aléatoire sur chaque capteur.

On remarque une convergence de l'algorithme, qui se fait de manière plus précise pour de faibles erreurs de position des capteurs. Néanmoins, la convergence n'est pas totale, c'est à dire que la position estimée des capteurs est légérement différente de la positon réelle, même si la forme générale de l'antenne est bien retranscrite.

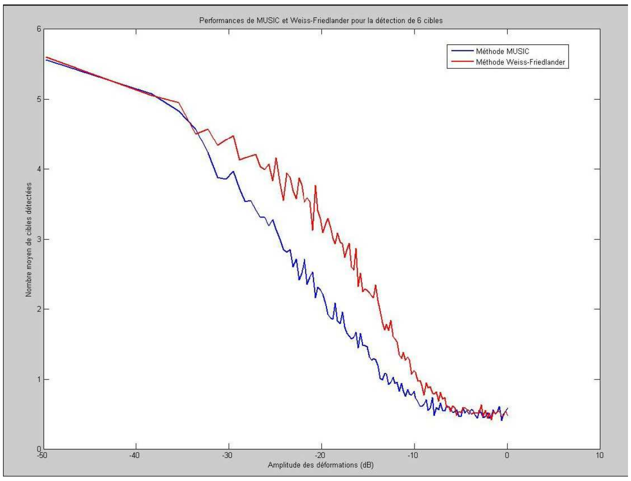

Figure 11: Robustesse de MUSIC et Weiss Friedlander pour une detection de 6 cibles (DOA égales à 30°, 60°, 80°, 100°, 130° and 160°)

La Fig. 4.13 permet d'analyser les améliorations de cette méthode par rapport à l'algorithme MUSIC. Elle représente le nombre moyen de cibles détectées pour 6 cibles présentes en fonction de l'amplitude de la déformation de l'antenne réseau, et ceci pour l'algorithme MUSIC sans fenêtrage et pour la méthode Weiss-Friedlander (qui ne fait pas non plus intervenir de fenêtrage dans sa partie algorithmique faisant référence à MUSIC).

Des améliorations sont nettement présentes. La méthode de Weiss-Friedlander apporte donc de meilleures performances dans une plage d'erreur qui correspond à notre cas pratique (erreurs de quelques métres).

Conclusion des méthodes de détection de DOA

L'étude menée a permis de tester la robustesse de deux algorithmes de traitement d'antenne dans le but de détecter la direction d'arrivée des cibles. L'application envisagée, à savoir un réseau d'antenne sur bouées en mer, requière la possibilité de détecter un nombre important de cibles à des distances lointaines.

Au terme des simulations effectuées durant la thése, il apparaît que l'algorithme MUSIC seul ne peut fournir de bonnes performances en terme de détection. Il nécessite une amélioration de ses performances, fournies par deux méthodes présentées dans ce rapport.

La premiére consiste à restreindre la zone angulaire pour la recherche de cibles par MUSIC, ce qui peut être effectué par un autre procédé de détection, comme la formation de voie. La seconde consiste en la méthode de Weiss-Friedlander qui améliore la détection de cibles par rapport à MUSIC en donnant une estimation de la position des capteurs de l'antenne réseau.

CHAPITRE 5

Dans les chapitres précédents, nous avons vu que les mouvements d'antennes dégradent les digrammes de rayonnement. Le deuxiéme problème introduit par le mouvement est relatif à la modulation du signal de réception sur l'antenne flottante. En fait, le déplacement de chaque antenne élémentaire sur la mer, indépendamment de la déformation du réseau génère des modulations dans le signal de réception, introduisant un étalement des raies de Bragg.

De nombreuses études théoriques ont été menées sur ce sujet. Ce chapitre présente une expérimentation avec une antenne flottante, menée sur la pointe de la Garchine en Bretagne.

Ce site breton a été choisi car un radar HFSWR de type WERA y est déjà opérationnel pour la mesure de courants de surface en mer d'Iroise. Le but est d'utiliser les infrastructures existantes de ce radar, c'est à dire toute la partie émission et toute la partie acquisition des signaux de réception.

En supprimant une des antennes du réseau de réception, une entrée du radar devient libre et il est donc possible de récupérer le signal de la bouée flottante en reliant son antenne avec le système d'acquisition du radar.

Le site

Le site est un terrain militaire où le SHOM (Service Hydrographique et Océanographique de la Marine) en collaboration avec Actimar et les sociétés Helzel (Hambourg, Allemagne) et Seaview (Sheffield, Royaume-Uni), a déployé un radar HF WERA, au cours de l'été 2006. Actimar met en oeuvre ces deux radars et assure leur maintenance pour un fonctionnement opérationnel.

Descriptif du matériel utilisé

Le radar WERA Le WERA est un radar développé par l'Université de Hambourg pour des mesures océanographiques. C'est un radar qui a :

- un réseau de 16 antennes en réception
- 4 antennes en émission : les quatre antennes d'émission permettent de former un faisceau principal vers la mer tout en protégeant le réseau de réception dans un des deux zéros du diagramme de rayonnement.

Choix de l'antenne de réception L'antenne de réception utilisée est de type Rhode et Shwarz. C'est une antenne active qui doit donc être alimentée et qui a par ailleurs l'avantage d'être compacte.

Choix de la bouée L'installation d'une premiére bouée est nécessaire pour limiter les efforts générés par la houle sur le câble. L'antenne ne sera pas directement reliée à cette bouée mais à une plate-forme flottante (un zodiac de petites dimensions) qui est elle-même attachée à la bouée.

La Fig. 5.3 présente le système flottant (bouée + plate-forme flottante). Des photos de la plate-forme sont présentées en Fig. 5.10. Elles représentent une boite hermétique qui abrite tout l'électronique embarqué sur un petit zodiac.

Le GPS RTK Pour avoir une bonne précision du mouvement de l'antenne flottante en mer, un GPS doit être fixé sur la plate-forme flottante. Pour une précision décimétrique ou centimétrique, un GPS type RTK doit être utilisé.

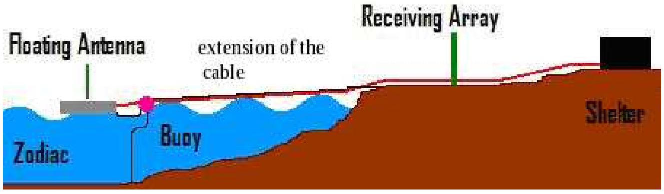

Figure 12: Bouée et plate-forme flottante

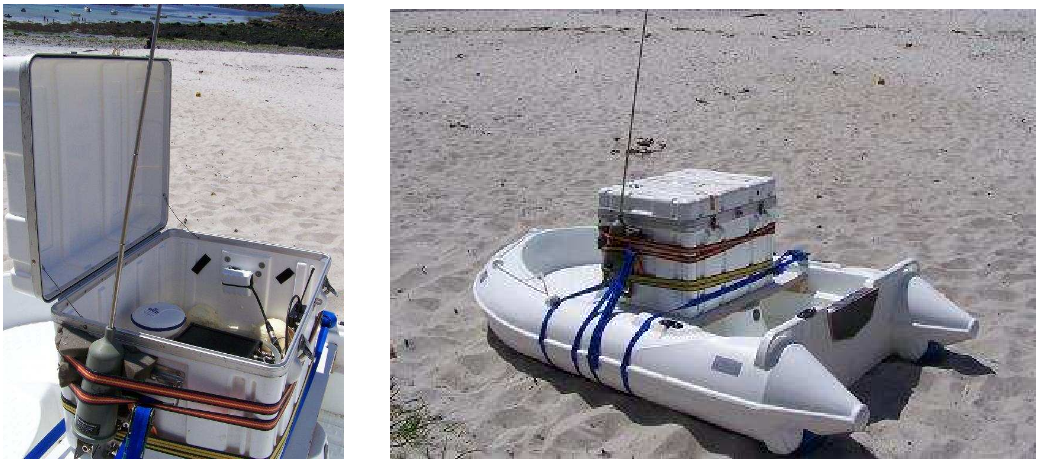
(a) (b)

Figure 13: (a) la boite hermétique et (b) le zodiac.

Le GPS était composé de deux éléments. Un premier élément nommé “base” qui reste en référence sur la côte et un second nommé “mobile” qui est embarqué sur la plate-forme flottante. Ces deux éléments communiquent en permanence pour affiner la position de l’antenne flottante. A ce GPS, il faut associer une central inertielle qui permet de mesurer le roumis et le tangage de la structure flottante.

Résultat de l’expérimentation

Dans un premier temps, nous nous intéressons au mouvement de la bouée mesurée par le GPS RTK pour quantifier son déplacement maximum.

Positions de l’antenne flottante Les figures 5.13 et 5.14 montrent la latitude et la longitude en degré de l’antenne flottante, mesuré par le GPS RTK pendant toute l’acquisition, à partir du départ de la plage la plus proche jusqu’à son retour sur cette même plage. Elle montre clairement que la bouée est restée dans un périmétre de 10 m ×10 m pendant les quatre heures qu’ont duré l’acquisition.

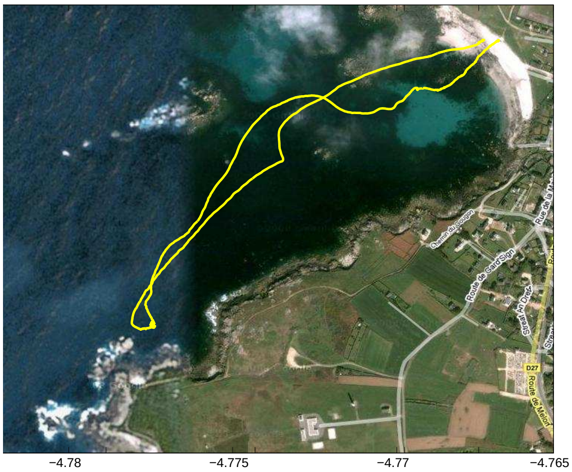

Figure 14: Latitude et longitude de la bouée flottante pendant toute l'acquisition.

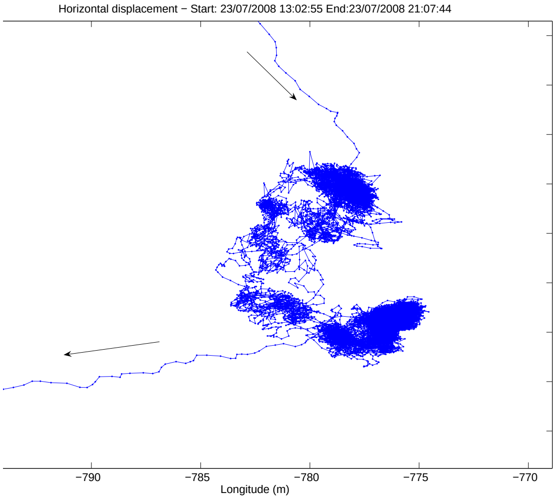

Figure 15: Positions de la bouée autour de son point d'ancrage.

Fig. 5.15 représente l'altitude de la bouée pendant cette même acquisition. Le temps de référence à t=0h correspond à la mise en marche du GPS embarqué. A la fin de l'installation de la bouée (t=3h), la courbe devient lisse. C'est à ce moment que l'enregistrement des signaux a commencé. L'évolution de l'altitude correspond à l'effet de la marée qui n'a cessé d'augmenter durant tout l'enregistrement des signaux. Son

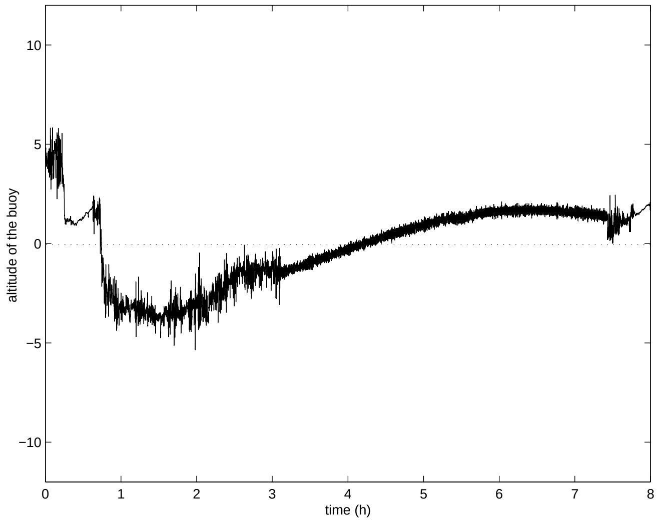

Figure 16: Altitude de la bouée pendant toute l'acquisition.

déplacement vertical est de moins de 1 m.

De la même façon, le roulis et tangage sont présentés. Leurs variations restent faibles (±5°). Ce point est hautement intéressant pour notre problème car cela implique que la modulation du signal ne doit pas être importante.

Mesures Radar avec l'antenne flottante

Deux acquisitions ont été réalisées avec les paramètres standards du radar à une fréquence centrale de 12.48 MHz. La représentation Range Doppler de l'antenne flottante est tracé en Fig. 5.17. Le signal de l'antenne 15 est également représenté comme référence.

Premièrement, la comparaison des deux signaux montre que le signal de l'antenne flottante a amplitude moins importante que celui de l'antenne 15. On remarque de plus que les raies de Bragg du premier ordre et la raie en zéro sont présentes comme prévu. La Fig. 5.18 montre une coupe à 70 km de ces deux résultats en ajoutant les signaux de l'antenne 1. La différence d'amplitude entre l'antenne 15 et l'antenne 1 est importante.

Le rapport entre le signal (défini comme le maximum de la raie de Bragg négative) et le clutter (défini comme le signal en dehors des raies de Bragg) est d'environ 25 dB pour l'antenne 1 et 15 et de 15 dB pour l'antenne flottante. On trouve également 8 dB d'atténuation du clutter entre l'antenne 1 et l'antenne 15. Le shelter est en fait situé plus près de l'antenne 1 que de l'antenne 15. L'écart entre les deux signaux s'explique en considérant l'ajout d'un câble pour couvrir la distance manquante.

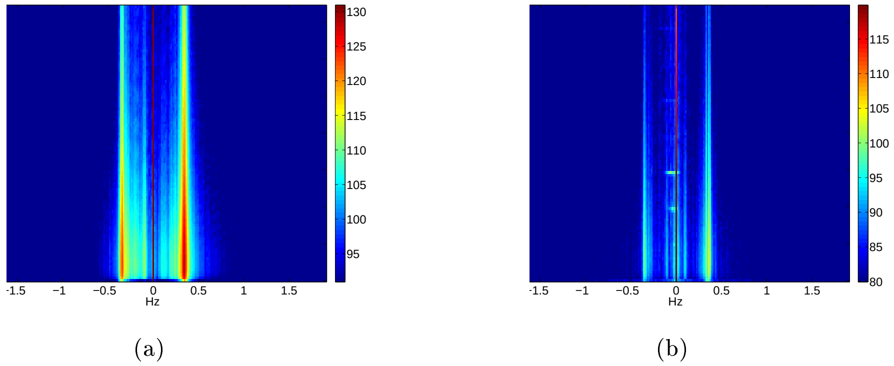

(a) (b)

Figure 17: Représentation en Range Doppler (a) de l'antenne 15 et (b) de l'antenne flottante.

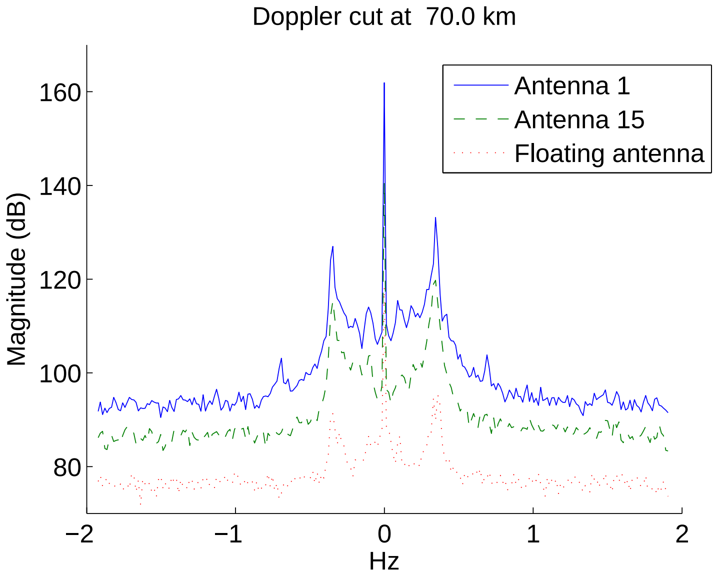

Figure 18: Représentation en Doppler à 70km pour l'antenne 1, l'antenne 15 et l'antenne flottante.

L'antenne flottante a 14 dB de différence d'amplitudes avec le clutter de l'antenne 15 et 22 dB avec les raies de Bragg. Une fois encore, le câble explique cette différence : 300 m de câbles ont été rajoutés pour relier l'antenne flottante et l'antenne 16.

Ce cable ayant une atténuation de 12 dB (1.2 dB pour 100 pieds dans un câble RG 213 à 30 MHz), il y a également quelques métres supplémentaires entre l'antenne 15 et 16. Mais ces remarques n'expliquent pas les pertes du signal par rapport au clutter.

Lors de la mise en place du câble sur l'eau, les connexions de l'antenne flottante n'ont pas été proprement réalisées : le connecteur du câble s'est oxydé. Une autre raison possible est que nous n'avons pas eu le temps de vérifier si le signal de l'antenne flottante n'était pas inférieur au niveau de bruit du radar.

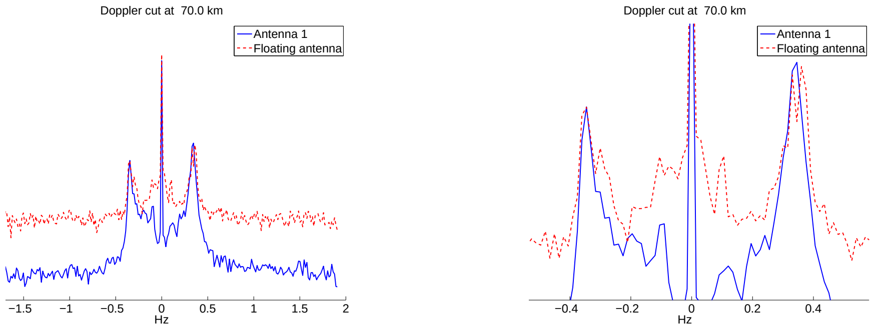

(a) (b)

Figure 19: (a) Coupe Doppler normalisée à 70 km, et (b) zoom sur les raies de Bragg du premier ordre.

Malgré un niveau de signal diminué, l'antenne flottante a pu correctement détecter les raies de Bragg. Nous avons alors normalisé les signaux de l'antenne 15 et de l'antenne flottante (cf Fig. 5.19). Un faible étalement des raies de Bragg est visible, particulièrement sur la raie négative mais il reste très limité. La raie positive semble légèrement découpée mais globalement les raies de Bragg sont retrouvées dans les deux cas à $f_b = \pm 0.36$ Hz, correspondant à une fréquence de 12.34 MHz. Ainsi, l'antenne flottante peut trouver les bonnes positions de raies de Bragg, tout en conservant le même rapport d'amplitude entre elles. De plus l'étalement limité des raies permet d'envisager des applications de surveillance maritime.

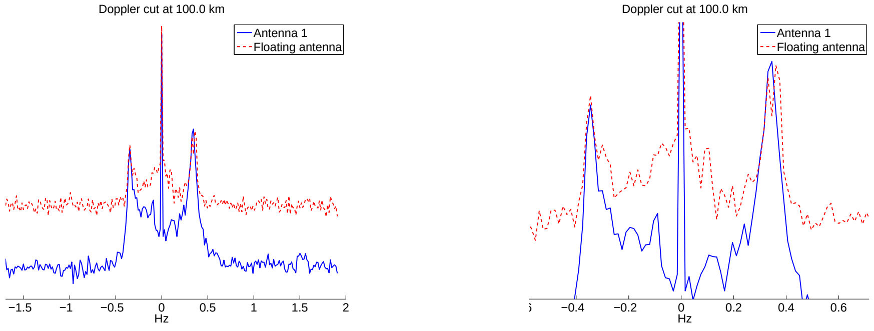

(a) (b)

Figure 20: (a) Coupe Doppler normalisée à 100 km, et (b) zoom sur les raies de Bragg du premier ordres.

Ces premières mesures ont validé la faisabilité du concept d'antenne flottante. Des mesures avec des états de mer plus élevés sont cependant nécessaires.

Conclusion

Le radar HFSWR est un outil permettant la surveillance de grandes zones maritimes et la mesure de paramètres océanographiques. Cette thèse a permis de proposer une solution à l'inconvénient majeur de ces radars, c'est à dire leur résolution limitée en azimut. Un nouveau concept a été proposé, consistant à mettre les antennes du réseau de réception sur des bouées en mer.

Cependant, la déformation du réseau génère des perturbations entrainant notamment des remontées de lobes secondaires dans le diagramme de rayonnement. Des méthodes de correction ont été proposées suivant le type de déformation (vertical ou horizontal) et elles ont été comparées à des méthodes itératives. Ces méthodes de correction abaissent de façon significative le niveau de lobes, en temps réel.

Dans un deuxième temps nous avons étudié la robustesse de l'algorithme MUSIC pour la détection de directions d'arrivée. Une deuxième méthode appelée Weiss Friedlander a permis d'améliorer de façon significative les performances de MUSIC.

Pour finir, une première expérimentation avec une antenne flottante a été menée. Ces premiers résultats ont permis de valider le concept d'antenne flottante pour de faibles états de mer en obtenant des signaux exploitables dans le cadre d'applications océanographiques. De plus, même si des mesures avec de plus grands états de mer doivent être menées, le niveau de perturbations amené par le mouvement de la bouée reste relativement faibles. Ce résultat ouvre des perspectives dans le cadre de la détection de cibles.

Ph.D. THESIS
OF THE NATIONAL INSTITUTE OF APPLIED SCIENCES OF RENNES

Speciality:
ÉLECTRICAL ENGINEERING

Thesis Submitted for the Degree of:
DOCTOR OF PHILOSOPHY

By:
Anthony BOURGES

Feasibility of a surface wave radar on buoys - On the deformation of the antenna array and realisation of a buoy

Defended:
November, 7^{th} 2008

Jury:

Reviewers:

Pr. Jean-Yves DAUVIGNAC	University of Nice Sophia Antipolis
Pr. Marc HELIER	University Pierre et Marie Curie

Examiners:

Pr. Pierre FLAMENT	University of Hawaii
Dr. Randy HAUPT	Pennsylvania State University
Pr. Raphael GILLARD, co-supervisor	INSA of Rennes
Dr. Régis GUINVARC'H, co-supervisor	SONDRA/Supelec
Pr. Bernard UGUEN, Thesis Director	University of de Rennes 1

Contents

Introduction

The concept of the Economic Exclusive Zone (EEZ) finds its legal basis in the United Nations Convention on the Law of the Sea [4]. The states may establish an exclusive economic zone with a maximum of 200 nautical miles (370 km) from their coasts. In this area, the State has sovereign rights as regards from the exploration, the exploitation, the conservation and the management of natural or biological resources. The rights extend from the waters above the seabed and the seabed in the subsoil. Moreover, the rights apply to the exploration and exploitation of the zone for economic purposes, such as the production of energy from water, sea currents and winds. Finally, the State has full jurisdiction regarding the establishment and the use of artificial islands, installations and structures for marine scientific research, protection and preservation of the marine environment.

Thus, the monitoring of the EEZ is an economic, civil and military issue. The importance of the investment of the scientific activity in Singapore, France and abroad on this area is considerable [26]. France has, through its departments and overseas territories, the second world EEZ, over ten millions km^2. While Singapore has a much smaller EEZ, it is one of the world's most busy ports and is situated at the Malacca straits southern end which is of the most important shipping lanes in the world. Therefore, although their situations can be described in different ways, both countries have to face the same issue: how to maintain the security and safety of goods, people and the maritime environment?

In terms of sensors requirements, it means a sensor able to monitor a large zone, permanently with a good resolution. Whatever the type of sensors, it can be either ground based or based on a satellite or airborne.

Satellites If the satellite is a geosynchronous one, it will cover a wide zone permanently. However, it also means it will be at 35786 km from the Earth, therefore a fine resolution cannot be obtained. On the contrary, considering a satellite in Low Earth Orbit, it will not permanently cover the area but will have a typical revisit period of 90 min.

Airborne Obviously, an airborne sensor is not able to permanently cover a given area.

Ground based A ground based sensor can easily be a permanent solution. However, for most of them, their wave propagation does not follow the earth curvature and they cannot detect an object beyond the horizon (cf. Fig. 21), limiting the range of the monitoring area.

Figure 21: Coverage of various type of radars.

However, not all the ground-based radar are horizon limited. For instance, X-band radars can see over the horizon thanks to a ducting effect, but only in some particular circumstances. More interesting for the monitoring of the EEZ, High Frequency (HF, 3-30 MHz) radars have the capacity to receive target echoes over much longer distances than microwave radars. The most common type of HF radar operates in the skywave mode, which receives radar echoes through reflection from the ionosphere. ONERA proposes for example the Nostradamus project which is a skywave radar located in Dreux.

HF radar can also operate in the surface wave mode, which provides coverage in the order of a few hundred kilometers, roughly the size of the EEZ. Signals propagate efficiently in the surface wave mode only at vertical polarization and require a conducting surface along the signal path. This makes the HFSWR practical at coastal installations where the ocean surface serves as the conducting surface.

The drawback of these HFSWR is a lack of resolution. A good azimuthal resolution means a large receiving array. At HF frequencies, this leads to a very large receiving array, several hundred meters. Furthermore, this receiving array needs to be as close to the sea surface as possible to correctly excite the surface wave mode. Both requirements are extremely hard to fullfill at the same time if the HFSWR is located on the coast.

The idea is then to put the radar where there is plenty of room: directly on the sea surface. Each antenna of the HFSWR is placed on a separate floating platform, a buoy for instance, as the array spacing is of the order of 10 m. Each antenna has then its own movement. The array is conformed to the sea surface and therefore undergoes a continuous deformation.

Considering the potential valuable applications of these HFSWR on buoys, along with their originality, Singapore and France have decided to launch together a research program. This has been done within the framework of SONDRA, a joint research laboratory between Singapore and France, made of four partners, Supelec and ONERA from France and the National University of Singapore and the Defence Science and Technology Agency from Singapore. A PhD thesis funded by DSTA has then be started which has mainly aimed at investigating the feasibility of this concept.

This work is then twofold. A first part aims at investigating the effect of the sea surface on the radiation pattern of the array; it includes the analysis of the sea surface movements and of their effects on the floating antennas, along with the developpement of a correction technique to compensate for these sea surface movements. The second part addresses the issue of the modulation of the signal. Most of this work is focussed on the first part, while the second part is done through the realization of a floating antenna and its measurement.

Chapter 1 describes the HFSWR. Its basic principle is introduced, its components are detailed with a particular emphasis on the phased array. The specific processing of the signal is then explained. Some oceanographic notions are also given in order to understand the importance of the Bragg lines.

Chapter 2 introduces the modelling of the sea surface and of the movements of the buoys. It starts by explaining the generation of a wave. It then describes how to generate a 3 dimensional modelling of a sea surface, based on a sea spectrum and on a spreading function. The different sea states are presented. In addition, the time evolution of these sea surfaces is described. Examples of sea surfaces are then given to illustrate the mechanisms. These surfaces are then used in a simple model we have made to study the displacements of the buoys.

Chapter 3 investigates the receiving array with deformations. The various sources of disturbances are studied depending on the type of displacement i.e. the vertical (along z axis) and the horizontal movements (along x and y axis). These displacements introduce deformations in the radiation pattern of the floating receiving array. Correction methods are proposed, that consist in modifying the excitation coefficients of the array. At the end of the chapter, these corrections methods are compared with iterative methods.

Chapter 4 proposes a new approach of the floating antennas problem focusing on receiving signal to obtain information about targets directions of arrival. The first part provides a presentation of MUSIC and Weiss Friedlander algorithms which developes in that purpose by extracting properties of the correlation matrix of received signals in the receiving array. The second part tests their robustness considering positioning errors in the receiving array.

Chapter 5 describes a realization and the first measurements of a floating antenna. This experimentation permits to introduce a second issue generated by the movements of floating antennas: the modulation of the received signal. In fact, the displacement of every elementary buoy, independently of the array deformation generates some modulations introducing a spreading of the Bragg lines.

Chapter 1

High Frequency Surface Wave Radar (HFSWR)

1.1 Introduction

High Frequency Surface Wave Radars (HFSWRs) use a particular mode of propagation, the surface wave mode that propagates at the interface between the air and the sea. It is therefore possible to produce systems with ranges of a few hundred kilometers [33][7][25]. The surface wave spreading along the interface between the air and the sea, the signal received by the radar contains information on the properties of this surface and on various objects disseminated over the sea surface [36]. This information can be used for various applications, ranging from oceanography to target detection. To collect as much information as possible, a particular emphasis is put on the receiving array. The challenge addressed by this thesis is to put on buoys the receiving array.

The first part of this chapter gives details on both HF surface waves and on the HFSWR. Then, the second part describes the two main applications: oceanographic monitoring and target detection for military applications, with a particular emphasis on the oceanographic ones. The third part provides some theoretical formulation of array theory which will be helpful for setting the correction algorithms. Finally, we present our alternative solution to the classical coastal receiving array of HFSWR, along with its interests and specificity.

1.2 High Frequency waves

The ground is characterized by its conductivity σ and its permittivity ϵ. The complex permittivity is:

$$\epsilon_0 \epsilon_c = \epsilon - j\frac{\sigma}{\omega} \tag{1.1}$$

where ϵ_c is the relative complex permittivity, ϵ_0 the permittivity of the vacuum, ω the angular frequency and σ the ground conductivity.

For the HF waves, the displacement current is smaller to the conductivity current ($\epsilon << \frac{\sigma}{\omega}$), the ground is a conductor but with some losses which can be taken into account as follows [35]:

$$\alpha = \frac{2\pi}{c_0}\sqrt{\frac{\sigma f}{4\pi\epsilon_0}} \tag{1.2}$$

where α is the attenuation in Neper per meter (1 N_p = 8.6 dB), c_0 the speed of the light in the vacuum and f the operating frequency.

At the interface between the atmosphere and the ground, the discontinuity of the electric induction generates a density of charges on the ground surface. This density of charge creates a weak deviation of waves which has then a parallel propagation to the interface. This induction phenomena allows the waves to propagate at the interface. The waves are called surface waves and they follow the Earth curvature.

For the particular case of the sea, the surface is a good conductor and the surface waves spread easily in the HF band.

1.3 High Frequency Surface Wave Radar (HFSWR)

High Frequency (HF) radars are referred to as over-the-horizon radars because of their capacity to receive target echoes over much longer distances than microwave radars, which are restricted to distances defined by the line-of-sight or the horizon. The most common type of HF radar operates in the sky wave mode, which receives radar echoes through reflection from the ionosphere. The ONERA proposes for example the Nostradamus radar which is a skywave radar localized in Dreux.

HF radar can also operate in the surface wave mode, which provides coverage of the order of several hundred kilometers. Signals propagate efficiently in the surface wave mode only for vertical polarization and we have seen that it requires a conducting surface along the signal path. This makes the HFSWR practical at coastal installations where the ocean surface serves as the conducting surface (cf Fig. 1.1).

1.3.1 Antenna system

HFSWR generates electromagnetic waves radiated toward the sea. One part of the transmitting signal is backscattered by the sea surface. This signal is recovered thanks to a receiving antenna system. In fact, HFSWR measures the spatial distribution of the reflectivity of the waves on the sea. HFSWR are usually quasi monostatic radars, it means that the transmitting and the receiving antennas are separated, but only by a short distance in terms of wavelength (cf Fig. 1.1).

Generally speaking, two modes of transmission are possible:

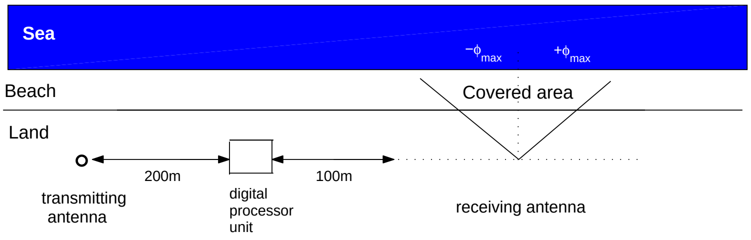

Figure 1.1: HFSWR geometry

- The first mode uses pulsed waves, they are called "pulsed radar". The radar transmits a pulse during a time T_r and waits for the return before the transmission of another one,
- The second one uses a continuous wave, they are called "continuous wave mode". The required de-coupling between transmitter and receiver has to be achieved by means of using a transmitter beamforming.

Most of the HF radars used the pulsed mode, except the WERA radar we have used for our measurements. The last chapter will go into more details on the WERA.

The HFSWR receiving antenna is in many cases a phased antenna array [33]. The receiving array of a "pulsed radar" is switched off during the transmission of the pulses. For the "continuous mode" radar, the receiver is continuously on in order to pick up signals. The signal processing is carried out in parallel to transfer all antennas amplitude and phase information to the digital processor units [15]. Its basis will be explained in section 1.4.1.

1.3.2 Dimensions of a HFSWR

The capabilities of a radar, such as target detection or the measurement of oceanographic parameters, depends on its resolution cell. For a HFSWR, the area to be observed is defined in the (x-O-y) plane (cf Fig. 1.2), i.e. on the sea surface. In terms of azimuth, the radar angular sector of observation is defined by $\pm\phi_{max}$. So, the receiving array needs to scan all this angular sector and has to be designed for that purpose.

The observation area is also divided into radar cells, fixing its resolution capabilities. The resolution cell is defined as the surface that contributes to the echo received by the radar [29]. The cell size is constrained by range and angular resolutions.

The range resolution δR is the capacity to separate two echoes of a radar in distance:

$$\delta R = \frac{cT_r}{2} \tag{1.3}$$

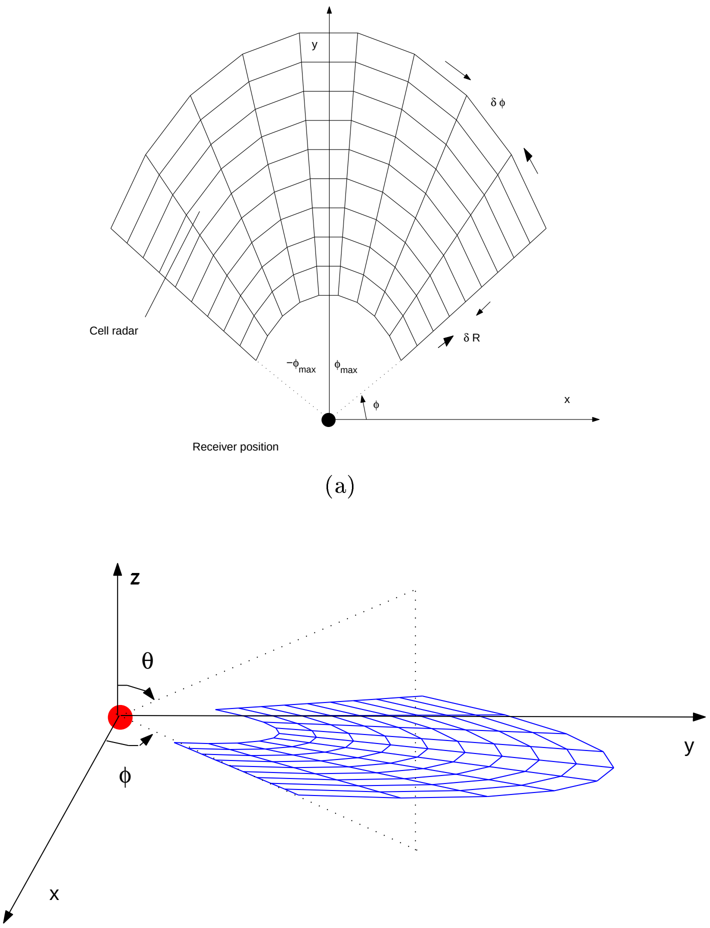

(a)

(b)

Figure 1.2: Observation area of a radar

with c the celerity. This formula applies only in the case of a pulsed radar. The larger T_r, the smaller the range resolution. The range resolution of a radar in "continuous wave mode" is:

$$\delta R = \frac{c}{2B} \tag{1.4}$$

where B is the frequency bandwidth of the radar.

In the same way, the angular resolution $\delta\phi$ is defined as the minimum angular separation at which two identical targets can be separated when at the same range R. Fig. 1.3 illustrates the relation between the angular resolution and the equivalent resolution in distance. It is called the cross range resolution and it permits to denote

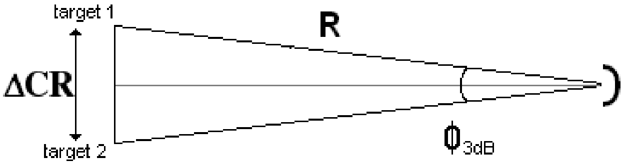

Figure 1.3: Cross range resolution.

the resolution in the direction orthogonal to range.

$$\Delta CR = 2R \sin \frac{\phi_{3dB}}{2} \tag{1.5}$$

where ϕ_{3dB} is the -3 dB beamwidth of the main beam. It corresponds to the angular range for which the radiated field is larger than $\frac{1}{\sqrt{2}}F_{max}$, F_{max} being the maximum value of the field.

The cross range resolution increases linearly with range as illustrated in Fig. 1.2, whereas the range resolution is constant.

To conclude, the radar capabilities are fixed by the cell resolution which means the range and the angular resolution. The range resolution can be improved by modifying the transmitting signal, this point will not be discussed in the thesis. The angular resolution is impressed by the half-power aperture of the radiation pattern of the receiving array. It means that the angular performance depends on the geometry of the receiving array. The larger the array, the better the angular resolution. This point is discussed in section 1.5.

1.4 HFSWR Applications

This section is focused on the different applications of HFSWR. We distinguish two main applications: the measurements of oceanographic parameters and the target detection. The surface wave spreads along the interface between the air and the sea, therefore the signal received by the radar contains information about this surface [36]. One possible application is thus to find the oceanographic parameters of the sea surface (wind speed, wind direction, current ...) from the received signal [9] [34]. In this application, the signal of interest is the signal from the sea surface, all the other signals (ship echoes from instance) are the noise. Of course, the opposite problem is also of interest, i.e. the presence of targets in the received signal, this time, the signal from the sea is the noise.

Besides the standard information of a radar, distance and direction of arrival of a target, and thanks to the frequency band, the HFSWR provides some additional information with the Doppler shift. A particular signal processing is applied to the received signals in order to obtain a Range Doppler representation, which is the usual way of plotting the results.

1.4.1 Range Doppler representation

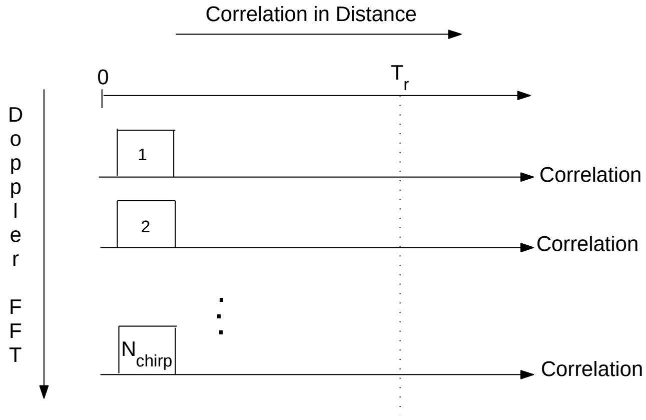

Figure 1.4: Process of doppler distance with an HFSWR.

The radar signal processing consists of a range Doppler analysis of the backscattered signals of each antenna of the radar. All the channels are treated in parallel in the digital processor unit.

A three dimensional dataset is obtained. Each element of this dataset is associated with:

- The magnitude of the signal,
- The group distance, determined by the correlation between the received signal and the replica of the transmitted signal,
- The Doppler frequency obtained with a spectral Fourier analysis.

The processing in range Doppler is illustrated in Fig. 1.4. Practically, a first Fourier transform is applied ('short time' Fourier transform) to realize the correlation between the emitted signal and the received signal. Then, a second Fourier transform is performed from pulse to pulse ('long time' Fourier transform) to analyse for the Doppler shift.

The choice of the transmitting and receiving parameters (transmitting time, receiving time, number of chirps) permits to fix the Doppler frequency resolution and the number of range cells.

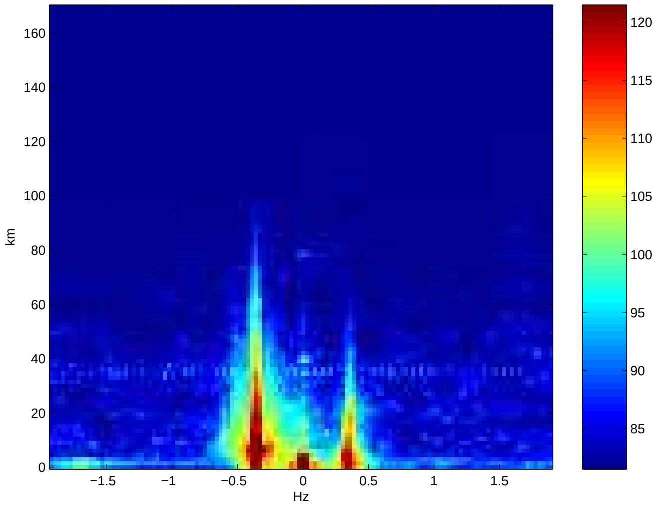

Figure 1.5: Example of a range Doppler plot.

Fig. 1.5 introduces an image in range Doppler. It is a characteristic response of the sea. This example shows two lines at two Doppler frequencies at $\pm f_b = 0.36$ Hz and one at 0 Hz. The first two lines are called Bragg lines and the last one is a DC coupling or the echo of the land. The next section is an explanation of the origin of these lines.

1.4.2 Sea surface and Bragg lines

The sea surface is composed of many waves spreading in all directions, as shown on Fig. 1.6. This system of waves is generated by the wind and the waves of gravity. Further details are given in Chapter 2.

The interactions between the surface wave and the sea surface can be modeled by the mechanism of the resonant Bragg scattering, as explained in the next section.

First order of Bragg lines The radar wave arrives with an incident angle α on the crests of a train of waves with a wavelength L (see Fig. 1.7). A portion of the energy is diffracted in the direction of the transmitter. If the wavelength L is about half that of the radar, the diffracted contributions adds in phase (Bragg resonance effect). A strong

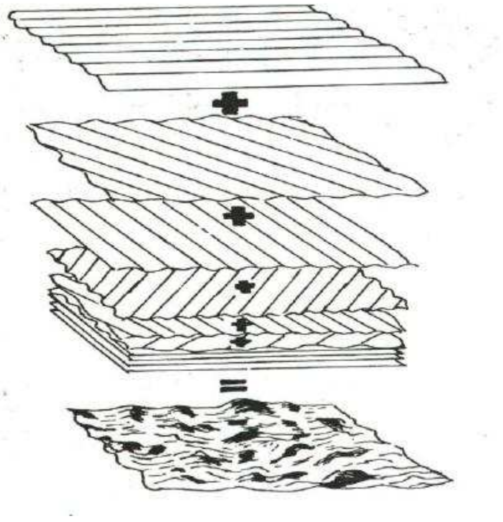

Figure 1.6: Decomposition of a sea surface

backward signal is then produced as shown on Fig. 1.5. The condition of the resonance is given by:

$$L \cos \alpha = \frac{\lambda}{2} \tag{1.6}$$

where L is the wavelength of the sea wave, α is the incident angle of the wave and $\lambda = c_0/f$ is the electromagnetic wavelength of the radar with c_0 the celerity of light.

In the case of a HFSWR application, α is almost zero. So, Eq. 1.6 becomes $L = \lambda/2$.

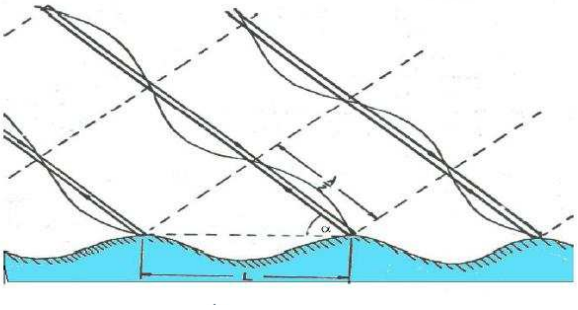

Figure 1.7: Interaction between the wave and the sea surface

The speed of the sea wave is given by[22]:

$$V = \sqrt{\frac{gL}{2\pi}} \tag{1.7}$$

where g is the gravity constant.

When Eq. 1.6 is satisfied:

$$V = \sqrt{\frac{gc_0}{4\pi f}} \tag{1.8}$$

It corresponds to a Doppler shift f_b that is given by:

$$f_b = \frac{2V}{c_0} f_{MHz} = 0.102\sqrt{f_{MHz}} \tag{1.9}$$

where f_{MHz} is the frequency in MHz and f_b is expressed in Hz.

For HF frequencies, there are always two trains of waves: a train of sea waves which goes from the radar to the open sea and an inverse train of waves. So, there are two constructive interferences at $+f_b$ and $-f_b$. These are the Bragg lines for the first order.

Second order of Bragg lines We have seen in the previous paragraph that only two trains of waves comply with the condition of resonance, which result in two dominant peaks. However, in the system of waves, second and higher order scattering exists and results in other lesser peaks and a continuum. It is generally accepted that the second order covers $[-2f_b; +2f_b]$, [32][12].

Echo of the land We have always considered the radiation of the radar towards the sea. But for most of the coastal HFSWR, there is also a symmetric backward radiation, towards the land. This radiation results in a backscattered signal with a zero Doppler shift (see Fig. 1.5). Other causes may exist, such as the presence of islands.

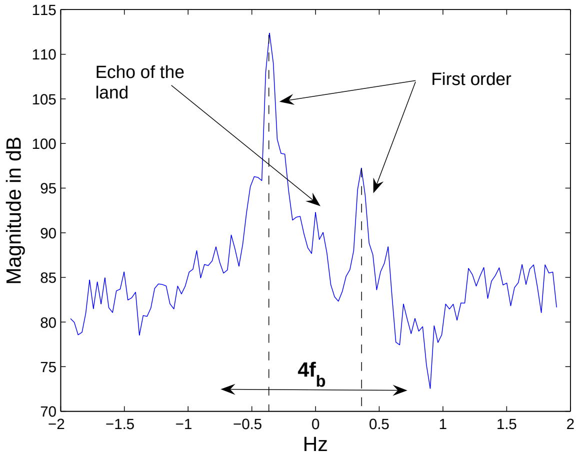

Figure 1.8: Doppler spectrum of the sea.

Doppler spectrum of the sea Fig. 1.8 is a cut of Fig. 1.5. It summarizes the elements previously described, a zero Doppler component (echo of the land), two components at $\pm f_b$ (the first order of Bragg) and a continuum of components between $[-2f_b; +2f_b]$ with lower magnitudes.
All these elements are due to the sea surface. Therefore, the information on the heights of the waves, the speed of the surface currents, the speed and the direction of the wind can be extracted from this Doppler spectrum of the sea. This is explained in the next section.

1.4.3 Oceanographic applications: calculation of oceanographic parameters

HFSWR is the only sensor that can measure temporal and spatial ocean properties simultaneously over thousands of square kilometers with a good resolution. It is normally deployed as a pair of land stations with overlapping coverage, but it can operate also from a single land station, with reduced capabilities. Oceanographic measurements include surface current, vertical current shear, directional wave height spectra and wind direction. These aspects are introduced in the following section.

One important point to note is that the calculation of the meteorological parameters from the sea spectrum is realized from empirical formulas [22] and [24].

1.4.3.1 Wind direction

The wind direction is obtained from the relationship which exists between the amplitude of the first order of Bragg, the direction of observation of the radar and the wind direction. This is represented under the shape of a cardioid (Fig. 1.9).

$$\phi_{wind} = \pm 90 \left(\frac{\Delta S - 24}{24} \right) \tag{1.10}$$

where ϕ_{wind} is angle between the wind direction and the radar look direction in degree and ΔS is the ratio in dB between the two Bragg lines.

Using Eq. 1.10, it is possible to obtain the wind direction over the area covered by the radar, as illustrated in Fig. 1.9.

1.4.3.2 Wave heights

The wave heights are obtained from the relationship between the energy of the first order (0.14 Hz around the Bragg frequencies in the first order) and the second order (0 Hz to f_b):

$$k_0 h = 0.8 r^{0.6} \tag{1.11}$$

where k_0 is the wavenumber of the wave, h is the quadratic mean of the wave height and r the energy ratio in dB.

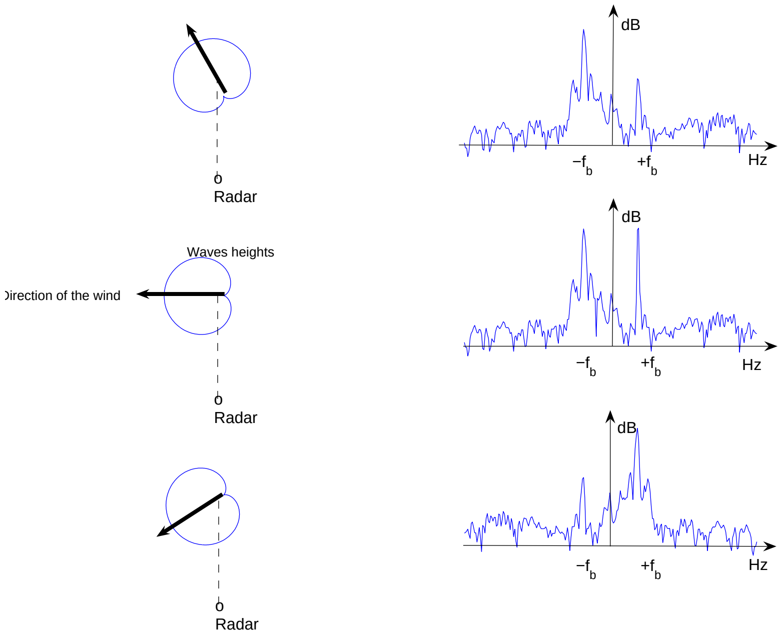

Figure 1.9: Cardioids of wind with the corresponding Doppler sea spectrum

The significant wave height $H_{1/3}$, used in meteorology, is obtained by:

$$H_{1/3} = 2.83h \tag{1.12}$$

A more precise definition of $H_{1/3}$ related to sea state is given in Chapter 2 (cf Eq. 2.9).

1.4.3.3 Surface currents

The radial velocity of surface currents is obtained using the gap between the theoretical positions of the first Bragg line (Eq. 1.13) and its observed position:

$$V_r = \frac{c_0 \Delta f}{2f} \tag{1.13}$$

where V_r is the radial speed of the surface current, f is the work frequency and Δf is the shift between the emitted frequency and the measured frequency. Fig. 1.10 show a map of the surface currents off the shore of Brittany, measured in real time by a pair of HFSWR (red stars on the figure). With only one radar, the angle can be found, but modulo 180°. The up to date figure is available to the navigators, or any interested persons, on the internet [5].

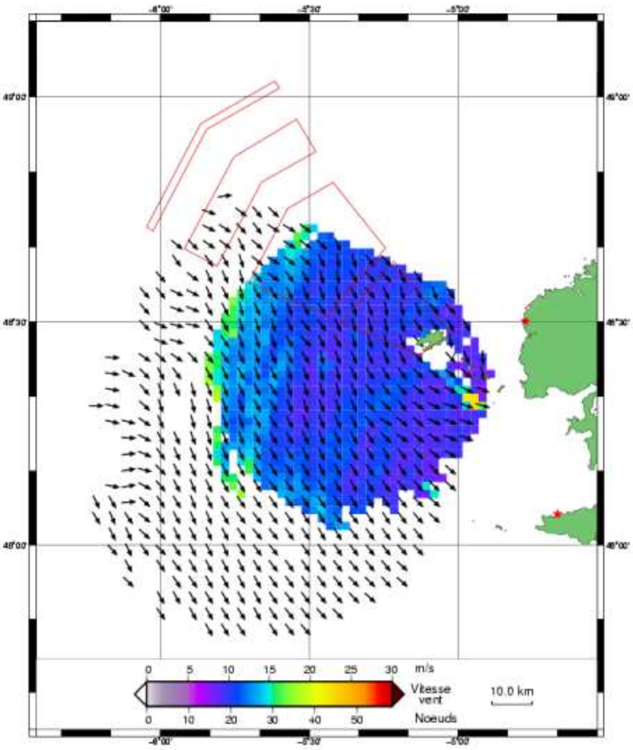

Figure 1.10: Surface currents in the area of Brittany coasts

1.4.3.4 Validity of empirical formula

As outlined by C. Kerbiriou [22], formulas from Eq. 1.10 to Eq. 1.13 are empirical and the validity of the results may be questionable. The effect of integration of the beam on the radar cell (50 km by 5 km in the case of C. Kerbiriou) is not known. It is necessary to confront regularly, or even permanently, calculated data and data measured on the ground by buoys or ships.

1.4.4 Monitoring application and target detection

The pace of modern military operations and the over-the-horizon range capability of many weapons systems impose heavy demands on real-time surveillance and intelligence support. For operations in the littoral zone, there is a clear requirement for a relocatable, shore-based sensor which can provide reliable all-weather detection of small surface and aerial targets of interest out to ranges in excess of 200 kilometers from the coast. HFSWR may well provide the most cost-effective solution to this requirement, given the results of recent trials of experimental land-based systems developed in USA, in France, in Australia and in Canada [7] [6].

Contrary to the oceanographic applications, the presence of the sea spectrum is here a problem. The magnitude of the first order Bragg line is actually larger than the response of a target, even than the response of large ships. However, the Bragg peak for coastal radar is quite narrow. Thus, the usual way to circumvent this problem is to change the emitting frequency because it will change the position of the Bragg line. This undesirable element is called sea clutter of the sea spectrum.

To give a precise idea, consider Fig. 1.5 and a fishing boat (in other words a pirate ship) approaching a yacht. At 10 MHz, the Doppler shift of the fishing boat approaching at 20 km/h is roughly 0.4 Hz. It will thus be totally hidden by the Bragg line.

In addition to this sea clutter, we can add the disturbances caused by the ionosphere. It is called the ionospheric clutter. It is introduced in the measured signal because of the directivity of the antennas [21] and [20].

1.5 Design of the receiving array

This section discuss the design of the receiving array of an HFSWR. It is focused on the choice of a phased array. The Shelkunoff's representation is also proposed to highlight some aspects of the discussion on the zero placement method.

1.5.1 Phased array

The antenna plays a major role in determining the angular resolution of the radar [29]. A wide variety of antenna types can be used, however the phased antenna array is most of frequently adapted in the HFSWR context.

A phased array is obtained by associating several elementary antennas and by controlling the phase of their excitation coefficients. It provides an efficient way of steering the main beam in a desired direction. This section will briefly summarize the basics of phased array. The first part express the radiated field by a translated antenna. The law which follows computes the radiated field of phased arrays, introducing the concept of array factor.

1.5.2 Radiated field by a translated antenna

This section permits to determine the radiated field of a translated element. So, we consider antenna 1 which is localized at $\vec{r} = [x, y, z]$ with its associated radiated field intensity $F(\vec{k})$ and a translated antenna, named antenna 2 which is localized at $\vec{r} - \vec{d}$ with its associated radiated field intensity $F_d(\vec{k})$ [13]:

$$F_d(\vec{k}) = e^{j\vec{k}.\vec{d}} F(\vec{k}) \tag{1.14}$$

where k is the wavenumber, $k = \frac{2\pi}{\lambda}$ and λ the wavelength, $\vec{k} = k.\hat{k}$, $\hat{k}$ describing the direction of the incident wave.

The phased array being the sum of the translated antennas, Eq. 1.14 permits to compute the array field. This is the topic of the next section.

1.5.3 Array pattern multiplication

An array of N identical antennas is now considered. Antenna n is located at $\vec{r} - \vec{d_n}$. Relation 1.14 can be used for the calculation of the total radiated field intensity $F_{tot}(\vec{k})$ of all the N antennas:

$$F_{tot}(\vec{k}) = A(\vec{k}) F(\vec{k}) \tag{1.15}$$

with:

$$A(\vec{k}) = i_1 e^{j\vec{k}.\vec{d_1}} + i_2 e^{j\vec{k}.\vec{d_2}} + \cdots + i_N e^{j\vec{k}.\vec{d_N}} \tag{1.16}$$

with i_n which is an excitation coefficient attached to antenna n ($i_n \in \mathbb{C}$). $A(\vec{k})$ is called the array factor.

In the following, we restrict our analysis to linear antenna arrays. Linear antenna arrays are a single convenient when the radiation pattern has to be optimized in only one plane. This is the case for HFSWR where the observation plane coincides with the sea surface (xOy). We assume that the array elements are distributed along the x axis.

In the case of a uniformly spaced one dimensional array, the N antennas positions are given by the coordinates $(x_n, 0, 0)$ with $x_n = (n-1)d$ where d is the constant distance between antennas. The array factor will be:

$$A(\theta, \phi) = \sum_{n=1}^{N} i_n e^{j(n-1)kd\cos\phi\sin\theta} \tag{1.17}$$

or,

$$A(\psi) = \sum_{n=1}^{N} i_n e^{j(n-1)\psi} \tag{1.18}$$

where

$$\psi = kd\cos\phi\sin\theta \tag{1.19}$$

In the observation plane, $\theta = 90°$. Eq. 1.17 reduces to:

$$A(\phi) = \sum_{n=1}^{N} i_n e^{jk(n-1)d\cos\phi} \tag{1.20}$$

ϕ_{3dB} is usually expressed as [29]:

$$\phi_{3dB} \approx 0.886\frac{\lambda}{l} = 0.886\frac{\lambda}{Nd} \tag{1.21}$$

where l is the array length.

So, the beamwidth can be controlled by the number of elements in the array and the interelement spacing. It results that a trade off has usually to be found when designing the array. It is illustrated by a unit circle technique due to Shelkunoff. This representation is given in the following section.

1.5.4 Array pattern design: the Shelkunoff's representation

The representation developed in this section is called Shelkunoff's representation and is explained in details in [30].

For a better understanding of the Shelkunoff's representation, it is important to define the concept of associated polynomial of an array factor.

1.5.4.1 The associated polynomial of the array factor

In the Shelkunoff's representation, we consider the positions of the nulls of the radiation pattern. It means we look for the azimuth angle ϕ for which the array factor is zero.

Using Eq. 1.18 and applying a simple transformation of variable $z = e^{j\psi}$, we have:

$$A(z) = \sum_{n=1}^{N} i_n z^{n-1} \tag{1.22}$$

$A(z)$ is called the associated polynomial of the array factor.

Searching for the nulls in the array factor is equivalent to searching for the roots (or the zeros) of the associated polynomial $A(z)$ defined in Eq. 1.22.

The next section establishes some common notations using the Shelkunoff representation.

1.5.5 Shelkunoff's Zero Placement Method for a regular array

As we have seen in the previous section, the array factor of an N-element array can be written as a polynomial of degree $N-1$ (Eq. 1.22):

$$A(z) = \sum_{n=1}^{N} i_n z^{n-1} = (z - z_1)(z - z_2)...(z - z_{N-1})a_N \tag{1.23}$$

The roots of the obtained polynomial can be plotted in the complex plane. The analysis and the synthesis of a regular array can be tied to the study of the properties of the polynomial, a distinct asset for the antenna designer. To develop this approach, we can observe that when ϕ varies in real space from 0 to π, ψ varies from $\psi_b = -kd$ to $\psi_a = kd$. We can also observe that ϕ traces out a path along the unit circle in the complex plane as illustrated in Fig.1.11.

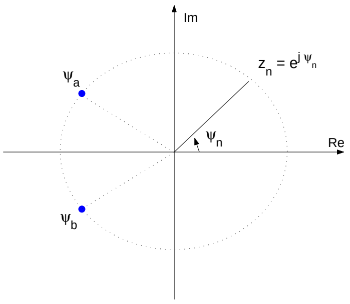

Figure 1.11: Visible region on the unit circle

For a regular uniform array, the magnitude of the roots is always equal to 1, thus they are all placed on the unit circle. If the roots of the polynomial are placed on the unit circle then they define nulls in the radiation pattern. Alternatively, if all the roots

z_n are placed off the unit circle, a radiation pattern devoid of nulls will be produced.

As we will see later, this situation can be achieved when the array is not regular anymore. An array on floating buoys belongs to this category and will be studied in Chapter 3.

We now define the visible region as the overall range of variation of ψ. It corresponds to the extension between ψ_b and ψ_a on the unit circle in Fig. 1.11.

$$-kd \leq \psi \leq kd \tag{1.24}$$

As it can be seen, it depends on the interelement spacing. Three cases are distinguished:

- if $d < \lambda/2$, the visible region is a reduced portion of the unit circle.
- if $d = \lambda/2$, the visible region exactly coincides with the unit circle.
- if $d > \lambda/2$, the visible region is covered by doing more than one turn on the unit circle. This can give rise to grating lobes or fringes, which are main beam lobes in directions other than the desired one [23].

These cases are highlighted in three examples of uniform 10-element arrays represented in Fig. 1.12. Three different spacing were chosen $d = \lambda/4$, $d = \lambda/2$ and $d = \lambda$. The zeros positions are highlighted with the circle markers. The solid line corresponds to the visible region on the unit circle.

For $d = \lambda/4$, only four zeros are on the visible region of the unit circle, this is why there are only four nulls in the array factor. For $d = \lambda/2$, all the zeros are in the visible region and there is the equivalent number of nulls in the factor array. For $d = \lambda$, the visible region goes twice on the unit circle, this is why the number of nulls is doubled. Grating lobes also appear at $\phi = 0°$ and $\phi = 180°$.

1.5.5.1 Choice of the SLL: comparison between the uniform repartition and the Tchebycheff repartition

In the examples given in Fig. 1.12, an array with uniform weights and spacing has been chosen. It leads to a uniform spacing of zeros on the unit circle. The regular positions of nulls in the radiation pattern generate a sidelobe level equal to -13.4 dB (Fig. 1.13 for an array of 10 antennas width $d = \lambda/2$.

Another approach is to consider a new representation of the zeros on the unit circle to optimize the sidelobe level of the radiation pattern. This is the case when using Tchebycheff weights [23] instead of uniform. They are computed to obtain a constant sidelobe level.

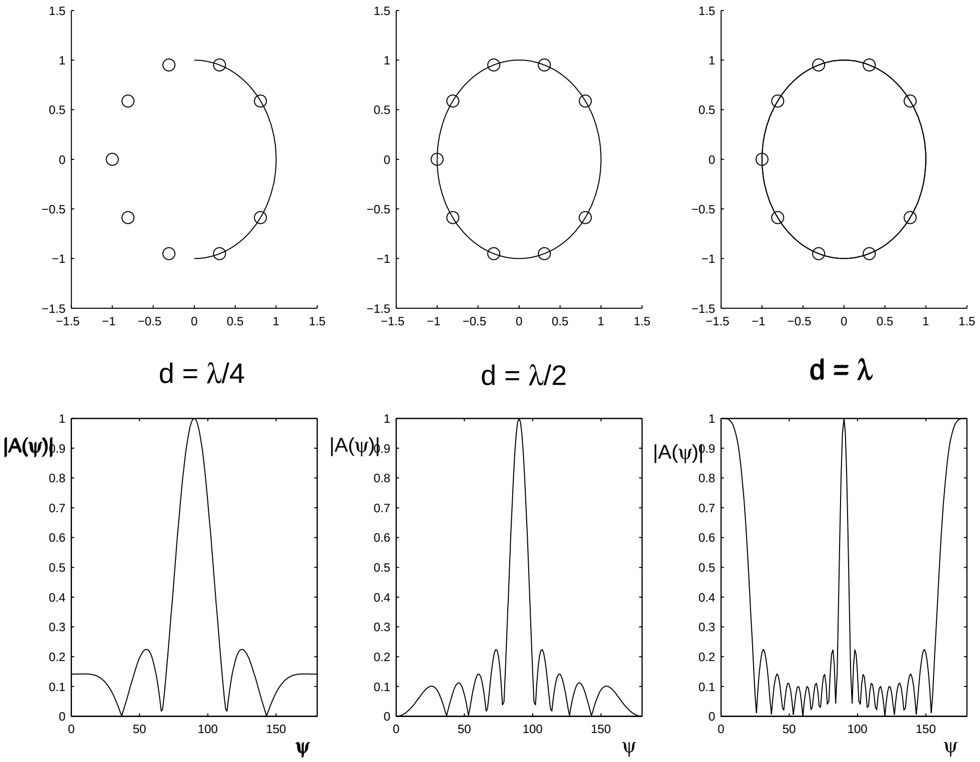

Figure 1.12: Array factor and its associated unit circle of 10-element uniform array.

As can be seen in the Shelkunoff plot (cf Fig. 1.14), this is achieved by modifying the positions of the zeros: the closest to the main beam are moved apart while the distant ones get closer.

1.5.5.2 Beam steering

As explained in section 1.3.2 beam steering is required in order to be able to scan over the desired observation range (from 65° to 115° assuming that the initial radiation is broadside $\phi = 90°$). This can be achieved without rotating the array, only by modifying the excitation coefficients of the different elements. Typically, it can be shown that a linear phase distribution $i_n = i_1 e^{jn\alpha}$ results in a beam which is moved from broadside $\phi_d = \pi/2$ to $\phi = \arccos \frac{\alpha}{kd}$.

Fig. 1.15 represents an array factor and its associated steered array factor. The roots of the associated polynomial for both array factors are represented in Fig. 1.16.

We can see that a ϕ_d translation of the main beam of the array factor is equivalent

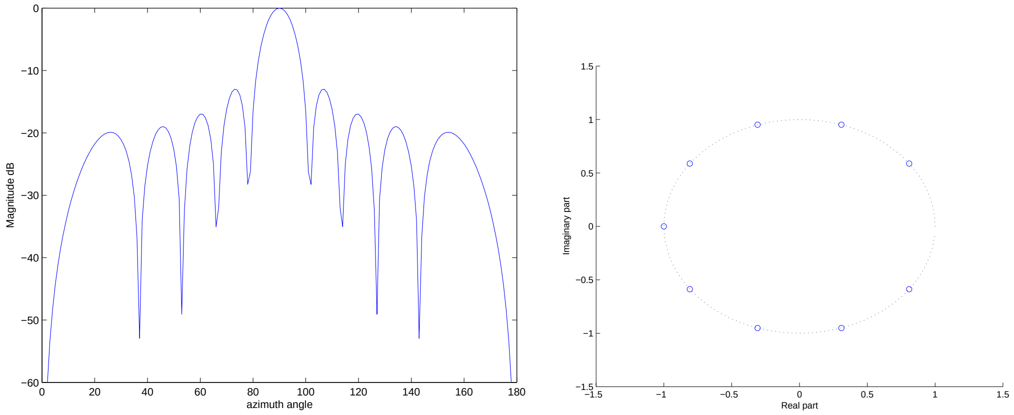

(a) (b)

Figure 1.13: Radiation pattern and Shelkunoff's unit circle representation

to a rotation of the roots of the associated polynomial on the unit circle. The relation between ϕ and ψ is not linear. The desired direction of observation moves toward the largest ψ and the width of the main beam increases when it is steered.

The real beamwidth of a steered array, using small angle from the broadside is given in [13]:

$$\phi_{3dB} \approx 0.886 \frac{\lambda}{l} \csc \phi_d \tag{1.25}$$

where ϕ_{3dB} is expressed in radian and csc is the cosecant function.

For example, in Fig. 1.15, the beamwidth ϕ_{3dB} of the array in $\phi_d = 90°$ is equal to $10.1°$ and the beamwidth of the array in $\phi_d = 65°$ is equal to $11.8°$.

The motion of the visible region translates with minor modifications in the case of a steered beam. As the angle ϕ_d varies over $0° \leq \phi_d \leq 180°$, the translated ψ' varies over the shifted visible region:

$$-kd(1 + \cos \phi_0) \leq \psi' \leq kd(1 - \cos \phi_0) \tag{1.26}$$

where the total angular width is still equl to $2kd$.

To ensure no grating lobes, ψ' must remain strictly less than 2π, which results in the following sufficient condition:

$$d < \frac{\lambda}{1 + |\cos \phi_d|} \tag{1.27}$$

This condition is a major issue when considering the trade off between the required number of antenna elements (N) and the optimal interelement spacing (d).

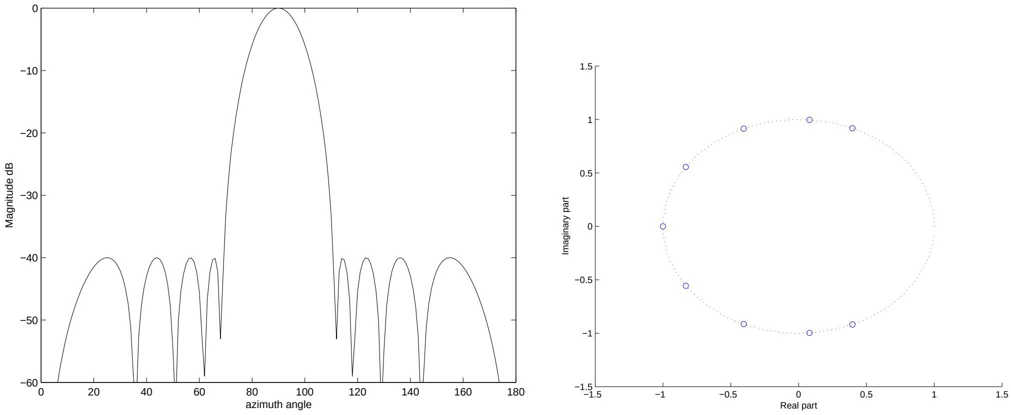

(a) (b)

Figure 1.14: Radiation pattern and Shelkunoff's unit circle representation

1.5.6 Choice of the desired receiving array

The two previous sections have presented basic results about phased arrays. The goal of this section is to propose a receiving array adapted to the constraints of a HFSWR.

From Eq. 1.5, we can determine the cross range resolution to separate two targets for a given range. For example, if we want to detect two targets separated of 10 km at 50 km. The required beamwidth ϕ_{3dB} is 11.5°.

Eq. 1.25 permits to determine the length of the receiving array l depending on its beamwidth for a given direction of the main beam. The larger the receiving array, the higher the directivity. In our example, for $\phi_d = 90°$, $l = 4.41\lambda$ and $\phi_d = 65°$, $l = 4.87\lambda$.

The length of a regular array is $l = Nd$. A discussion on the choice of N and d has to be done. It is a compromise between the grating lobes for a given ϕ_d and the global cost of the installation of the receiving array. To limit the cost, we have to limit the number of antennas N in the array keeping the same length of the array l, it means: d has to be as large as possible.

Eq. 1.27 gives a relation between the maximum interelement spacing and the beam deviation that prevents from the grating lobes. At broadside, $\phi_d = 90°$, this reduces to the earlier condition $d < \lambda$. For $\phi_d = 65°$ to 115°, it reduces to $d < 0.70\lambda$. So, for $\phi_d \in [65°115°]$, $d < 0.70\lambda$. In our example, $d = \lambda/2$ is chosen as the best compromise, it corresponds to $N > 9.74$ antennas. A number of 10 antennas is chosen.

So, to conclude, a uniform and regular array of 10 antennas with an interelement spacing of $\lambda/2$ is chosen as the desired receiving array. This array guarantees a detec-

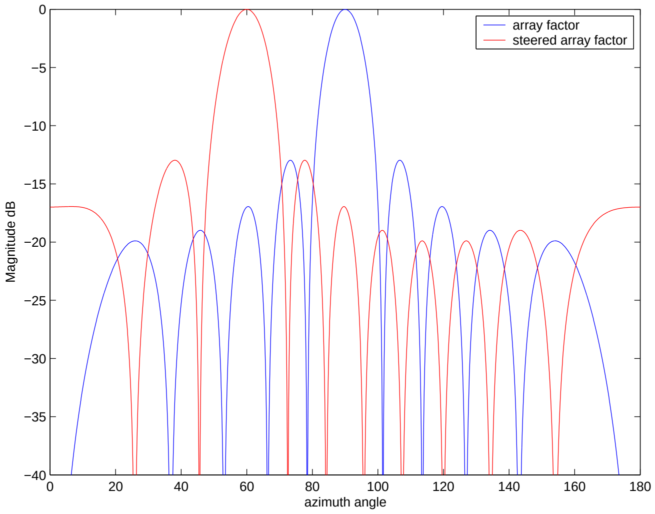

Figure 1.15: Array factor defined in $\phi_d = 90^\circ$ and its associated steered array factor in $\phi_d = 65^\circ$

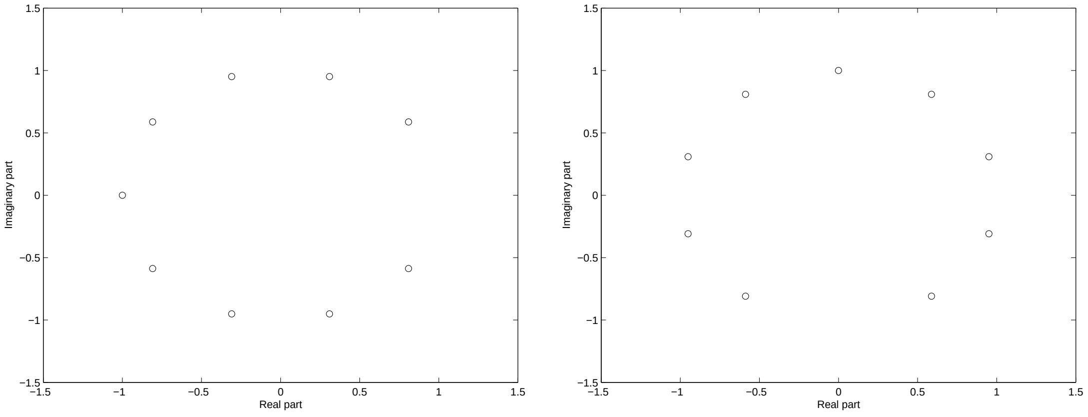

(a) (b)

Figure 1.16: Roots of the array factor defined in $\phi_d = 90^\circ$ and the roots of its associated steered array factor $\phi_d = 65^\circ$

tion of two targets at 50 km.

1.5.6.1 Elementary antenna: the dipole

The elementary antenna used in the HFSWR can be a monopole or a dipole which can be realized at low cost. We can say that a monopole is a half of a dipole where the soil plays the role of mirror. The dipole is presented in Fig. 1.17 [23].

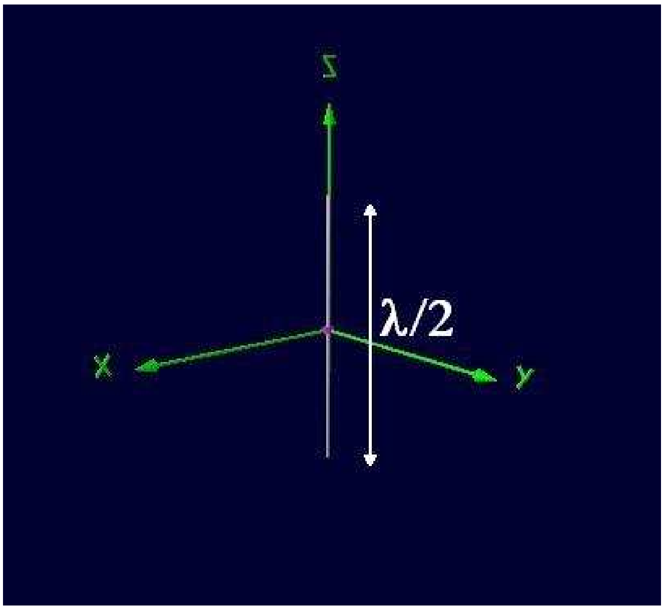

Figure 1.17: $\lambda/2$ Dipole

A representation of the radiation pattern of the dipole is given in Fig. 1.18 (a). It radiates in all the directions except in the direction of the z axis. It has an omnidirectional radiation pattern in the observation plane (xOy) (cf Fig. 1.18 (b)).

1.5.6.2 Radiated field of a uniform array of $\lambda/2$ dipoles

We consider a 10-antenna regular and uniform array of $\lambda/2$ dipoles with an interelement spacing equal to $\lambda/2$ (cf Fig. 1.19 (a)) with its associated radiated field (cf Fig. 1.19 (b)) [23]. In Fig. 1.19 (b), we can observe the main beam in the y direction.

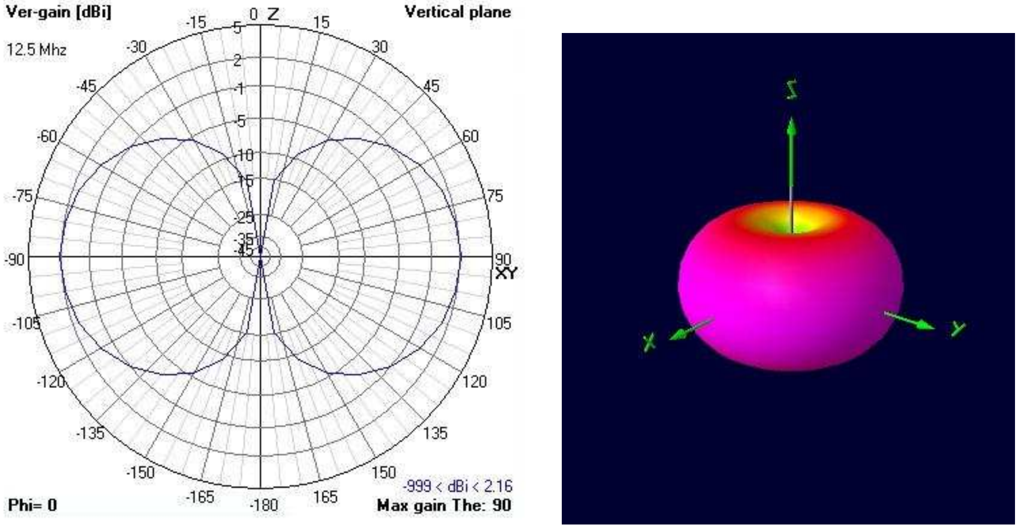

(a) (b)

Figure 1.18: Radiation pattern of a $\lambda/2$ dipole

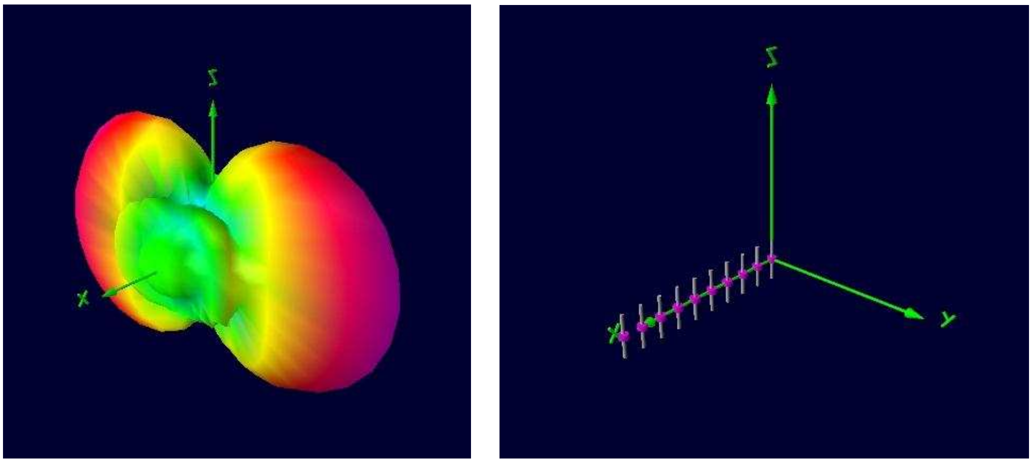

(a) (b)

Figure 1.19: Phased array of dipoles (a) with its associated radiation pattern (b)

1.6 Introduction to the floating antennas concept

1.6.1 Classical problem of HFSWR deployment

Considering the receiving array of the previous section, composed of only 10 elements with a half wavelength spacing, the array length at 9 MHz is 150m. And practically, the receiving array of HFSWR are of at least 16 elements to provide a good azimuthal resolution.

Furthermore, we have seen that to correctly excite the surface wave mode, the radar needs to be near the sea surface. This point limits the possible locations of the radar deployment on the littoral. Additional constraints may result from regulations which usually limit the quantity of HF signals that can be transmitted on the coast.

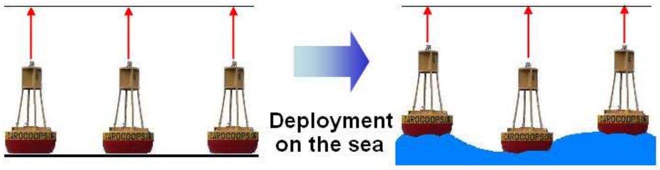

Figure 1.20: Phase disturbances in a deformed array

In order to circumvent the problem, one solution is to move the receiving array (the largest part of the antenna system) on buoys on the sea . The receiving array being directly on the sea, the wave propagation problem is directly solved. Moreover, larger receiving arrays may be considered as the available space is not limited. Unfortunately, this alternative technology also generates new problems which will be introduced in the next section.

1.6.2 Floating antennas

In the proposed solution, the receiving array consists of N antenna elements. Each of them is supported by a floating buoy on the sea surface, see Fig. 1.20. The main concern is the effect of the sea motion: it will be responsible for a displacement of the different buoys and of the attached antennas. As a result, the initial array arrangement will be modified continuously. This "deformation" of the receiving array and the associated perturbation in the radiation pattern will be studied in this thesis. Correction procedures will also be considered as a means of preserving acceptable performance in spite of the sea motion.

The second issue is related to the movements of each buoy. Each receiving antenna follows the movement of the sea surface, its received signal is thus modulated by this sea surface. This can have some strong effects on the Bragg mechanism.

1.7 Conclusion of Chapter 1

The first part of this chapter has presented the HF waves and the High Frequency Surface Wave Radar. A discussion about the design of the receiving array was proposed in a second part. A uniform and regular array is presented as the desired receiving array for an HFSWR. Different applications of HFSWR were then presented. Two domains are distinguished. This first one is the measurements of oceanographic parameters. The second one is the target detection in maritime environment.

In a last part, our alternative solution to the coastal receiving array is introduced. It consists in putting this array on buoys on the sea. This solution limits the constraints of radar deployment but raises some new issues related to the movements of the sea surface. The next chapter will therefore deal with the modelling of the sea surface.

Chapter 2

Modelling of the sea and of the buoy motion

2.1 Introduction

We have seen in Chapter 1 that HFSWR proposes good solutions for the measurement of oceanographic parameters and for the monitoring of the EEZ, thanks to its permanent coverage of a large zone. However, it requires a large space to have a good azimuthal resolution. The solution proposed in this thesis is to put the antennas of the receiving array on independent buoys on the sea surface.

The global radiation pattern of the receiving array is an addition in phase of all the radiation patterns of all the elements of this array. In our case, each independent buoy (thus, each elementary antenna) will have its own movement, on the sea surface. This should affect the global radiation pattern. The estimation of the latter effect implies a good knowledge of both the sea surface and the buoys movement on this sea surface.

This chapter is not an exhaustive study of sea surface modelling but it is focused on the study of few sea surfaces examples. Some necessary notions will first be defined and the modelling of the sea surface will then be introduced, along with its evolution with time. The second part of the chapter is a presentation of the model we have used to simulate the buoy displacement on a sea surface, such as the one described in the first part.

2.2 Sea surface modeling

In this part, we define a realistic representation of the sea surface elevation. We start by describing how the wind can generate the waves.

2.2.1 Definition of gravity and capillarity wave

When the wind starts to blow on a calm sea, waves with short wavelength appear. The first waves are called capillarity waves. After their formation, their amplitude and their wavelength increase with nonlinear energy transfer and covering. This new kind of waves is called gravity waves. The gravity waves result from the balance of gravity and inertia of the waves. If the wind blows long enough, the waves reach a stationary regime.

The smallest capillarity waves have very low amplitudes, thus they do not intervene in the process of buoys displacements. So, they do not need to be defined in our model of sea surface, only the gravity waves are going to be taken into account.

We can also introduce the concept of fetch. The fetch, cf. Fig. 2.1, is the specific distance from the coast from which the waves of the sea are not disturbed by the coast.

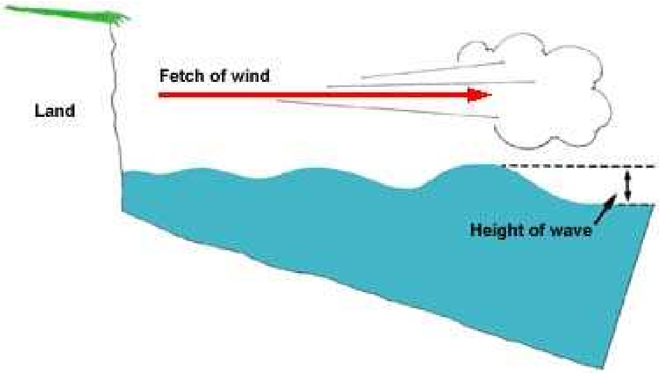

Figure 2.1: Illustration of the fetch

The sea state not only depends on the force of the wind locally but also on the fetch distance on which the wind acts. We will assume that the influence of the coast is minimum, so all the sea surface representations are realized in the open sea.

The next part will present the details of the modelling of the sea surface.

2.2.2 Sea surface generation

The sea surface is made of a large number of waves which spread in all directions. It can thus be described as a sum of waves in the space domain and time domain.

All the complex magnitudes of every elementary wave are random Gaussian variables with a zero mean which are stationary, homogeneous and statistically independent during an analysis period T.

$\xi(x^s, y^s, t)$ is the elevation of the sea surface in the horizontal coordinates of space (x^s, y^s) and time t. It can be written as:

$$\xi\left(x^s, y^s, t\right) = \sum_{l,m,n=-\infty}^{\infty} A\left(\vec{k}_{m,n}, \omega_l\right) \exp\left(-j\left(\omega_l t - k_x x^s - k_y y^s\right)\right) \tag{2.1}$$

where:

$l,\ m,\ n$ are integer number
$\vec{k_{m,n}} = k_x \vec{x} + k_y \vec{y}$
$k_x = \frac{2\pi}{L} m$
$k_y = \frac{2\pi}{L} n$
$\vec{x}$ and $\vec{y}$ are the unit vector of the sea surface plane
$A\left(\vec{k}_{n,m}, \omega_l\right)$ is the Fourier transform of the waves amplitude

The size of the patch of the sea surface is $L \times\ L$. Eq. 2.1 is actually an inverse 2D Fourier transform (using x^s and y^s) of $A\left(\vec{k}, \omega_l\right)$.

Highlighting the dynamic theory of the fluids (conservation of the mass, continuity of the surface and balance pressure), Weber and Barrick [38] have shown that, at the first order, the surface is composed of waves which are subject to the field of gravity. These waves of gravity are free, progressive and they do not travel at the same phase speed. Their dispersion relation is defined in the next section.

In the second order, waves are not gravity waves [38]. They result from the non linear interactions between two Bragg lines (see section 1.4.2. Their directions of propagation and their amplitudes directly depend on the direction of propagation and the amplitudes of the waves which are formed.

2.2.2.1 Dispersion relation

The relation between the spatial wavenumber ($k = 2\pi/\lambda$), where λ is the wavelength of the wave, and its frequency f ($\omega_l = 2\pi f$) is [22]:

$$\omega_l^2 = gk \tanh(kH) \tag{2.2}$$

where g is the acceleration due to gravity and H the depth of the sea. This relation is called the dispersion relation. When the depth of the sea is much higher than the wavelength ($H >> \lambda$), $\tanh(kH)$ is closed to 1. So, a simplified relation can be used:

$$\omega_l^2 = gk \tag{2.3}$$

This relation is used to go from the spatial domain to the time domain and reciprocally.

2.2.2.2 Introduction of the Sea Spectrum

We have seen that a sea surface is a sum of waves. To describe these waves, the power spectral density of the waves $S(\vec{k},\omega_l)$ is introduced.

In the statistical sense, the power spectral density S is the mean square of the Fourier transform (in the space time domain) of $\xi(x^s,y^s,t)$.

$$S(\vec{k},\omega_l) = \frac{L^2T}{(2\pi)^3}\left|A(\vec{k},\omega_l)\right|^2 \tag{2.4}$$

Using the relation of dispersion, $S(\vec{k},\omega_l)$ can be more generally expressed as a function of $S(\vec{k})$ [22]:

$$S(\vec{k},\omega_l) = \frac{1}{2}S(\vec{k})\delta(\omega_l - \sqrt{gk}) + \frac{1}{2}S(-\vec{k})\delta(\omega_l + \sqrt{gk}) \tag{2.5}$$

So, the complete sea spectrum can be expressed using the wave number. It depends on $\vec{k}$ and thus on k and ϕ. Therefore, $S(\vec{k})$ becomes $S(k,\phi)$ which is called the directional spectrum. This spectrum can be expressed as a separate product of the frequency spectrum $S(k)$ and of the spreading function $D(\phi)$:

$$S(k,\phi) = S(k)D(k,\phi) \tag{2.6}$$

Before describing the frequency spectrum and the spreading function we have used, we introduce the concept of the significant wave height.

Significant wave height The significant wave height $H_{1/3}$ in meter is a statistical parameter which is used in a lot of sea surface modelling. It is the mean value of heights of the superior third of waves observed during a given period of time (cf. Eq. 2.9). Significant wave height is used for evaluating the impact of waves in the open sea.

This parameter permits to classify the sea surface in the different sea states. Two scales are often used: Beaufort scale and Douglas scale.

Beaufort scale proposes an approximated description of the sea state whereas Douglas scale introduces directly a relation between the sea state and the significant wave height. So, the Douglas scale is more accurate. A description of the different sea states and their associated wind speed and significant wave height is shown in Table 2.1.

Sea State	Description	$H_{1/3}$ (m)	Wind speed (m/s)
0	Calm	0	0
1	Smooth	0 to 0.3	0 to 3.18
2	Slight	0.3 to 0.9	3.18 to 5.51
3	Moderate	0.9 to 1.5	5.51 to 7.11
4	Rough	1.5 to2.4	7.11 to 8.99
5	Very Rough	2.4 to 3.6	8.99 to 11
6	High	3.6 to 6	11 to 14.21
7	Very High	6 to 12	14.21 20.10
8	Precipitous	12	20.10

Table 2.1: Douglas scale

Pierson Moskowitz spectrum In the literature ([16] and [27]), some models are proposed to generate a spectral density of the sea. In this paragraph, a standard model is introduced [27]. Eq. 2.7 and Eq. 2.8 represent this spectrum expressed as a function of k and angular frequency ω_l respectively:

$$S(k) = \alpha H_{1/3}^2 \frac{(k_p)^2 \sqrt(kg)}{(kg)^3} e^{-\beta\left(\frac{k_p}{k}\right)^2} \tag{2.7}$$

$$S(\omega_l) = \alpha H_{1/3}^2 \frac{\omega_p^4}{\omega_l^5} e^{-\beta\left(\frac{\omega_p}{\omega_l}\right)^4} \tag{2.8}$$

with:

- $\beta = 33,93.10^{-2}$
- $\alpha = 3,89.10^{-2}$

k_p or ω_p allows to translate the energy of the spectrum toward the desired wavelength of the sea wave.
Fig. 2.2 plots two Pierson Moskovitz spectra $S(k)$ and $S(\omega^l)$ for two different values of the significant wave height. This spectrum is often used to model the gravity waves. We can see that the sea state is related to the amont of energy observed in the spectrum. The larger $H_{1/3}$, the larger the energy in the spectrum.

From Pierson Moskovitz spectrum, we can write [39] [41]:

$$H_{1/3} = 0.0297U^2 \tag{2.9}$$

where U is the wind speed.

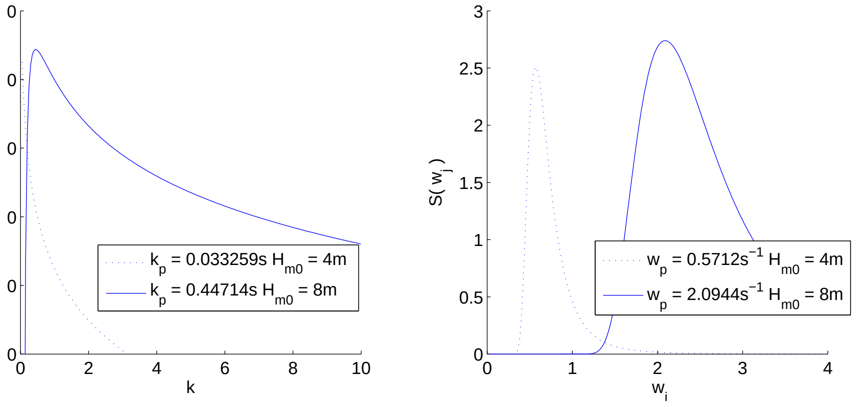

Figure 2.2: Pierson Moskovitz Spectrum of the sea (Left) versus the wavenumber (Right) versus the angular frequency.

The spreading function To realize a directional spectrum, we need to define a spreading function [16] [14]. It permits to compute the 2D directional spectrum from the spectral density defined previously. A number of common spreading functions can be found in the literature. In this chapter, the spreading function used is the cos-2s type of Eq. 2.10:

$$\begin{cases} D(k,\phi) = \cos^{2s}(\frac{\phi_{wind}-\phi}{2}) & \\ s = 9.77\left(\frac{k}{k_m}\right)^{\mu} & \\ \mu = 4.06 & \text{if } k < k_m, \\ \mu = -2.34 & \text{if } k > k_m \end{cases} \tag{2.10}$$

where:

- ϕ_{wind} is the wind direction.
- $k_m = (g2\pi)/U^4$. The wind speed U is directly related to the significant wave height in the Douglas scale (cf. table 2.1).

The spreading function is oriented along an average directional angle ϕ_{wind}. It means that a main direction must be defined which corresponds to the direction of the main phenomenon of the sea (the current or the wind direction for example). The representation of this function with ϕ_{wind} is given in Fig. 2.3.

Discretization of the sea surface elevation As we have seen in the previous parts, the sea surfaces are generated assuming a Pierson Moskovitz spectrum and a cos-2s spreading function. The sea surfaces has to be discretized in order to perform numerical simulation. At a time t_k, $z^s_{i,j,k}$ is defined in Eq. 2.11 as the sea elevation of the discretized sea surface at the horizontal position x^s_i and y^s_j.

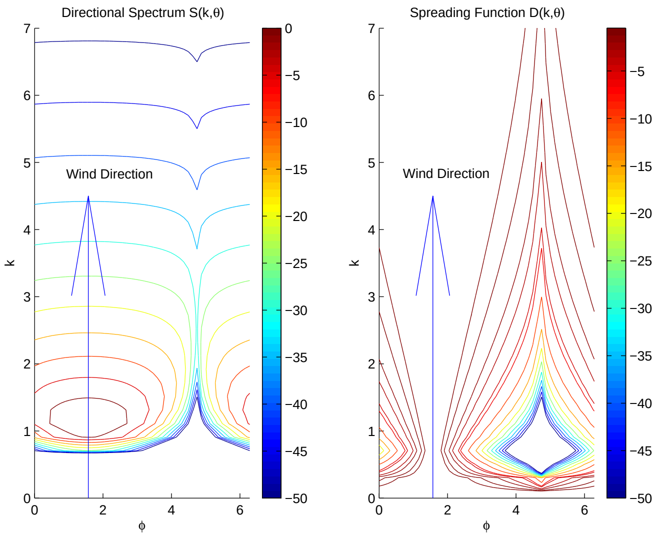

Figure 2.3: Directional Spectrum $S(k, \phi)$ with its associated Spreading function $D(k, \phi)$ in cos-2s type

$$\left\{ \begin{array}{rcl} x_i^s & = & (i-1)\Delta x, \;\; i = 1, ..., N_x \\ y_j^s & = & (j-1)\Delta y, \;\; j = 1, ..., N_y \\ z_{i,j,k}^s & = & \xi(x_i^s, y_j^s, t_k) \;\; k = 1, ..., N_t \end{array} \right. \tag{2.11}$$

where Δx, Δy are the spatial sampling steps and ξ is a function which returns the sea elevation $z_{i,j,k}^s$ corresponding to the coordinates x_i^s and y_j^s on the sea surface. All the $z_{i,j,k}^s$ are grouped in the sea surface elevations matrix $\mathbf{Z_k^s}$ defined at time $t_k = (k-1)\Delta t$.

2.2.3 Examples of sea surfaces elevations

The sea surface is modelled as a superposition of different sinusoidal plane waves (cf. Eq. 2.1). The discretized sea surface elevation is then:

$$\xi\left(x_i^s, y_j^s, t_k\right) = \sum_{n}^{N_c} A_n \sin\left[\omega_n t_k - k_{x,n} x_i^s - k_{y,n} y_j^s + \epsilon_n\right] \tag{2.12}$$

with:

$$\vec{k_n} = \left(\begin{array}{c} k_{x,n} \\ k_{y,n} \end{array} \right) \tag{2.13}$$

where A_n is defined from the directional spectrum S and ϵ_n is a random value in $[0, 2\pi[$. It can be also defined by the multiplication of S and of a random matrix which S different realizations of sea surfaces elevations generates from one directional spectrum. N_c is the number of currents describing the sea surface.

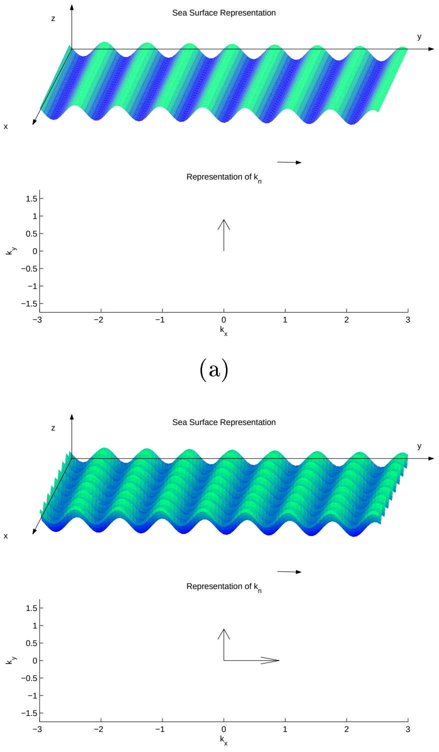

(a)

(b)

Figure 2.4: Representation of the vector $\vec{k}_n$ and its associated sea surface which size is 50 × 50 at a time t_k. (a) $\vec{k}_1 = k_{x,1}\vec{i}$ with $k_{x,1} = 1$ and (b) $\vec{k}_1 = k_{x,1}\vec{i}$ with $k_{x,1} = 1$ and $\vec{k}_2 = k_{y,2}\vec{j}$ with $k_{y,2} = 1$

Simple theorical examples In this section, the effect of the current is illustrated, computed from Eq. 2.11. First, two simple theoretical cases are shown in Fig. 2.4, with $A_n = 1$ and $\omega_n = 0.5$ $\forall n$:

- a sea surface which is defined from one current $N_c = 1$, $(k_{x,1} = 1, k_{y,1} = 0)$
- a sea surface which is defined from two currents $N_c = 2$, the previous one $(k_{x,1} = 1, k_{y,1} = 0)$ plus an orthogonal second current $(k_{x,2} = 0, k_{y,2} = 1)$

The associated directional spectra are defined as one and two Dirac's respectively.

From a Pierson Moskovitz spectrum We now add a lot of plane waves, through the use of the Pierson Moskovitz directional spectrum, defined in Eq. 2.7. Two generated spectra are presented which correspond to the spectra plotted in Fig. 2.2:

- with $H_{1/3} = 4$ m and $k_p = 3,32.10^{-2}$ m^{-1}

- with $H_{1/3} = 8$ m and $k_p = 44,7.10^{-2}$ m^{-1}

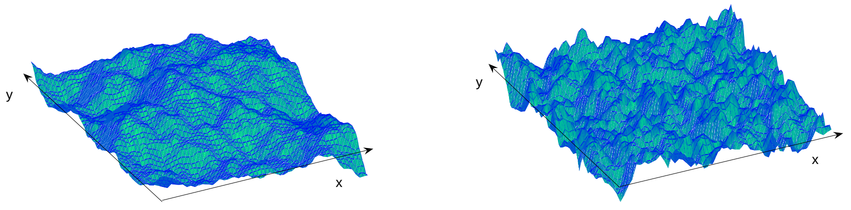

(a) (b)

Figure 2.5: Sea surfaces whose size is 50 × 50 at one time step. (a) $H_{1/3} = 0.3$ m and (b) $H_{1/3} = 4$ m

The same scale is used in both figures. As we can see, the amplitude of the waves is larger in the second case where $H_{1/3}$ is larger (as the energy is larger, cf. section 2.2.2.2). So, in the first case, the sea surface is smoother.

Time evolution of a sea surface A last result (cf. Fig. 2.6) shows the evolution of the sea surface according to time for $H_{1/3} = 4$ m. The simulation was realized for $t_k =$ 1, 5 and 10s.

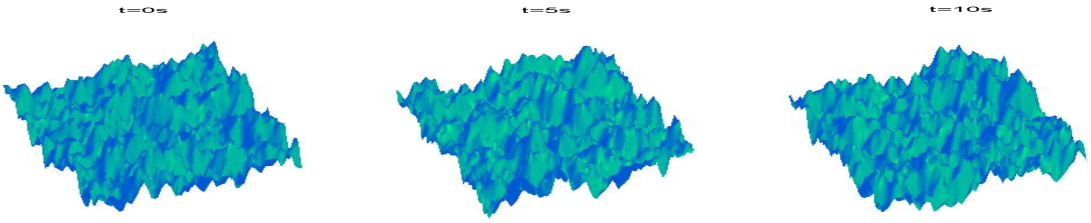

Figure 2.6: Evolution of the sea surface according to time

2.3 Buoy movement modelling

Once the sea surface has been modelled, we now have to consider the movements of the buoys on this surface. The notions of undeformed and deformed array are first presented.

In the second part, a simple numerical modelling of buoys motions is computed over a discretized sea surface which was presented in the first part of this chapter. It introduces a correlation between the shape of the sea surface and the movement of a buoy.

2.3.1 Definition of the system

2.3.1.1 Introduction of the undeformed array

The undeformed array is used as a reference for the evolution of disturbances in the radiation pattern. It is a regular linear array aligned along the x-axis, composed of $N = 10$ elements with $\lambda/2$ interelement spacing, λ being the wavelength at the operating frequency f (cf. Fig. 2.7).

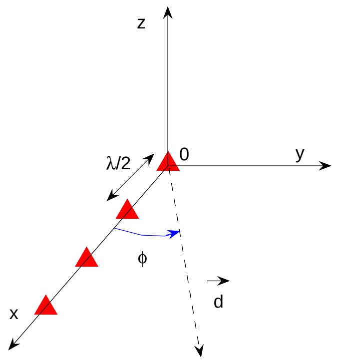

Figure 2.7: Undeformed array

The HF radar is working at 10 MHz, corresponding to $\lambda/2 = 15$ m.

(x_n, y_n, z_n) are the coordinates of buoy n. For the undeformed array, the coordinates of buoy n are $[(n-1)\lambda/2, 0, 0]$. The coordinates of all the elements of the undeformed array are grouped in three vectors X, Y and Z as:

$$\mathbf{X} = [\ x_1,\ x_2,\ \ldots,\ x_N\ ] \tag{2.14}$$

$$\mathbf{Y} = [\ y_1,\ y_2,\ \ldots,\ y_N\ ] \tag{2.15}$$

$$\mathbf{Z} = [\ z_1,\ z_2,\ \ldots,\ z_N\ ] \tag{2.16}$$

2.3.1.2 Definition of the floating system: the deformed array

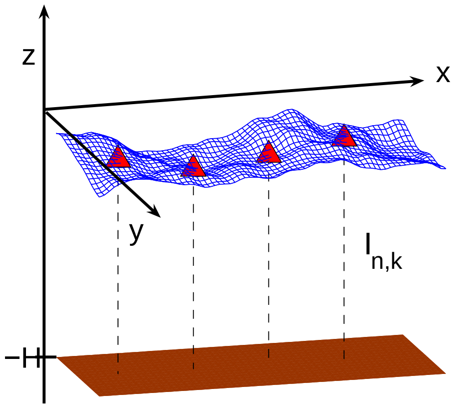

Figure 2.8: Receiving array on buoys on sea surface.

We now assume that each antenna is supported by a buoy, floating on the sea. The deformed array is then defined as the receiving array nom composed by buoys moving on the sea surface.

Each buoy is anchored to the sea bed thanks to a cable attached at a sea depth H referenced from the sea surface reference level (cf. Fig. 2.8 and Fig. 2.9). The length of the cable L defines the maximum authorized displacement of the buoy around its anchorage point. Due to the sea motion and the induced dynamic of buoys, the new coordinates of buoys are defined by $\tilde{X}$, $\tilde{Y}$ and $\tilde{Z}$:

$$\tilde{\mathbf{X}} = [\ \tilde{x}_1,\ \tilde{x}_2,\ \ldots,\ \tilde{x}_N\ ] \tag{2.17}$$

$$\tilde{\mathbf{Y}} = [\ \tilde{y}_1,\ \tilde{y}_2,\ \ldots,\ \tilde{y}_N\ ] \tag{2.18}$$

$$\tilde{\mathbf{Z}} = [\ \tilde{z}_1,\ \tilde{z}_2,\ \ldots,\ \tilde{z}_N\ ] \tag{2.19}$$

This deformation of the receiving array on the sea surface introduces deformation of the radiation pattern.

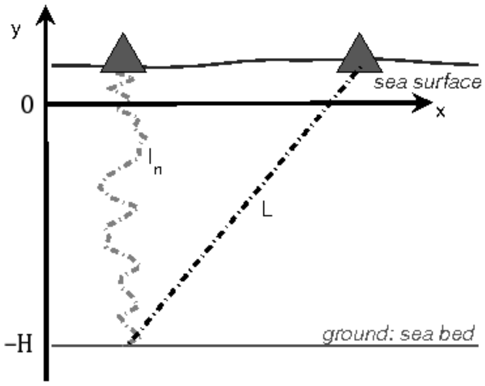

Figure 2.9: Definition of L, the length of the cable.

2.3.2 Modelling of buoys motions

The buoys motions are calculated from the sea surface model presented in section 2.2.2.

In order to consider a receiving array with N antennas, the minimum length of the underlying sea surface patch has to be equal to $(N+1)\lambda/2 = 165$m. The typical values we have chosen for Eq. 2.11 are:

- $N_x = N_y = 210$
- $\Delta x = \Delta y = 1$ m
- $N_t = 60$ and $\Delta t = 0.2$s

2.3.3 Buoys displacements

In this section, a simple algorithm is proposed to compute the different positions of buoys on the sea. These positions are obtained from the shape of the sea surface. We note $(\tilde{x}_{n,k}, \tilde{y}_{n,k}, \tilde{z}_{n,k})$ the positions of buoy n at time k. The algorithm can be decomposed into six steps:

1. The initial coordinates of buoy n $(\tilde{x}_{n,1}, \tilde{y}_{n,1})$ are set to the horizontal coordinates (x_n, y_n) of the undeformed array.
2. At time $k+1$, the buoy moves to a new position $(\tilde{x}_{n,k+1}, \tilde{y}_{n,k+1})$ given by:

$$\left\{ \begin{array}{lcl} \tilde{x}_{n,k+1} & = & \tilde{x}_{n,k} + \nu \Delta t \cos \phi_{n,k} \\ \tilde{y}_{n,k+1} & = & \tilde{y}_{n,k} + \nu \Delta t \sin \phi_{n,k} \end{array} \right. \tag{2.20}$$

where ν is a coefficient representing the displacement speed of buoy over the sea and $\phi_{n,k}$ is the angular value ϕ of the new position relative to the old one, which has been defined using the steepest slope of the sea surface around the initial point $(\tilde{x}_{n,k}, \tilde{y}_{n,k})$:

$$\phi_{n,k} = \arctan\left(\frac{\frac{\delta\xi}{\delta y}(\tilde{x}_{n,k}, \tilde{y}_{n,k})}{\frac{\delta\xi}{\delta x}(\tilde{x}_{n,k}, \tilde{y}_{n,k})}\right) \tag{2.21}$$

3. The corresponding elevation $\tilde{z}_{n,k}$ directly depends on the horizontal positions of the buoy and is computed from the values $(\tilde{x}_{n,k}, \tilde{y}_{n,k})$ (Eq. 2.11).

4. $l_{n,k}$ is the distance between the anchorage point and the position of buoy n at time t_k (Eq. 2.22). Its value must be kept smaller than the length of the cable L (cf. Fig. 2.9).

   $$l_{n,k} = \sqrt{(\tilde{x}_{n,k} - x_n)^2 + (\tilde{y}_{n,k} - y_n)^2 + (\tilde{z}_{n,k} + H)^2} \tag{2.22}$$

   For each buoy, $l_{n,k+1}$ is compared to the value of L. If $l_{n,k+1} > L$, the new positions $(\tilde{x}_{n,k+1}, \tilde{y}_{n,k+1})$ are limited by D:

   $$D = \sqrt{L^2 - (\tilde{z}_{n,k} + H)^2} \tag{2.23}$$

   which is the maximum possible horizontal displacement of the buoy.

5. Time incrementation, $k = k + 1$.

6. If $k < N_t$, we return to step 2 otherwise the algorithm is stopped.

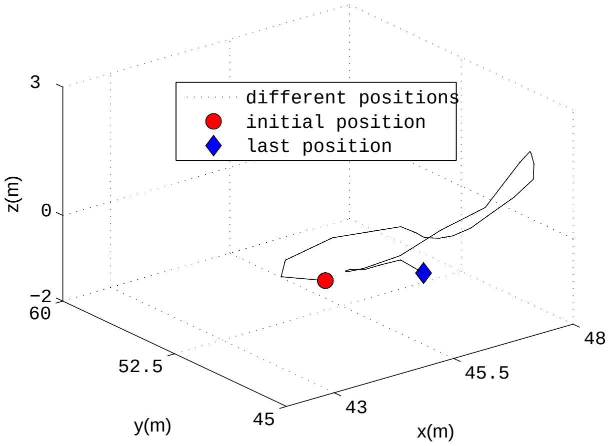

Figure 2.10: Example of antenna displacements.

An example of antennas displacements is given in Fig. 2.10. It shows the temporal evolution of the buoy around its initial position.

2.3.4 Maximum displacement of buoy motion

We have seen that the bouy movement is limited by its physical structure. So, the buoys are not completely free of their movements. They have a maximum displacement in all the direction around their initial position.

As the buoy follows the sea surface, the maximum vertical displacement is fixed by the sea elevations. The horizontal displacement is limited by its cable which imposes its maximum value.

In extreme cases, when the sea state is large, the maximum vertical displacement Δv_{max} could correspond to the significant wave height of the sea (for example with a sea state of 4, $H_{1/3} = 6$ m). If this value is expressed in λ, the maximum vertical displacement could be equal to $\lambda/2$ (with the same example, for $f = 25$ MHz, $\lambda = 12$ m and thus $\Delta v_{max} = H_{1/3} = \lambda/2$).

The maximum horizontal displacement Δh_{max} corresponds to the interelement spacing of the receiving array. In Chapter 1, the distance between two antenna is equal to $\lambda/2$, so $\Delta h_{max} = \lambda/2$. For that the buoys do not have a common displacement area Δh_{max} has to be limited to $\lambda/4$ (cf Fig. 2.11).

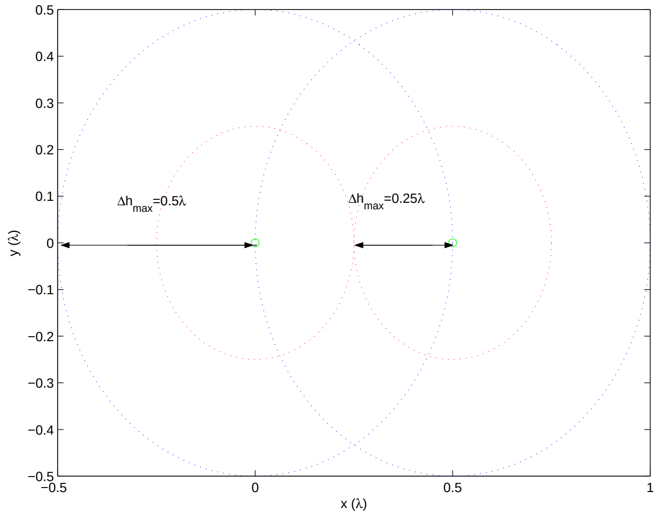

Figure 2.11: Common area displacement between two buoys.

2.4 Conclusion of Chapter 2

This chapter has introduced the modelling we use for the calculation of the surface elevation matrix Z_k^s, evolving in time. A new algorithm has been proposed to model the buoys motions from Z_k^s. This algorithm will be useful to quantify the disturbances generated by the array deformations and to test the corrections methods developped in the next chapter.

Chapter 3

Correction methods

3.1 Introduction

As we have seen, we need to use a large receiving array to improve the azimuth detection of a HFSWR radar. However, the available space on the coast is often reduced and it could limit the number of antennas in the receiving array. So the deployment of the radar (and more particularly the receiving array) on the coast is one of the encountered problems.

The alternative challenging solution investigated in Chapter 2 is to use antennas on buoys over the sea surface. Thus, the location of the HFSWR can be found more easily (the restrictions on sea surface are not so drastic) but this new deployment introduces new issues related to the array deformation with sea motion. This chapter is focused on the disturbances generated by the deformations of the receiving array and proposes specific correction methods to limit their effects.

In Chapter 2, the notions of undeformed and deformed array have been presented. The undeformed array is used as a reference for the evaluation of disturbances in the radiation pattern. The deformed array is defined as the receiving array on buoys moving on the sea surface. A simple numerical modelling of buoys motions over a discretized sea surface has been presented. It introduces a correlation between the shape of the sea surface and the movement of a buoy. Thus, the deformation of the receiving array on buoys can be quantified, and the associated disturbances in the radiation pattern is investigated.

A first consequence of the displacement of the antenna elements is the modification of the coupling over the array. This problem will be investigated in the first part of the chapter. The second consequence is the modification of the positions of the antenna elements that change the very geometry of the array. This "deformation" of the array will be addressed in the second part of the chapter. The various sources of disturbances are studied depending on the type of displacement i.e. the vertical (along z axis) and the horizontal movements (along x and y axis).

The proposed correction methods consist of a modification of the excitation coefficients of the array and can be regarded as array synthesis techniques. Finally, they are also compared to more conventional array synthesis techniques (using Genetic Algorithms or Particle Swarm Optimization) in order to assess their performance regarding processing time.

3.2 Study of coupling

On buoys, the receiving array is deformed by the sea surface movement (cf Chapter 2). With deformations, using passive resonant antennas, the coupling in the array changes and it can be responsible for disturbances in the radiation pattern. The next section of this chapter is focused on the coupling influence in a deformed array.

3.2.1 Introduction of the coupling

We first consider the simple case of mutual coupling between two $\lambda/2$ dipoles. The typical interelement spacing we will use is $\lambda/2$ so the mutual impedance cannot be neglected [23]. We will then extend the investigation to a 10-element array.

3.2.2 Mutual Impedance of two dipoles

We consider the case of two vertical $\lambda/2$ dipoles as shown in Fig. 3.1. We will investigate the modification of the mutual coupling when the position of the second dipole with respect to the first one is varied.

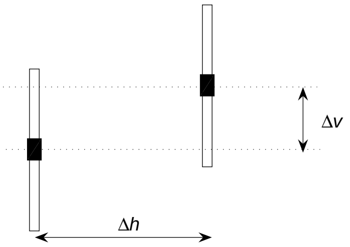

Figure 3.1: Parallel dipoles

Two displacements parameters are considered:

- Δh is the horizontal displacement of the moving antenna

- Δv is the vertical displacement of the moving antenna

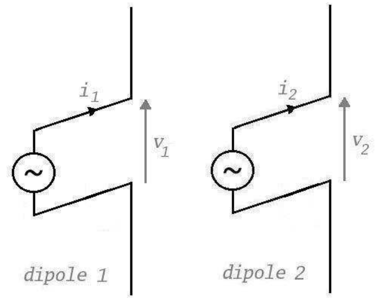

Figure 3.2: Representation of the coupling between two dipoles

Using the conventions presented in Fig. 3.2, the mutual coupling is defined by the $\mathbf{Z^{MU}}$ matrix with:

$$\begin{aligned} v_1 &= i_1 Z_{11}^{MU} + i_2 Z_{12}^{MU} \\ v_2 &= i_1 Z_{21}^{MU} + i_2 Z_{22}^{MU} \end{aligned} \tag{3.1}$$

More precisely, the mutual impedance is given as

$$Z_{21}^{MU} = \left. \frac{v_2}{i_1} \right|_{i_2=0} \tag{3.2}$$

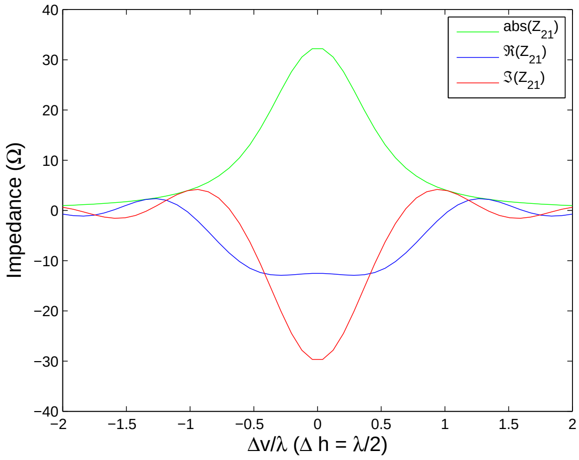

Figure 3.3: Mutual coupling between 2 dipoles depending on the vertical placement

Fig. 3.3 and 3.4 present the variations of Z_{21}^{MU} versus Δh and Δv respectively.

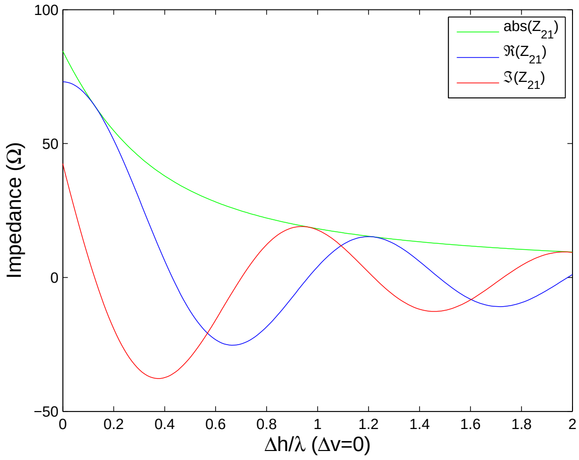

Figure 3.4: Mutual coupling between 2 dipoles depending on the horizontal espacement

The simulations are performed using NEC at 12 MHz [2]. However, in practice, to reduce the computational cost, we can use a Matlab toolbox (EWA) [1] defined with an analytic model without using the way of electromagnetic simulations. The dimensions of the dipoles are in $\lambda/2 = 12.5$ m. For simplicity, we consider dipoles in free space which means the effect of the sea is not taken into account.

Fig. 3.3 shows that the effect of the vertical displacement can be significant. The magnitude of Z_{21}^{MU} varies from 19 Ω to 32 Ω where Δv is moved from $\lambda/2$ to 0. However, is has been shown in Chapter 2 that the expected vertical displacements were much smaller (at 10 MHz, $\lambda/2$ is about 15 m which is not a realistic wave height for typical weather conditions).

For $\lambda/10$ vertical displacements (which corresponds to 3 m wave heights), the modification in mutual coupling is not so high (only 4 Ω in magnitude). As a conclusion, variations in mutual coupling do not appear as a major issue for typical vertical displacements as those we can expect for a realistic sea surface.

For horizontal deformations, the displacements can be much larger and the modifications in the coupling cannot be neglected.

3.2.3 Coupling in an N-antenna array

As we have defined the mutual impedance of two dipoles (cf Eq. 3.3), we can generalize this expression to an array of N dipoles:

$$\begin{array}{rcl} v_1 & = & i_1 Z_{11}^{MU} + i_2 Z_{12}^{MU} + \cdots + i_N Z_{1N}^{MU} \\ v_2 & = & i_1 Z_{21}^{MU} + i_2 Z_{22}^{MU} + \cdots + i_N Z_{2N}^{MU} \\ \vdots & = & \vdots \\ v_N & = & i_N Z_{N1}^{MU} + i_N Z_{N2}^{MU} + \cdots + i_N Z_{NN}^{MU} \end{array} \tag{3.3}$$

For a N-element array, it is not so easy to represent the variations of the mutual coupling when the positions of the different elements are modified.

Here, we prefer to consider the evolution of the magnitude of the electric current at the middle of a dipole.

For clarity, we adopt a normalized representation of the currents. The reference value I^{ref} is the current on the central dipole (with an odd number of antennas) or one of the two central dipoles (with an even number of antennas) of a non deformed array with uniform excitation.

The normalized currents are defined as:

$$i_n = \frac{I_n}{I_{ref}} \times 100 \tag{3.4}$$

where I_n is the non normalized current on dipole n and i_n is a percentage.

3.2.4 Currents with vertical deformation in the array

Fig. 3.5 represents all the currents i_n with $n = 1, \ldots, N$ considering a vertical deformation in the array. Each column in the graph corresponds to an array in which each of the 10 different antenna elements exhibits a vertical deviation Δv_n. Δv_n is a value that is arbitrarily chosen in the interval $[-\Delta v_{max}, +\Delta v_{max}]$.

Practically, the antennas positions are computed as follows:

$$\begin{array}{rcl} \tilde{x}_n & = & x_n \\ \tilde{y}_n & = & y_n \\ \tilde{z}_n & = & z_n + (2r_n - 1)\Delta v_{max} \end{array} \tag{3.5}$$

where ($\tilde{x}_n$,$\tilde{y}_n$,$\tilde{z}_n$) and (x_n,y_n,z_n) are respectively the coordinates of antenna n in the undeformed and deformed array and $\mathbf{R} = [\ r_1\ \ldots\ r_N\ ]$ is a random vector with each r_n which is defined with a uniform distribution on the unit interval.

In fact, 100 different simulations are performed for each column corresponding to 100 different random configurations of the array with the same maximum deviation Δv_{max}.

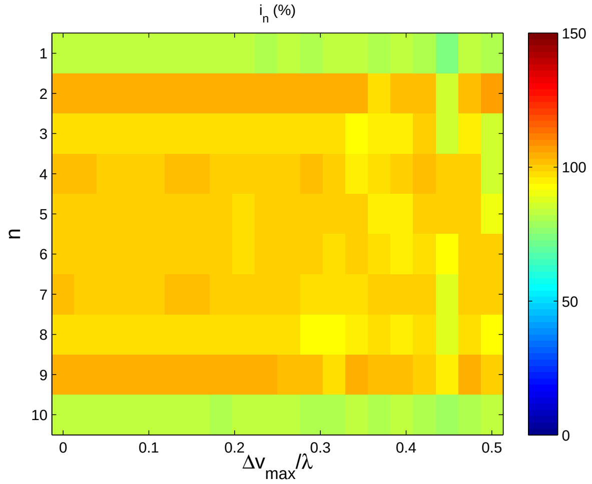

Figure 3.5: Current representation according to the vertical Δv deformation in the array

The first column ($\Delta v_{max} = 0$) corresponds to the undeformed array. We can notice that the currents in all 10 elements are not perfectly identical due to the finite dimension of the array. Variations are observed at both extremities (for antenna 1 and 2, respectively 10 and 9).

When Δv_{max} is increased, the dispersion in currents is larger (right area in Fig. 3.5). However, the maximum deviation is less than 10 %. This confirms that the disturbance due to mutual coupling are small (especially if we only consider $\frac{\Delta v_{max}}{\lambda} \leq 0.1$ as stated before).

3.2.5 Currents with horizontal deformation in the array

Fig. 3.6 represents all the currents i_n with $n = 1, \ldots, N$, considering horizontal deformation in the array. The only difference with the previous section is that the position of the moving antennas is now:

$$\begin{array}{rcl} \tilde{x}_n & = & x_n + (2rx_n - 1)\Delta h_{max} \\ \tilde{y}_n & = & y_n + (2ry_n - 1)\Delta h_{max} \\ \tilde{z}_n & = & z_n \end{array} \tag{3.6}$$

where $\mathbf{Rx} = [\ rx_1 \ \ldots \ rx_N\ ]$ and $\mathbf{Ry} = [\ ry_1 \ \ldots \ ry_N\ ]$ are random vectors, each rx_n and each ry_n is defined with a uniform distribution on the unit interval.

The variations of current in the array can be large. Even if Δh_{max} is weak, if two antennas of the array get closer, their movement is combined, amplifying their coupling (and limiting their effect on the others antennas). Moreover, when Δh_{max} is larger than

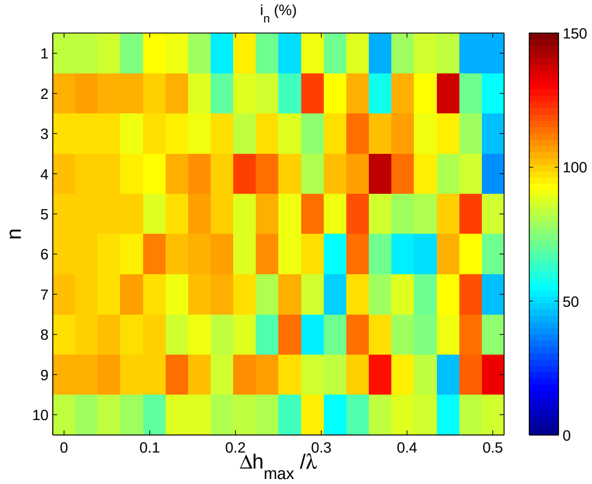

Figure 3.6: Current representation according to the horizontal deformation Δh in the array

0.1λ, the coupling can radically change the current value on a dipole.

An example of current repartition in an array is given in Fig. 3.7. The dotted line corresponds to the magnitude of the current in the array without deformation. The solid line corresponds to the repartition of currents in the deformed array. In the array without deformation, the repartition of the current is uniform and close to I_{ref}, except for the two extreme antennas (antenna 1 and antenna 10). With the deformed array, the repartition of current is not uniform anymore. So, in this case, the coupling effect is very important and it has to be limited.

3.2.6 Conclusion on coupling effect in the deformed array

This brief study of the modification of the coupling in the array permits to draw a few conclusions:

- the modification of coupling for vertical displacements should remain small, especially because of the reduced amplitude of vertical motions that is expected for realistic sea surfaces.
- it could be much higher for horizontal displacements firstly because larger displacements are expected, secondly because the distance between two dipoles (which controls the coupling) combines the effect of two displacements.

3.2.7 Coupling effect on the radiation pattern

We now show that the modification of coupling is not always the major cause in the modification of the array pattern.

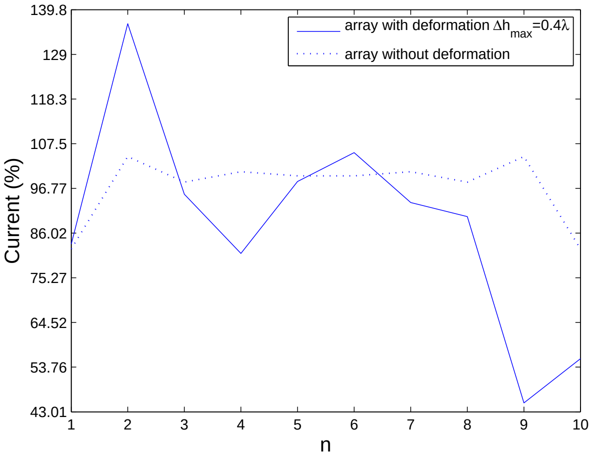

Figure 3.7: Currents repartitions in a deformed array and in an array without deformation

To do so, we compare three different radiation patterns. Their simulation are realized with a uniform 10-antenna array with an interelement spacing equal to $\lambda/2$ (cf Chapitre 1). The first one is the radiation pattern of an undeformed array, the second one is that of a deformed array with coupling effect and the last one is that of a deformed array without coupling. The three radiation patterns are simulated for two different deformations: the vertical and the horizontal. The maximum horizontal and vertical displacement which are used during these simulation are defined with $\Delta h_{max} = \Delta v_{max} = 0.25\lambda$.

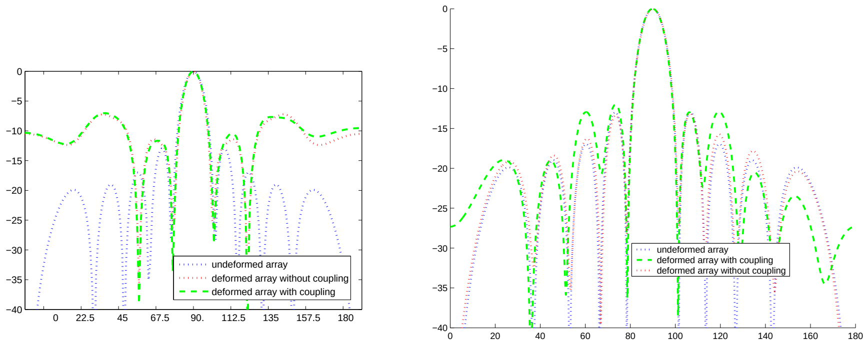

(a) (b)

Figure 3.8: Coupling effect and horizontal deformation (a) and vertical deformation (b) effect on the radiation pattern

Fig. 3.8 represents this comparison. In Fig. 3.8 (a), the two radiation patterns of the deformed array are very close and they exhibit significant disturbances compared to the radiation pattern of the undeformed array. This demonstrates that the horizontal deformation of the array is the most important source of disturbances. In Fig. 3.8 (b), the disturbances are weak whatever the sources of disturbances, (coupling or deformation).

We have seen that the disturbance in the radiation pattern of the array is not only due to the modification in the coupling: the variation of the geometry of the array is often the major issue. This is particularly the case for horizontal displacements of the antennas where the effect of the coupling is negligible compared to the effect of the deformation.

This suggests the procedure that will be used for the correction procedure.

3.3 Receiving array with a vertical deformation

The deformation of the array due to sea movement is responsible for perturbations in the radiation pattern. The purpose of this section is to propose correction procedures that compensate for the deformation. The main assumption is that the position of the antenna elements in the deformed array can be known with a sufficient accuracy. When this condition is satisfied, we show that a judicious modification of the weighting coefficients can be used to compensate for the displacements.

In a vertical displacement [11], there is no physical deformation in the observation plane (xOy), so the main disturbances come from the modification of the coupling in the array when the dipoles move vertically. Although these disturbances are usually small, they can be corrected easily.

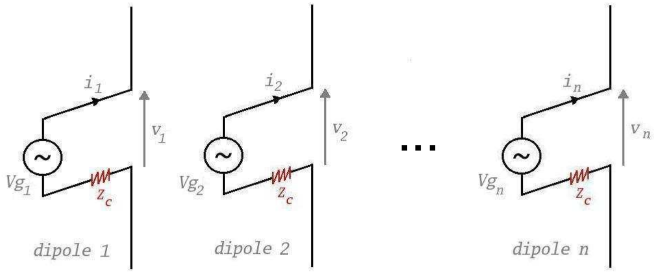

Figure 3.9: Representation of the coupling in a dipole.

Let $\mathbf{I} = [\ i_1,\ i_2,\ \ldots,\ i_N\ ]^T$ be the currents in the antenna ports that produce the desired radiation pattern. The impressed voltages $\mathbf{V_g} = [\ v_{g1},\ v_{g2},\ \ldots,\ v_{gN}\ ]^T$ can be defined as:

$$\mathbf{V_g} \;=\; (\mathbf{Z} + \mathbf{Z_g I_d})\,\mathbf{I} \tag{3.7}$$

where $\mathbf{Z_g}$ is the source impedance, $\mathbf{Z^{MU}}$ is the impedance matrix (representing coupling) and $\mathbf{I_d}$ is the identity matrix.

For simplicity, in the following example, $\mathbf{Z^{MU}}$ is built from the mutual impedance of two parallel dipoles in free space for different vertical shifts between the antennas [23].

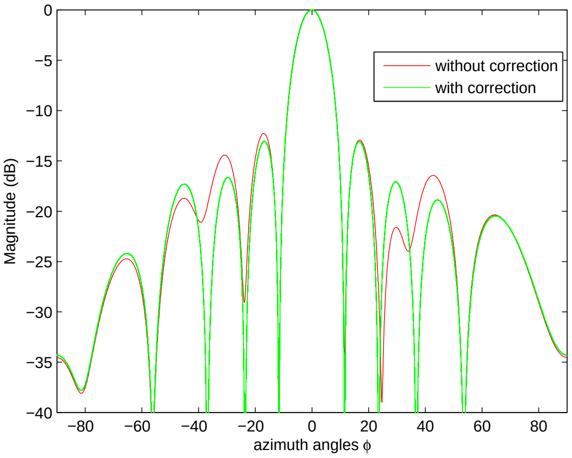

Figure 3.10: Radiation pattern of 10-antenna array with a vertical deformation and with uniform weights, with and without correction with a $\Delta v_{max} = 0.25\lambda$.

Fig. 3.10 illustrates the effect of the correction procedure. These simulations are computed with a 10-antenna array with an interelement spacing equals to $\lambda/2$. The case without deformation corresponds to a uniform array with vertical deformation (modifying the z coordinates of antennas. The case with correction is the same array changing the uniform weights by the weights given by the correction method. We used $\Delta v_{max} = 0.25$. It compares the radiation patterns obtained for two different impressed $\mathbf{V_g}$.

The case 'without correction' corresponds to an array where the z coordinates of the antennas are different but $\mathbf{V_g}$ is calculated using the $\mathbf{Z}$ matrix of the undeformed array. The case 'with correction' corresponds to the same array but it now utilizes the actual $\mathbf{Z^{MU}}$ matrix of the deformed array. As can be seen, the correction procedure results in a significant decrease of the sidelobe level.

3.3.1 Robustness of the vertical correction method

In the previous section, the mutual coupling $\mathbf{Z^{MU}}$ is prefectly known. This approach is not realistic and it could be interesting to study the robustness of the correction method with $\mathbf{Z^{MU}}$ partially unknown. This section is focused on this point.

So, we define $\mathbf{\Delta Z^{MU}}$ as a matrix of errors which can be added to $\mathbf{Z^{MU}}$:

$$\mathbf{\tilde{Z}^{MU}} = \mathbf{Z^{MU}} + \mathbf{\Delta Z^{MU}} \tag{3.8}$$

where $\mathbf{\tilde{Z}^{MU}}$ is the noisy matrix.

Each coefficient of the error matrix is a real random number. We assume a uniform distribution in the range $[-4\Omega, 4\Omega]$. The maximum error (4Ω) corresponds to 11% of the maximum coupling coefficient for the considered configuration when $\Delta_v = 0$ and $\Delta_h = \lambda/2$.

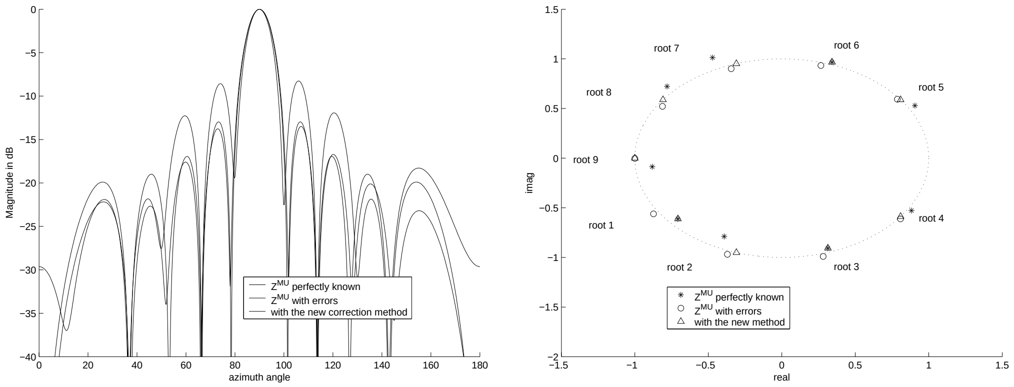

(a) (b)

Figure 3.11: (a) Radiation patterns with the two different corrections methods (b) their representations of the positions of the roots of the associated polynomial

Fig. 3.11 (a) shows the radiation pattern applying the vertical correction method when the coupling is perfectly known and when errors are added. Fig. 3.11 (b) represents the positions of the roots of the associated polynomial. The simulation was realized for $\Delta v_{max} = 0.25\lambda$. As can be seen, large increases of SLL appear when the coupling matrix that is used for correction is not perfectly characterized. This can be interpreted using the Shelkunoff's representation. We remind that it relies on the analysis of the associated polynomial $F(z) = \sum i_n z^n$. Here, i_n is the n^{th} coefficient of the current vector $\mathbf{I} = \left(\mathbf{Z^{MU}} + \mathbf{Z_g}\right)^{-1} \mathbf{V_g}$.

This equation shows that the i_n coefficients are modified when the coupling $\mathbf{Z^{MU}}$ is changed. As a result, the associated polynomial is also modified and this causes a displacement of the roots in the Shelkunoff representation (cf Fig. 3.11 (b)).

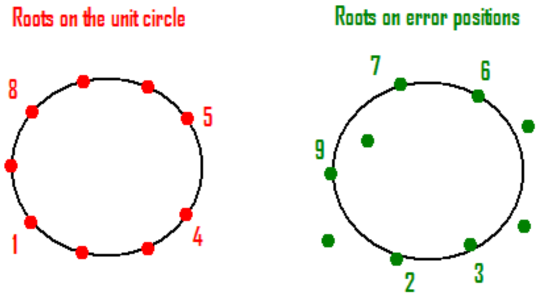

Figure 3.12: Example of roots displacement

Using this representation, an improved correction is proposed. It consists of identifying the few roots whose position has been significantly modified and move them back at their initial position. Fig. 3.12 gives an illustration where roots 1, 4, 5 and 8 have to be moved back on the unit circle.

If we go deeper into technical details, two issue have to be discussed. The first one is the criterion that is used to decide which roots have to be displaced. This can be done by measuring the distance between the initial position and the 'erroneous' one. If it exceeds a given threshold, the displacement process is actived. The second issue is the mechanism that is used to bring back a root to its initial position. This is done by imposing the initial value of the roots at the 'erroneous' one.

In practice, both issue can be addressed simultaneously by optimizing the positions of the roots thanks to optimization routines such as genetic algorithm.

Fig. 3.11 (a) shows the improvement of the results with this new correction method. The increases of sidelobes are limited, compensating for errors in $\mathbf{Z^{MU}}$. The displaced roots chosen during the correction method are exposed in Fig. 3.11 (b).

To conclude, the new correction method drastically limits the increases of SLL generated by the errors in the mutual coupling matrix. Moreover, the new correction method inspired from the Shelkunoff's representation has a double utility:

- it quantifies the errors in $\mathbf{Z^{MU}}$ to know if the correction method can be applied
- it finds the roots which are responsables for the disturbances when $\mathbf{Z^{MU}}$ is erroneous

3.4 Horizontal deformations of the receiving array

For horizontal movements, the problem is a bit different. We first consider the longitudinal movement (along the array axis, (O, x)). The main disturbance does not result from coupling modifications but from the modification of the interelement spacing in the array. The deformed array can be seen as a linear array with a non regular interelement spacing (cf Fig. 3.13).

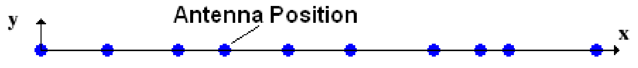

Figure 3.13: Longitudinal deformation

The coupling is a secondary effect that could be accounted for as in Section 3.3 and will not be discussed again here.

3.4.1 Compensation method for longitudinal movement

We assume that the antennas positions are perfectly known. The principle of the proposed correction method consists in balancing the changes in the interelement spacing by a modification of the excitation coefficients. Haupt has studied the reciprocal problem in [17]. In the following, i_n is the current in antenna n for the undeformed array and $\tilde{i}_n$ is the corresponding coefficient to be used in the deformed array. The compensations can be realized by forcing the coefficients so that the nulls of the radiation patterns correspond to those of the undeformed array. A linear system is then obtained:

$$\sum_{n=1}^{N} \tilde{i}_n e^{jk\tilde{x}_n u_m} = \sum_{n=1}^{N} i_n e^{jkx_n u_m} \quad m = 1, ..., N-1 \tag{3.9}$$

where $u_m = \cos\phi_m$ and ϕ_m is the azimuth angle of null m in the radiation pattern. Eq. 3.9 represents a linear system of $N-1$ equations for N unknowns. We choose to set $\tilde{i}_N = 1$ to fix the proportionality level of all the weights $\tilde{i}_n$. Eq. 3.10 is the new linear system which has to be solved.

$$\sum_{n=1}^{N-1} \tilde{i}_n e^{jk\tilde{x}_n u_m} = \sum_{n=1}^{N} i_n e^{jkx_n u_m} - e^{jk\tilde{x}_N u_m} \quad m = 1, ..., N-1 \tag{3.10}$$

Eq. 3.10 can be rewritten in the following matrix representation with $\tilde{X}_1 = [\ \tilde{x}_1\ \tilde{x}_2\ \ldots\ \tilde{x}_{N-1}\ ]$.

$$\tilde{\mathbf{E}}\tilde{\mathbf{I}}_1 = \mathbf{EI} - \mathbf{A} \tag{3.11}$$

with

$$\mathbf{U} = [\ u_1\ u_2\ \dots\ u_{N-1}\ ]^T \tag{3.12}$$

$$\mathbf{E} = \exp\left(jk\mathbf{U}\mathbf{X}\right) \tag{3.13}$$

$$\tilde{\mathbf{E}} = \exp\left(jk\mathbf{U}\tilde{\mathbf{X}}_{\mathbf{1}}\right) \tag{3.14}$$

where $\tilde{\mathbf{I}}_{\mathbf{1}} = [\ \tilde{i}_1\ \tilde{i}_2\ \dots\ \tilde{i}_{N-1}\ ]^T$ and $\mathbf{A} = [\ e^{jk\tilde{x}_N u_1}\ e^{jk\tilde{x}_N u_2}\ \dots\ e^{jk\tilde{x}_N u_{N-1}}\ ]^T$. When $\mathbf{I}$ is known, we can easily compute $\tilde{\mathbf{I}}_{\mathbf{1}}$ with Eq. 3.15.

$$\tilde{\mathbf{I}}_{\mathbf{1}} = \tilde{\mathbf{E}}^{-1}\left(\mathbf{E}\mathbf{I} - \mathbf{A}\right) \tag{3.15}$$

and $\tilde{I}$, which corresponds to all the correction weights, is easily found:

$$\tilde{\mathbf{I}} = [\tilde{\mathbf{I}}_{\mathbf{1}}^T, 1]^T \tag{3.16}$$

In the next part, the correction method is extended when both longitudinal and transverse movements are considered.

3.4.2 Methods for joint longitudinal and transverse movements

The transverse and longitudinal corrections can be realized simultaneously. A new linear system is then defined (Eq. 3.17):

$$\sum_{n=1}^{N} \tilde{i}_n e^{jk(\tilde{x}_n u_m + \tilde{y}_n u'_m)} = \sum_{n=1}^{N} i_n e^{jkx_n u_m} \quad m = 1, ..., N-1 \tag{3.17}$$

with $u'_m = \sin\phi_m$.

For longitudinal deformations, the resulting deformed array is a linear array with non equidistant elements. For both longitudinal and transversal deformations, the array is not linear anymore.

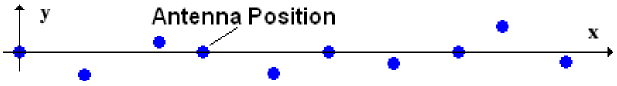

Figure 3.14: Longitudinal and transerve deformation

As a result, the array factor does not exhibit any rotation invariance. Eq. 3.17 is used to set the nulls for the front radiation only ($\phi \in [0, \pi]$). No control on the back radiation is possible. This is not a problem for the foreseen application as no received power is expected from the back. We define the new expression u'_m:

$$\mathbf{U'} = [\ u'_1\ u'_2\ \dots\ u'_{N-1}\ ]^T \tag{3.18}$$

the new matrix $\tilde{\mathbf{E}}$ is given by:

$$\tilde{\mathbf{E}} = \exp\left(jk\left(\mathbf{U}\tilde{\mathbf{X}}_\mathbf{1} + \mathbf{U'}\tilde{\mathbf{Y}}_\mathbf{1}\right)\right) \tag{3.19}$$

with $\tilde{\mathbf{Y}}_\mathbf{1} = [\ \tilde{y}_1\ \tilde{y}_2\ \dots\ \tilde{y}_{N-1}\ ]$ and the currents to be used are given by Eq. 3.15 and Eq. 3.16 where A is new given by $\mathbf{A} = \left[\ e^{jk(\tilde{x}_N u_1 + \tilde{y}_N u'_1)}\ e^{jk(\tilde{x}_N u_2 + \tilde{y}_N u'_2)}\ \dots\ e^{jk(\tilde{x}_N u_{N-1} + \tilde{y}_N u'_{N-1})}\ \right]^T$. Using this formulation, an example is given in the next section.

3.4.3 Results for the horizontal correction method

Fig. 3.15, is a 2 D color plot of the radiation pattern versus time for an array on a moving sea. The color scale corresponds to the relative magnitude of the field (in dB). The sea surface is modeled at each time step as explained in Chapter 2. The resultant deformation of the array is deduced, from which the radiation is computed. Fig. 3.15 (a) corresponds to the case where no correction is applied while Fig. 3.15 (b) accounts for the improvements brought by the correction method. A classical 1D radiation pattern can be obtained at each time step by selecting a specific abscissa in the 2D plots (see Fig. 3.18 that gives a 1D cut at t = 2s). An explanation of the graph construction is given in Fig. 3.17.

Three different kinds of displacements (generating more and more disturbances in the receiving array) are studied corresponding to three different sea states (their values being 1, 3 and 6). Fig. 3.15 represents the radiation pattern versus time with and without correction. Fig. 3.16 represents the same radiation pattern when a -3 dB threshold is applied for better clarity. It shows the direction of the main beam and the -3 dB beamwidth with and without correction respectively:

- For sea state 1, the sea is smooth (cf Table 2.1, Chapter 2) and the deformations in the array are small. The sidelobe level slightly increases in specific directions of ϕ (cf Fig. 3.15 (a)). The main beam direction is not affected by the sea movement (cf Fig. 3.16 (a)),
- For sea state 3, the sea is moderate and the deformations generate stronger disturbances in the radiation pattern (cf Fig. 3.15 (c)). The sidelobe level increases up to -6.6 dB (at t=10 s). For this sea state, the main beam direction is also not significantly affected (cf Fig. 3.16 (c)),
- For sea state 6, the disturbances in the radiation pattern are very large (cf Fig. 3.15 (e) and 3.16 (e)). The direction of the main beam is changing significantly and the sidelobe level can be very high (for example one may observe a sidelobe level reaching up to -2.4 dB, at time t=10 s).

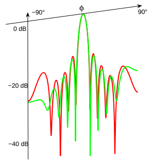

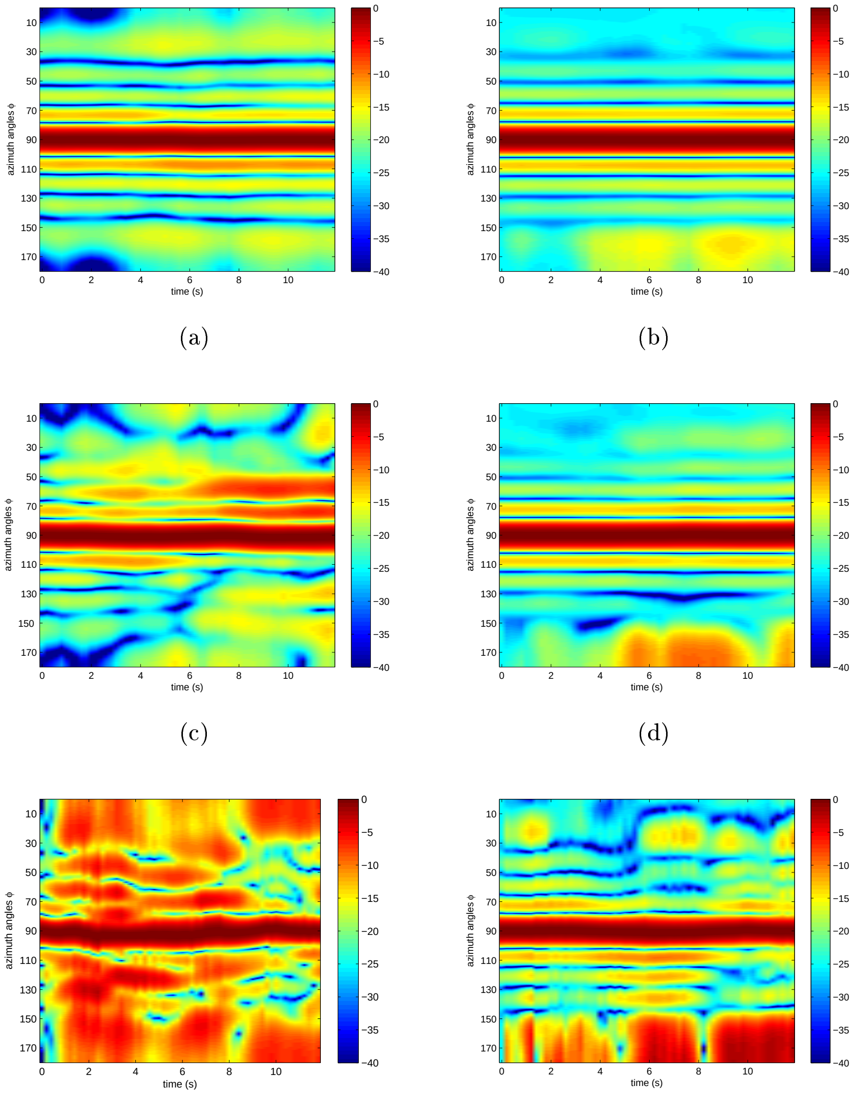

(a) (b)

(c) (d)

(e) (f)

Figure 3.15: Array factor without correction (a) (c) (e) and with correction (b) (d) (f) for sea state 1: (a) and (b), sea state 3: (c) and (d), sea state 6: (e) and (f)

However, our correction maintains the direction of the main beam and the -3 dB beamwidth (10° with a main direction equals to 0° in Fig. 3.15 (b) (d) (f)) compared to

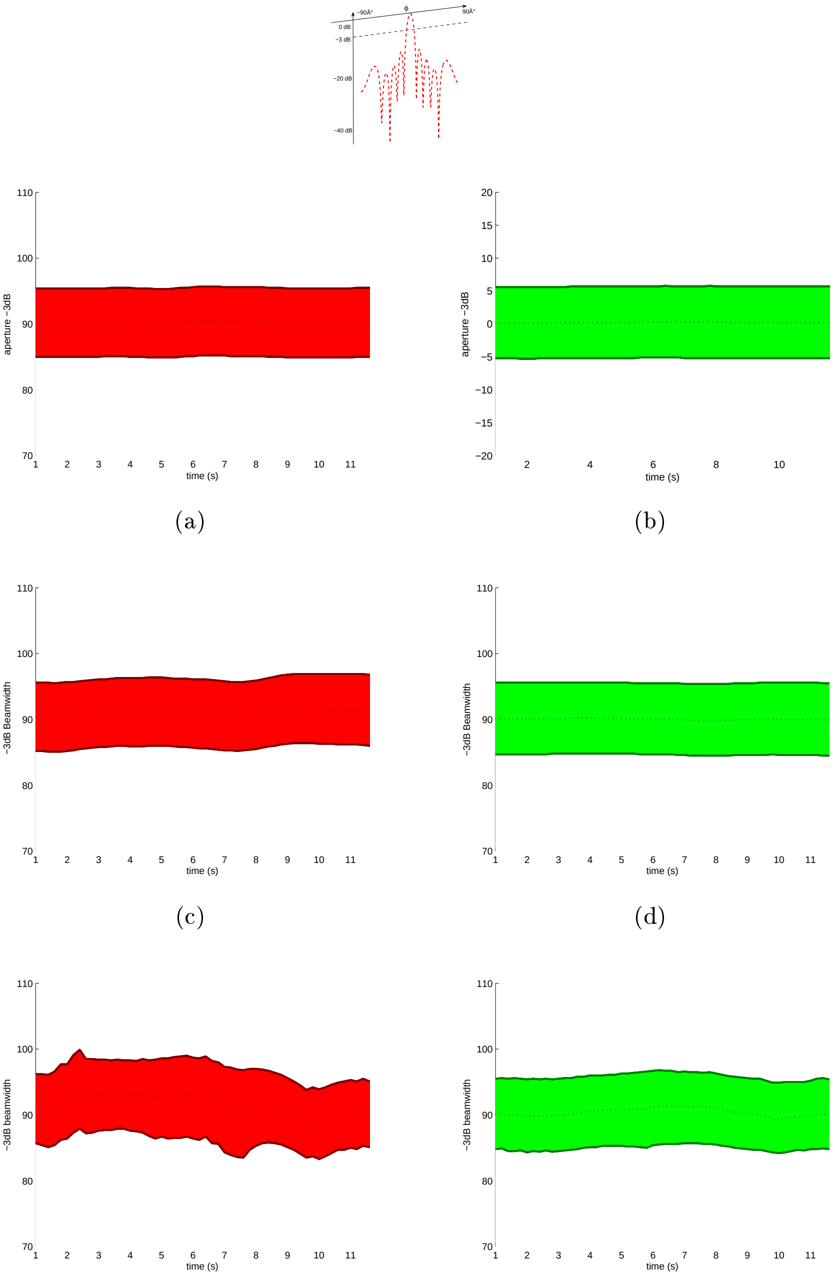

(a) (b)

(c) (d)

(e) (f)

Figure 3.16: Representation of the radiation pattern part above the threshold of -3 dB (direction of the main beam and -3 dB beamwidth): without correction (a) (c) (e) and with correction (b) (d) (f) for sea state 1: (a) and (b), sea state 3: (c) and (d), sea state 6: (e) and (f)

the result without correction (up to 12° with a main direction equals to ±5°) whatever

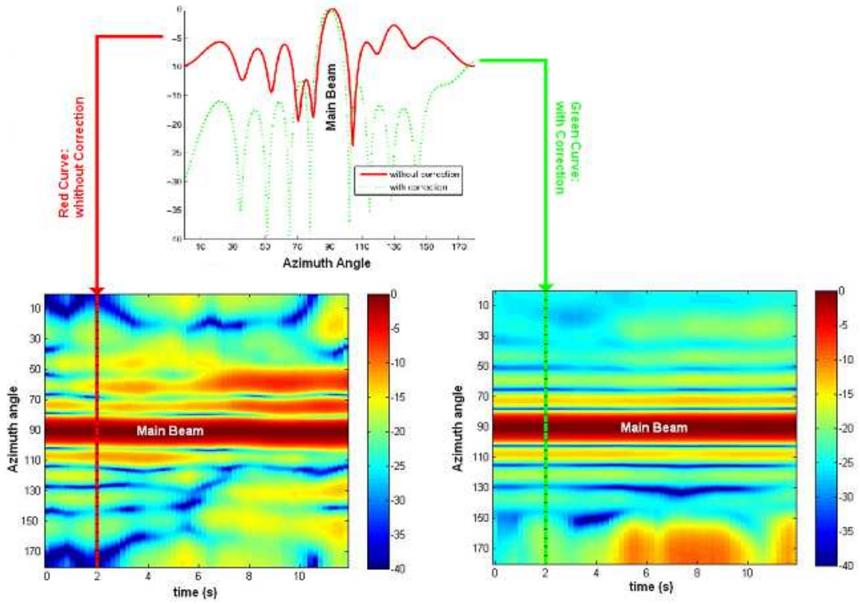

Figure 3.17: An explanation of graph 3.15

the sea state (up to 6).

For the considered array, $\phi_{N-1} = 143°$ we can notice that the correction reduces the sidelobe level for $\phi \leq \phi_{N-1}$.

For ϕ larger than ϕ_{N-1}, the correction is not valid anymore. As an illustration, Fig. 3.18 gives a cut of the result obtained with the radiation pattern in Fig. 3.15 (c) and 3.15 (d) for $t = 2$ s and a sea state equal to 3. In $[0, \phi_{N-1}[$, with correction, the maximum SLL is equal to -12.59 dB, instead of -13 dB for the undeformed array and -9 dB for $[\phi_{N-1}, 180°]$. However, the correction method proposes a better result than the case without correction where the SLL are equal to -2.5dB for $[\phi_{N-1}, 180°]$.

The magnitudes of $\tilde{i}_n$, corresponding to the results in Fig. 3.15 are given in Fig. 3.19. The magnitude of the weights increases with the level of sea state. The maximum value is lower than ten. The weights values are thus realistic and they are implemental in a real process. It means that the approach could be implemented in real life arrays.

We have seen that, the vertical correction method directly computes the prefect set of weights, considering the coupling effect. So, it is a direct method which proposes the best solution. It is not the case considering the horizontal correction method. An investigation of its robustness is necessary for its validation.

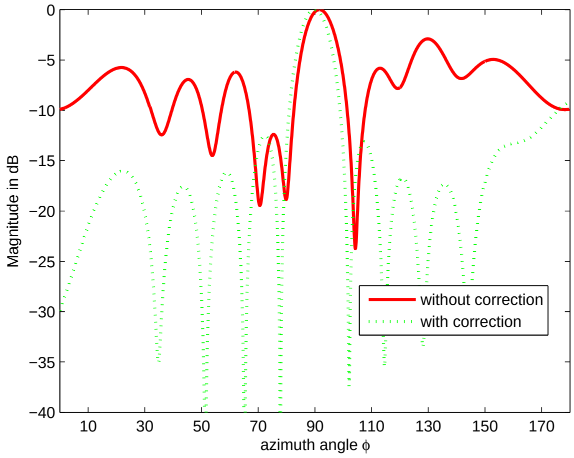

Figure 3.18: Array factor in Fig. 3.15 (c) (without correction) and in Fig. 3.15 (d) (with correction) for $t = 2$ s and sea state value equal to 3

3.4.4 Quantitative analysis of the performance of the horizontal correction

We now propose a more systematic assessment of the correction method. In this section, the investigation is limited to the horizontal correction. Each antenna position is defined using horizontal deformations around its initial position (x_n, y_n):

$$\begin{aligned} \tilde{x}_n &= x_n + \Delta x_n \\ \tilde{y}_n &= y_n + \Delta y_n \end{aligned} \tag{3.20}$$

where Δx_n and Δy_n, the horizontal deformations from the initial position. They are represented by a normal distribution with a variance σ^2.

When σ^2 increases, the deformation of the receiving array increases. The values of σ^2 are chosen to be consistent with deformations studied in Chapter 2.

For each level of deformation (or σ^2), 100 random perturbations were averaged. For each draw, the maximum sidelobe level (SLL) is computed. Fig. 3.4.4 corresponds to a uniform 10-antenna array (the initial weights I without correction are uniform and equal to one) with and without correction. The maximum SLL which is noticed in the interval where the horizontal correction method is effective, that is $[0, \phi_{N-1}]$. For a 10-element array, the interval is $[0, 143°]$.

Observing Fig. 3.4.4, we can see that the correction is robust up to $\sigma^2 = 0.1\lambda^2$ as the maximum SLL is lower than -10 dB.

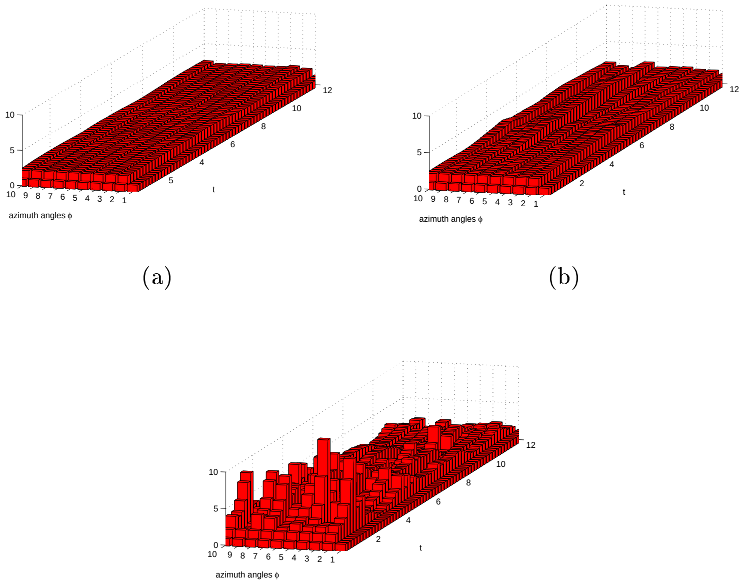

(a) (b) (c)

Figure 3.19: Values of weights to apply correction methods: (a) sea state 1 (b) sea state 3 (c) sea state 6

We have seen that the correction procedure is not efficient for ϕ larger than ϕ_{N-1}. One possible solution would be to increase N so that ϕ_{N-1} gets larger.

Fig 3.21 represents the value of ϕ_{N-1} depending on the number of antennas in the array. The oscillations correspond to the parity of N (with an even number N, ϕ_{N-1} is larger than with an odd number). We can see that with a uniform 100-antenna array $\phi_{N-1} = \phi_{99} = 169°$. It means that the correction method can be realized on almost all the front radiation pattern.

The performance of the correction for such a receiving array is presented in Fig. 3.22.

Thus, the horizontal correction method can be applied in a larger interval $[0, 169°]$. Increasing the number of antennas in the array, the maximum SLL which is obtained is globally lower (around -13 dB for all σ^2 values).

Even if such an array is larger than existing arrays radar array, it is possible to have this array in the highest frequencies of the HF band. For example, at 12 MHz, the corresponding λ is equal to 10 m. It means that the length of the array is equal to 500 m with $\lambda/2$ interspacing.

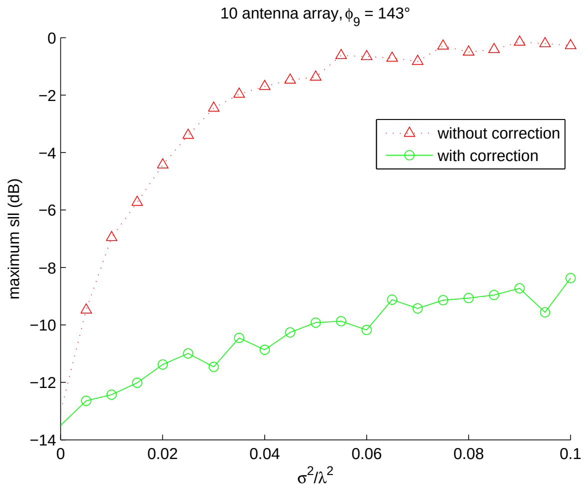

Figure 3.20: Robustness of the correction method of a 10-antenna array

Another way to improve the horizontal correction method is to consider other initial weights. Until now, the method was presented with uniform weights: $\mathbf{I} = [\ 1\ 1\ \ldots\ 1\ ]^T$. Tchebychev weights permit to compute radiation pattern with a uniform SLL (cf Chapter 1).

As an illustration, Fig. 3.23 presents the performance of a 100-element array with Chebychev weights for -40 dB.

Although the correction procedure does not succeed in maintaining such a SLL, it results in a radiation pattern where the maximum SLL is under -20 dB.

3.4.5 Robustness of the horizontal correction method

This section is focused on the robustness of the horizontal correction method. Until now, when a correction method is used, the positions of buoys are supposed to be perfectly known. We now assess the effect of positioning errors. This aspect is very important because the efficiency of the method depends on the accuracy of the positioning system which is used.

In practice, the antennas positions on the buoys are supposed to be measured with a Global Positioning System (GPS).

First, we have to give a new definition of the antennas positions, introducing the positioning errors:

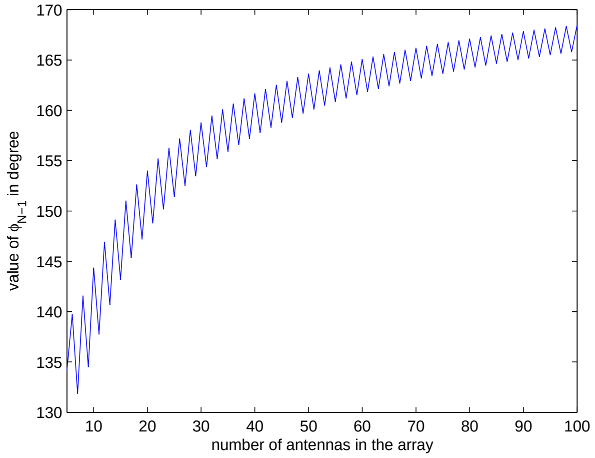

Figure 3.21: value of ϕ_{N-1} according to the number of antennas in the receiving array

$$\begin{aligned} \tilde{x}'_n &= \tilde{x}_n + \Delta\tilde{x}_n \\ \tilde{y}'_n &= \tilde{y}_n + \Delta\tilde{y}_n \end{aligned} \tag{3.21}$$

where $\Delta\tilde{x}_n$ and $\Delta\tilde{y}_n$ are the positioning errors, $(\tilde{x}_n, \tilde{y}_n)$ are the exact horizontal coordinates of antenna n (in the considered example $\sigma^2 = 0.05\lambda^2$) and $(\tilde{x}'_n, \tilde{y}'_n)$ are the measured coordinates of antenna n with a GPS. $\Delta\tilde{x}_n$ and $\Delta\tilde{y}_n$ are defined using a normal distribution with a variance σ_e^2.

frequency	5 MHz	7.5 MHz	15 MHz	30 MHz
$\lambda(m)$	60	40	20	10
$\lambda/10(m)$	6	4	2	1

Table 3.1: Precision in meter in HF band

The studied array is a uniform 100-antenna array. All the results concerning the positioning errors are represented in Fig. 3.24. As we have seen in the previous section, for all the points of the curve (or for each value of the variance σ_e^2), 100 draws have been realized and for each draw the maximum has been computed. The curve represents the mean of the maximum SLL of all these draws in dB. The correction is applied assuming the antennas have the measured positions while the radiation pattern is computed using the exact positions.

We can see that if the positioning errors are large, the effects of the correction method are limited. Typically, the maximum admissible variance is $\sigma_e^2 = 0.01\lambda^2$ (with

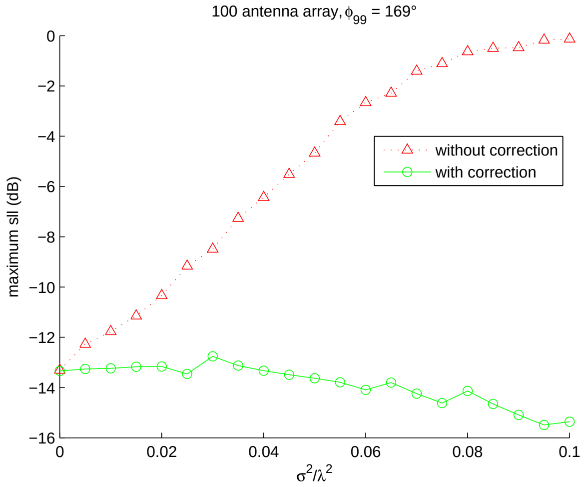

Figure 3.22: Robustness of the correction method of a 100-antenna array

a standard deviation $\sigma_e = 0.1\lambda$) which corresponds to a -10 dB SLL.

Table 3.1 is a representation of the maximum positioning error following the working frequency, considering $\sigma_e = 0.1\lambda$. We can quantify the equivalent maximum positioning error ($\Delta\tilde{x}_n$ and $\Delta\tilde{y}_n$) in meter following the working frequency. For example, it is 1 meter for $f = 30$ MHz.

3.5 Comparison with iterative methods

Our method has proved to be fast and quite efficient. It is therefore interesting to compare it to standard well known correction methods based on iterative algorithms. To this end, two global methods are studied, the Genetic Algorithm (GA) and the Particle Swarm Optimization (PSO).

The litterature is full of detailed presentations of GA and PSO algorithms, for instance see [19] [18]. We will thus restrict our presentation to the modifications we have made to adapt these algorithms to our problem. We now show how GA and PSO can be used to provide a new way of correcting the excitation weights in our deformed arrays. The goal is to improve the radiation patterns (compared to the ones we obtained with the proposed correction methods in the previous sections) and especially to reduce the SLL.

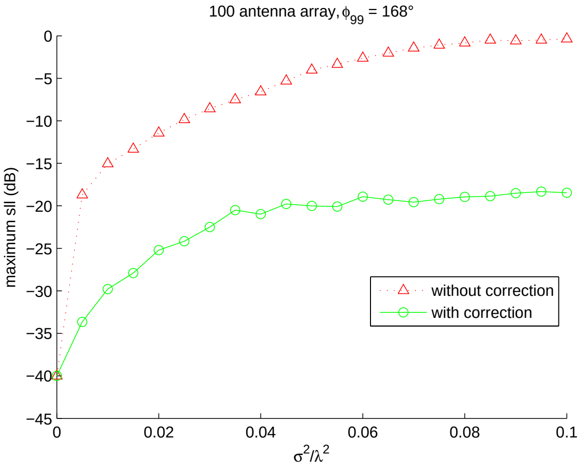

Figure 3.23: Robustness of the correction method of a 100-antenna array with Tchebychev weights of -40 dB

3.5.1 Genetic algorithm method

3.5.1.1 GA modifications

The idea is the same as for as our correction method: we optimize the positions of the zeros so that the SLL is reduced to a certain value. The fitness function is thus the maximum of the SLL and a chromosome is a set of the roots of the associated polynomial of the deformed array. There are N-1 roots for N weights. In addition, it is also needed to optimize for the width of the main lobe. This width of the main lobe is defined by two roots. By fixing these two roots, we then optimize only the other N-3 roots.

At each iteration, we keep the first half of the chromosomes which are ranked by SLL. The second half is recreated by swapping the first half at a random point. Finally, one random mutation of one bit is introduced. The number of chromosomes in the initial population is equal to the length of one chromosome.

The problem is then to code the roots: each root n is a complex number $r_n = a_n + jb_n$. We have found that defining a_n and $b_n \in [-10; 10]$ with a resolution of 0.01 gives the best results. So, the number of possible solutions for a_n and b_n is equal to 2001. Thus, a_n and b_n can be encoded with 11 bits and each root is encoded with $L_{gene} = 22$ bits.

As time goes on, the sea surface changes, the buoys move and thus a new set of weights has to be computed. However, the new sea surface is not very different from the previous one. Therefore, in order to speed up the computation, one of the chromosome is initialized with the previous set of weights (except for the first time). This is illustrated in Fig. 3.25.

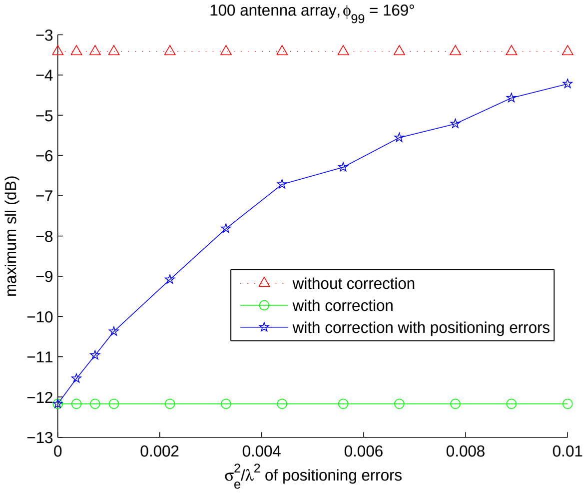

Figure 3.24: Influence of positioning errors

3.5.1.2 GA results

The algorithm is tested for three different sea states with $N_t = 60$ time values with a 0.2 s time step for each sea state. The fitness function is a SLL less than -13 dB. We consider the same 10-element array, so each chromosome is encoded with $L_{chrom} = 154$ bits. The GA results are illustrated in Fig. 3.26, 3.27 and 3.28 for sea states 1, 3 and 6 respectively. The sea surfaces used are the same that were used to test our method in order to properly compare the various methods.

The left part (cf. Fig. 3.26 (a) for instance) corresponds to the radiation pattern evolving with time. The same representation has been used for our method in Fig. 3.15. The bottom right part (cf. Fig. 3.26 (b) for instance) is a cut at -3 dB of the radiation pattern of the left part. This is to be compared to Fig. 3.16 that shows the results for our method.

The number of iterations is associated to the number of radiation pattern (RP). It means that the top right part (cf. Fig. 3.26 (b)) is the number of radiation patterns which were necessary to find a solution. Two kinds of results can be considered. If the algorithm is successful (radiation pattern with a SLL $<$ -13 dB), the number of iterations is indicated with a triangle. If it is not the case, the algorithm was terminated exceeding the number of iterations N_{last} and this kind of result is represented with a circle. So, the given solution corresponds to the best solution we have obtained and the number of radiation pattern we have needed to find it.

When the sea state increases, the deformation in the receiving array is larger and so is the computational cost. Globally, the GA correction method proposes better results than our correction method. The SLL are globally lower particularly when the array has strong deformations (around -13 dB for a sea state 1 and 3, around -10 dB for a sea state 6).

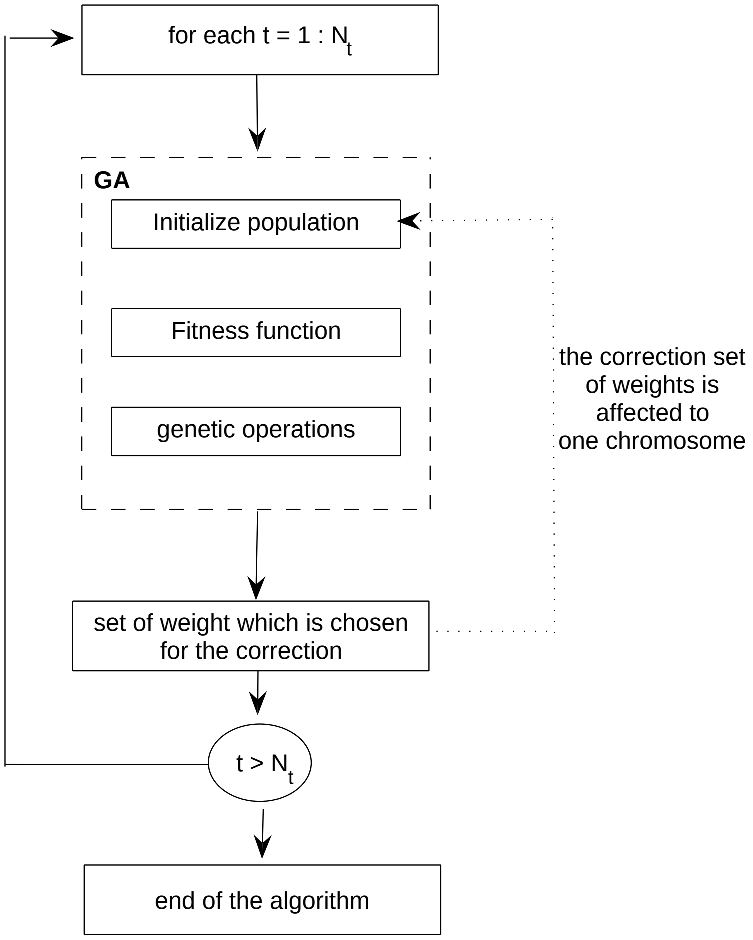

Figure 3.25: Flow chart of the GA applied for the simulation.

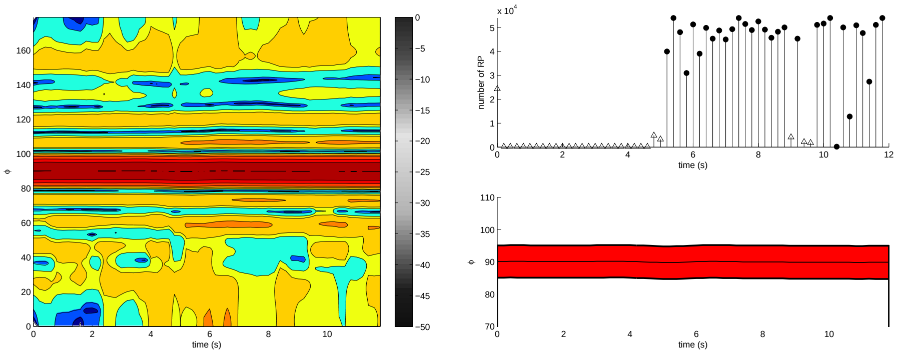

(a) (b)

Figure 3.26: GA correction ($N_{gene} = 15$, $N_{chrom} = 128$) with a sea state 1

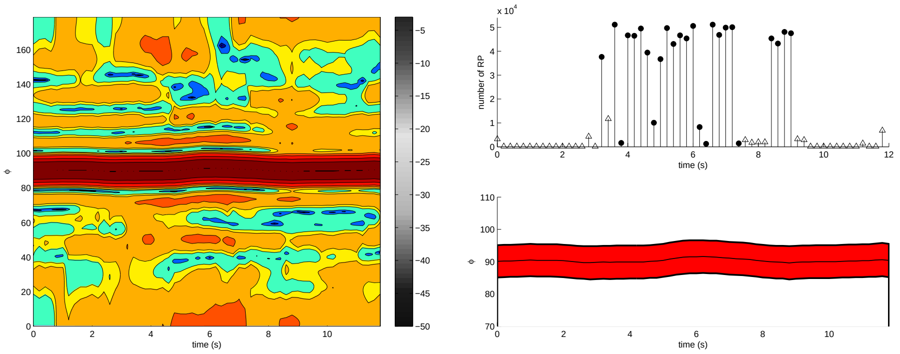

(a) (b)

Figure 3.27: GA correction ($N_{gene} = 15$, $N_{chrom} = 128$) with a sea state 3

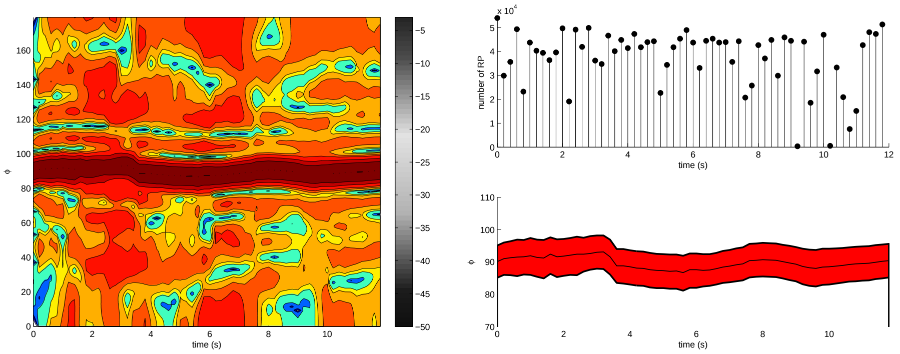

(a) (b)

Figure 3.28: GA correction ($N_{gene} = 15$, $N_{chrom} = 128$) with a sea state 6

If the deformations of the array are weak, the number of radiation patterns computed to have a good solution is limited (for example cf. Fig. 3.26(a), from 0 s to 4.6 s). Actually, the first time step requires 25000 radiation patterns, and then, thanks to the slow modifications of the sea surface and the proper initialization of the population, only a few steps are needed. But for strong deformations, the number of radiation pattern can be very large (for example cf Fig. 3.26(a), from 5.2 s to 8.8 s).

Furthermore, the method does not always propose a good solution. For example, with a sea state 6, the beam changes its main direction of a few degrees. A condition is thus necessary to conserve this direction, the fitness function has to be improved accordingly. But whatever the result, the GA is so long to run that it is not suitable for a real time application. The reason is the binary encoding of the positions of the roots which leads to large chromosomes. The next section will thus consider another kind of iterative algorithm, the PSO.

3.5.2 Particle Swarm Optimization method

Contrary to the GA correction methods, the roots of the associated polynomial are not taken into account. This choice of population for GA was realized considering the large computational cost. It is not the case for PSO which is more acceptable.

3.5.2.1 PSO fitness function and evaluation of population

Two PSO correction methods are presented, proposing two different fitness functions. The first one has a fitness function which corresponds to the maximum SLL in the radiation pattern. As for the GA method, the PSO is terminated if the fitness value of one agent is inferior to -13 dB or if the number of iteration L_{last} is superior to 300.

The second one considers a new fitness function which takes into account the width and the azimuth position of the main beam, in addition to the maximum SLL.

$$F = F1 + 10 \times F2 + 10 \times F3 \tag{3.22}$$

where $F1$ is the maximum SLL in dB, $F2$ is the width of the main beam in degree and $F3$ is the relative position of the main beam in degree, considering that its initial position is in $90°$.

3.5.2.2 Results of PSO correction methods

The same sea surfaces as in the GA section are used, along with the same way of presenting the results.

The results of PSO correction method 1 are illustrated in Fig. 3.30, Fig. 3.31 and Fig. 3.32 for sea state 1, 3 and 6 respectively and the results of PSO correction method 2 are illustrated in Fig. 3.33, Fig. 3.34 and Fig. 3.35 for sea state 1, 3 and 6 respectively.

As we have seen with the GA correction method, when the sea state increases, the deformations in the receiving array are larger and the computational cost increases.

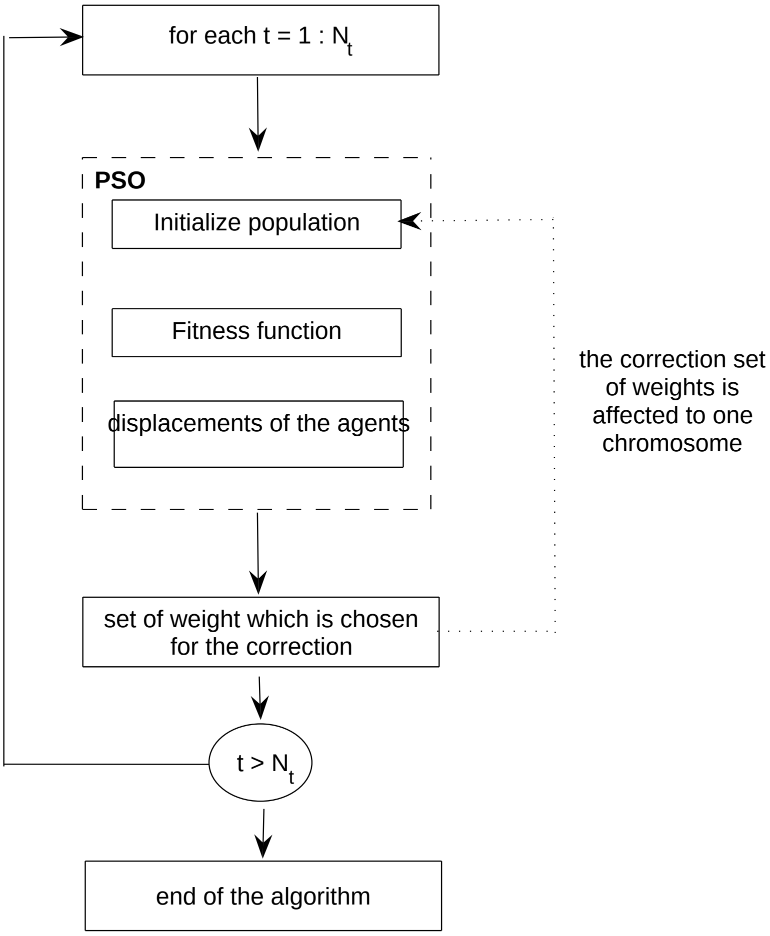

Figure 3.29: PSO applied for the simulation.

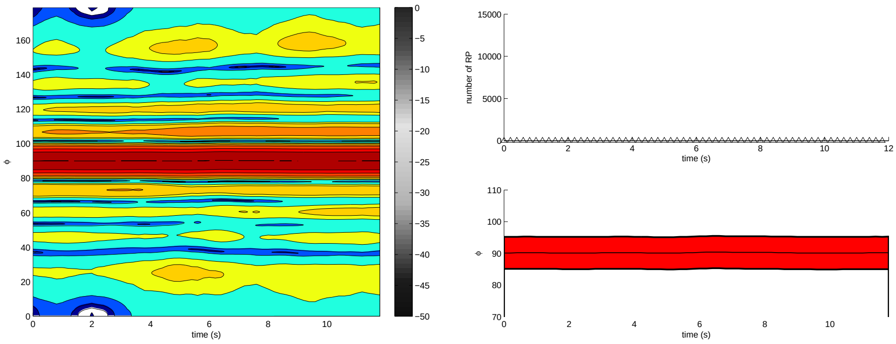

(a) (b)

Figure 3.30: PSO correction method 1, sea state 1

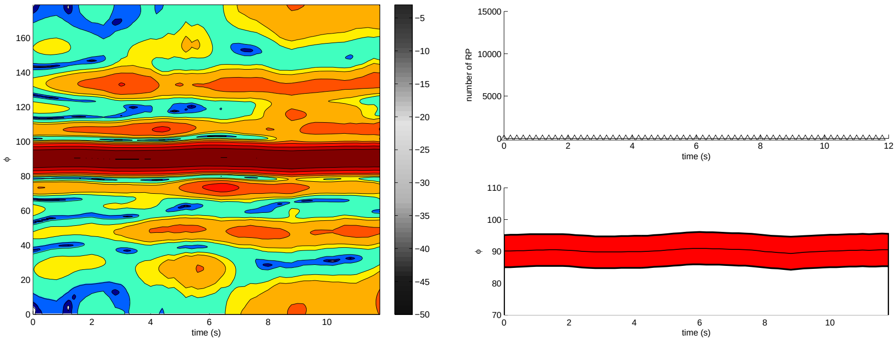

(a) (b)

Figure 3.31: PSO correction method 1, sea state 3

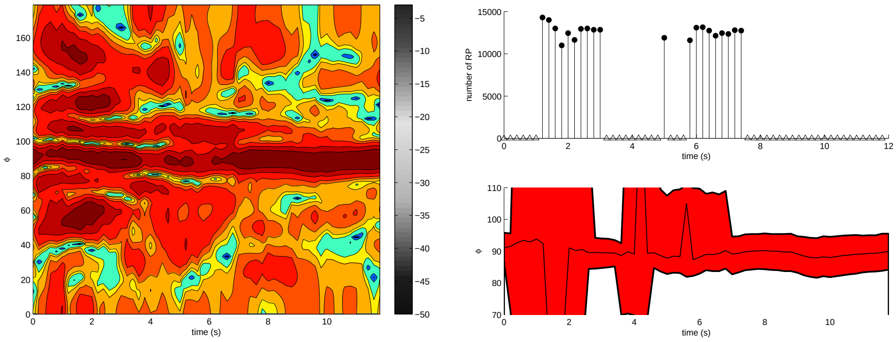

(a) (b)

Figure 3.32: PSO correction method 1, sea state 6

Furthermore, the algorithm does not propose systematically a good solution. Besides, the PSO correction methods are faster than the GA correction method.

The results of the PSO correction method 1 has a good results except for a sea state of 6 where there is no main beam anymore at 4 s and 6 s.

The results of the PSO correction method 2 are better than PSO correction method 1, the improvement of the fitness function permits to have a width and a position of the main beam which is unchanged from the main beam of the undeformed array even if sometimes the proposed solution cannot be validated giving a radiation pattern with a large main beam (for example see Fig. 3.35 between 5 and 7 s).

Moreover, the PSO correction method 2 is globally as fast as the PSO method 1. Sometimes method 2 is a little bit slower, the new fitness function generating sometimes a computational cost more important (for example cf Fig. 3.34 at 10.8 s). Sometimes it is faster (for example cf. Fig. 3.35 at 2 s) the fitness function helping for the choice of a good solution.

3.5.2.3 Conclusion of PSO methods

PSO correction methods propose faster solutions than the solutions given by the GA correction method. PSO correction method 2 is a good compromise between the computational time and the obtained result. The conditions which are imposed in the fitness function permit to converge quickly toward a good solution. If we compare this method with the correction method developed in chapter 4, the PSO method proposes a better solution than the correction method but the computational cost is more important.

3.6 Conclusion of Chapter 3

A method has been presented that permits to correct the horizontal and vertical displacements of antenna elements in a deformed array. The vertical correction relies on the knowledge of the modification of the coupling matrix. The horizontal correction can be synthesized by forcing the nulls in the radiation pattern of a deformed array. The goal is to obtain the same zeros as in the initial undeformed array. Both techniques result in the decrease of the SLL that have appeared as a result of the array deformation, while keeping a correct main beam.

A comparison with iterative algorithms has shown that our method is a little bit outperformed in terms of SLL, but leads to a drastic reduction of the computation time. Our method paves the way for real time compensation in moving arrays such as HFSWR on floating buoys.

The robustness of the horizontal correction method has also been analyzed. It has permitted to see that it relies on a good knowledge of antennas positions. A method to have a better knowledge of antennas positions is proposed in Chapter 4.

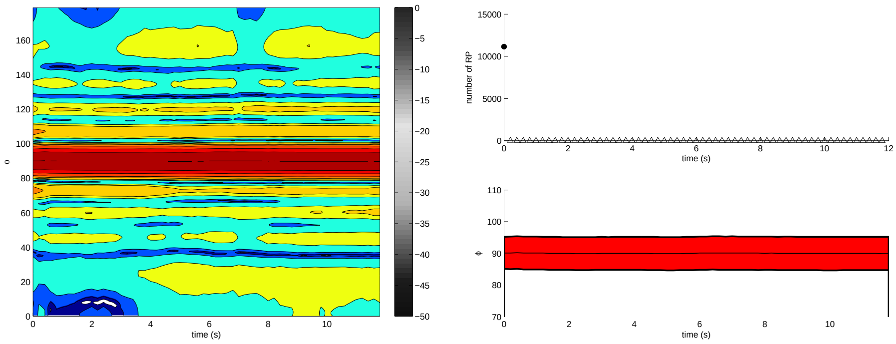

(a) (b)

Figure 3.33: PSO correction method 2, sea state 1

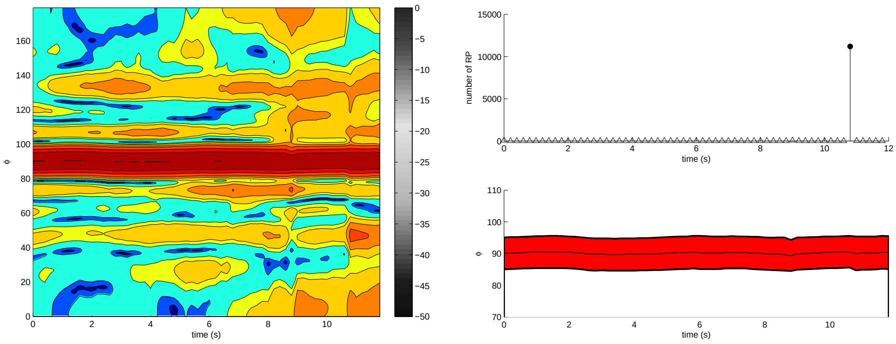

(a) (b)

Figure 3.34: PSO correction method 2, sea state 3

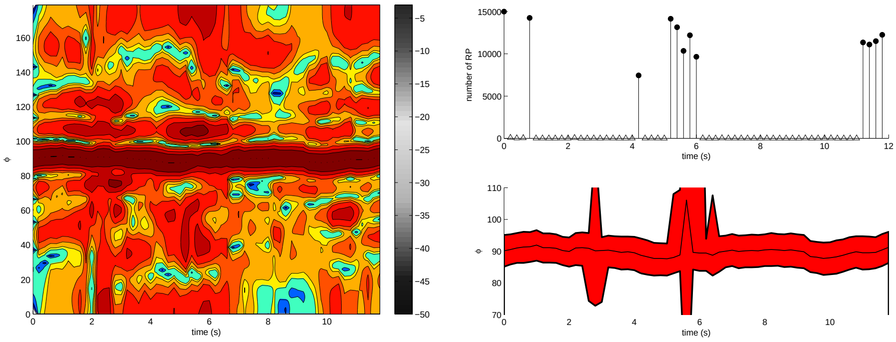

(a) (b)

Figure 3.35: PSO correction method 2, sea state 6

Chapter 4

Direction of Arrival

4.1 Introduction

Through specific post-processing of signals impinging on the antenna array it is possible to obtain information about target direction of arrival. Several algorithms have been developed in that purpose over the last thirty years. The most popular is certainly the MUSIC algorithm [31], standing for MUltiple SIgnal Classification. This method allows to retrieve the directions of arrival of targets, by extracting properties of the correlation matrix of received signals in the receiving array. The MUSIC algorithm has been developed under the hypothesis that the position of each antenna in the receiving array is perfectly known.

For our peculiar problem it is interesting to evaluate how robustness behaves when antenna positions are not exactly known, but defined with some positioning errors. This situation is precisely the one of a receiving array whose each antenna is placed on a buoy on sea surface and is equipped with a GPS receiver (the positioning errors of each antenna is equal to the error corresponding to the accuracy of the location given by a GPS system).

This chapter provides a detailed presentation of the MUSIC algorithm and focuses on the Weiss Friedlander method which is an evolution of MUSIC for improving performances for deformed arrays. A set of simulations has been done in order to evaluate positioning errors of the antennas in the moving receiving array. Finally, we conclude about the efficiency of these kind of algorithms in the practical cases of our study.

4.2 Mathematical formulation of the problem

We consider a N antennas receiving array and D incident monochromatic waves. D corresponds to the number of targets to be detected. A received signal is associated with each antenna. It is stacked in the following $1 \times N$ vector

$$\mathbf{S} = [S_1, \ldots, S_N]^T \tag{4.1}$$

Each received signal S_i is defined either from a single measure or from the averaging of a large number of measured samples.

Each incident wave is associated with a complex quantity F_j. The phase reference point has been arbitrarily chosen as being the position of the first antenna placed conventionally at origin. All these quantities can be combined into the following $1 \times D$ vector $\mathbf{F} = [F_1, \ldots, F_D]^T$.

It noted that D, the dimension of $\mathbf{F}$, is not a priori known.

Similarly, each noise component on each receiver W_i is stacked in the following $1 \times N$ vector $\mathbf{W} = [W_1, \ldots, W_N]^T$.

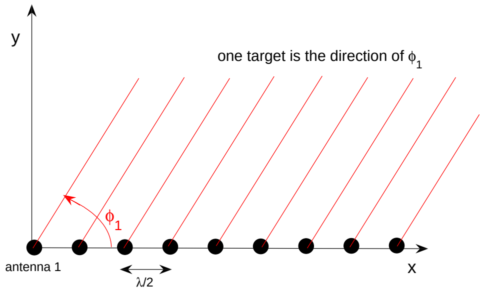

Figure 4.1: Direction of the incident wave generated by a target

We assume that the measured vector $\mathbf{S}$ can be written as a linear combination of D incident waves plus noise. It is related to the incident vector $\mathbf{F}$ as:

$$\mathbf{S} = \mathbf{AF} + \mathbf{W} \tag{4.2}$$

Where $\mathbf{A}$ is the complex $(N \times D)$ rectangular matrix associated with the receiving array.

$$\mathbf{A} = [\mathbf{a}_1, \ldots, \mathbf{a}_D] \tag{4.3}$$

This matrix is made of D columns vectors $\mathbf{a_j}$ defined as:

$$\mathbf{a_j} = [\ a_{1j}, \ldots,\ a_{Nj}\ ]^T \tag{4.4}$$

Each column vector $\mathbf{a_j}$ is called a modal vector and is depending on the response of the system for a given set of variables. The component a_{ij} of the modal vector is depending on:

- the position $\mathbf{r_i}$ of receiver i, the radiation pattern (directivity, gain, etc...).
- the incident angle ϕ_p of incident wave p, its frequency, its polarization as well as the position $\mathbf{r_p}$ of the target (if it is not localized at infinity)

In the following sections, the number of variables will be considered constant in the process of the calibration of the system: we will calibrate the modal vectors as being the functions of both given incident angle ϕ and locations of the antennas (stacked in the vector $\mathbf{r}$). We call them $\mathbf{a_j}(\phi)$. All the other parameters are implicitly known: frequency of the wave, polarization, etc...

Thus, the knowledge of the modal vectors of the matrix $\mathbf{A}$ is equivalent to the knowledge of all the parameters of the problem, including the direction of arrivals.

The antenna n response (in the case of an assumed uniformed and linear receiving array) from the p source coming from ϕ_p direction is defined as:

$$a_n(\phi_p, x_n, y_n) = \exp\left(j\frac{2\pi}{\lambda}\left(x_n \cos\phi_p + y_n \sin\phi_p\right)\right) \tag{4.5}$$

where x_n is the coordinate of antenna n in the array and λ is the wavelength of the received signal.

In Eq. 4.5 the locations of the antennas are perfectly known. To take into account a given uncertainty on the position of antennas, we add the error terms Δx_n and Δy_n to the initial position of the receiving array (x_n, y_n):

$$a_n(\phi_p, x_n, y_n) = \exp\left(j\frac{2\pi}{\lambda}\left((x_n + \Delta x_n)\cos\phi_p + (y_n + \Delta y_n)\sin\phi_p\right)\right) \tag{4.6}$$

The MUSIC algorithm which is described in the following section has not been set up for a situation with an error term on the antennas position.

The blind determination of the modal vectors will be affected by these errors terms. It will be considered as a new unknown parameter which can be added with the others existing parameters. The Weiss Friedlander algorithm has been introduced to deal with this kind of situation, [31] and [40]. This approach which permits to jointly estimate the errors of the positions of the antennas and the real directions of the arrivals of the targets will be evaluated in the last sections of the chapter.

4.3 Presentation of MUSIC Algorithm

In this section the MUSIC algorithm is presented. This algorithm allow to determine the direction of arrivals for one or few targets from the receiving array.

The receiving array can have a specific geometry, like a linear or a circular geometry. However, the study will be done in the case of an uniform linear array on which we apply a random deformations.

So, in the first part of the study, the receiving array is uniform (without positioning errors of the antennas).

The first goal is to determine the modal vectors corresponding to the received signals, from the measures ($\mathbf{S}$ vector).

4.3.1 Preliminary remarks

The vector $\mathbf{S}$ belongs to an N dimensional vector space Ξ. If the problem 4.2 is noise free ($\mathbf{W} = 0$), Eq. 4.2 corresponds to a linear combination of D modal vectors of the matrix $\mathbf{A}$ and so $\mathbf{S}$ is embedded in a subspace vector of Ξ. Lets call G this subspace (subspace Signal of Ξ).

The dimension of subspace G is not necessary equal to D because there may exist some linear dependencies between some modal vectors. In the general case:

$$\dim(G) \leq D \tag{4.7}$$

In fact, the dimension of G is equal to the rank of the matrix $\mathbf{A}$. This is the rank of the matrix $\mathbf{A}$ which determines the number of incident signals. So, to detect D independent signals, the number of antennas N has to be defined as $N \geq D$. In the opposite case (if $N < D$), the system 4.2 indicates that the D modal vectors are necessarily dependant. Thus, the rank of the matrix does not permit to determine the number of targets.

In the case where an additive noise is assumed, the vector $\mathbf{S}$ is not totally included in G, but it has some projection into the noise subspace (eq. 4.1).

The D modal vectors $\mathbf{a_j}$ of the matrix $\mathbf{A}$ correspond to an array of antennas which is illuminated by D individual impinging waves. They belong to a set of all the modal vectors, corresponding to the possible values which can be taken into account by the variables of the problem.

This infinite set is called Ω and it contents an infinite number of vectors. Ω is the complete characteristic of the receiving array in all its possible responses (determined by the geometry, the radiation patterns and the directivity). It can also be called the continuum of vectors $\mathbf{a_j}$.

The fundamental principle of the algorithm MUSIC is to analyse the structure of the received signal covariance matrix.

4.3.2 Measured covariance matrix

We assume that the vector $\mathbf{S}$ is centred (if it is not the case, we can build $\mathbf{S_c} = \mathbf{S} - \mathbf{S_a}$ from $\mathbf{S_a}$ the average of $\mathbf{S}$). The covariance matrix $\mathbf{R}$ is built from the measurement vector $\mathbf{S}$, E stands for the mathematical expectation. The symbol † is the transposed conjugate application:

$$\mathbf{R} = E(\mathbf{S}\mathbf{S}^\dagger) \tag{4.8}$$

It can be shown that all the characteristics concerning the incident signals can be deduced from the covariance matrix $\mathbf{R}$.

$\mathbf{R}$ is a $N \times N$ square matrix. It can be written in more detail as:

$$\mathbf{R} = \begin{pmatrix} E(|S_1|^2) & E(S_1 S_2^\dagger) & \ldots & E(S_1 S_N^\dagger) \\ E(S_2 S_1^\dagger) & E(|S_2|^2) & \ldots & E(S_2 S_N^\dagger) \\ \vdots & \vdots & \ddots & \vdots \\ E(S_N S_1^\dagger) & E(S_N S_2^\dagger) & \ldots & E(|S_N|^2) \end{pmatrix} \tag{4.9}$$

This matrix is Hermitian. The elements which are not on the diagonal of the matrix express possible correlations between the different signals which are measured on each antenna. If we introduce the relation 4.2 in 4.8, we obtain:

$$\mathbf{R} = E((\mathbf{AF} + \mathbf{W})(\mathbf{AF} + \mathbf{W})^\dagger) = E(\mathbf{AFF}^\dagger\mathbf{A}^\dagger + \mathbf{WF}^\dagger\mathbf{A}^\dagger + \mathbf{AFW}^\dagger + \mathbf{WW}^\dagger) \tag{4.10}$$

If we assume that incident signals and noise are independent on each antenna we have:

$$\mathbf{R} = \mathbf{APA}^\dagger + \mathbf{B} \tag{4.11}$$

with:

$$\mathbf{P} = E(\mathbf{FF}^\dagger) = \begin{pmatrix} E(|F_1|^2) & E(F_1 F_2^\dagger) & \ldots & E(F_1 F_D^\dagger) \\ E(F_2 F_1^\dagger) & E(|F_2|^2) & \ldots & E(F_2 F_D^\dagger) \\ \vdots & \vdots & \ddots & \vdots \\ E(F_D F_1^\dagger) & E(F_M F_2^\dagger) & \ldots & E(|F_D|^2) \end{pmatrix} \tag{4.12}$$

and

$$\mathbf{B} = E(\mathbf{W}\mathbf{W}^\dagger) = \begin{pmatrix} E(|W_1|^2) & E(W_1 W_2^\dagger) & \dots & E(W_1 W_N^\dagger) \\ E(W_2 W_1^\dagger) & E(|W_2|^2) & \dots & E(W_2 W_N^\dagger) \\ \vdots & \vdots & \ddots & \vdots \\ E(W_N W_1^\dagger) & E(W_N W_2^\dagger) & \dots & E(|W_N|^2) \end{pmatrix} \tag{4.13}$$

$\mathbf{P}$ is an $(D \times D)$ Hermitian matrix characterizing only the incident signals. Diagonal elements correspond to the energies which are carried on by the D incident waves. The off diagonal elements express the level of correlation between incoming waves.

$\mathbf{B}$ is an $(N \times N)$ matrix, which characterizes the different noises which disturbs the real signals. We assume the following classical simplification:

- The noise is assumed uncorrelated and thus $\mathbf{B}$ is diagonal:

$$\mathbf{B} = \begin{pmatrix} E(|W_1|^2) & 0 & \dots & 0 \\ 0 & E(|W_2|^2) & \dots & 0 \\ \vdots & \vdots & \ddots & \vdots \\ 0 & 0 & \dots & E(|W_N|^2) \end{pmatrix} \tag{4.14}$$

- the antennas are identical and the noise has zero mean. Then, $\mathbf{B} = \sigma_s^2 \mathbf{I_d}$ where $\mathbf{I_d}$ is the identity matrix $(N \times N)$ and σ_s^2 is the variance of the noise on each antenna.

The three matrices $\mathbf{R}$, $\mathbf{P}$, $\mathbf{B}$ have the classical properties of covariance matrices:

- defined semi-positive,
- all the eigenvalues are real, positive or zero,
- for each matrix, it exists an orthogonal basis: directions of eigenvectors are mutually orthogonal and the multiplicity of each eigenvalue is equal to the dimension of the associated eigensubspace.

4.3.3 Determination of the number of incident waves

We assume that the number of antennas is greater than the number of signals we want to detect: $N > D$.
The rank of $\mathbf{P}$ is assumed to be equal to D. As $N > D$, the $(N \times N)$ matrix $\mathbf{A}\mathbf{P}\mathbf{A}^\dagger$ is singular (rank D), thus:

$$\det(\mathbf{A}\mathbf{P}\mathbf{A}^\dagger) = \det(\mathbf{R} - \sigma_s^2 \mathbf{I_d}) = 0 \tag{4.15}$$

Eq. 4.15 implies that σ^2 is one of the eigenvalues of $\mathbf{R}$. Considering that λ_1, λ_2, λ_3, $\dots$, λ_N, the N eigenvalues of $\mathbf{R}$ and the properties of the matrix, these eigenvalues are real, positive or null. We can arbitrarily sort them in descending order:

$$\lambda_1 \geq \lambda_2 \geq \lambda_3 \geq \cdots \geq \lambda_{N-1} \geq \lambda_{min} \geq 0 \tag{4.16}$$

We consider σ_s^2 is associated with the minimum eigenvalue of $\mathbf{R}$. A covariance matrix $\mathbf{R}$ formulation satisfying 4.15 by construction can then be written as:

$$\mathbf{R} = \mathbf{APA}^{\dagger} + \lambda_{min}\mathbf{I_d} \tag{4.17}$$

The N eigenvectors $\mathbf{e}_i$ of the matrix $\mathbf{R}$ verify:

$$\mathbf{Re_i} = \lambda_i \mathbf{I_d e_i} \; i = 1, \ldots, N \tag{4.18}$$

From Eq. 4.17, we can write:

$$(\mathbf{APA}^{\dagger}\mathbf{e_i}) = (\mathbf{R} - \lambda_{min}\mathbf{I_d})\mathbf{e_i} = (\lambda_i - \lambda_{min})\mathbf{I_d e_i} \tag{4.19}$$

This expression is null for all the eigenvectors corresponding to the minimum value:

$$(\mathbf{APA}^{\dagger}\mathbf{e_i}) = 0 \; ; \; \lambda_i = \lambda_{min} \tag{4.20}$$

Thus, the eigenvectors, corresponding to the minimum value λ_{min}, are also eigenvectors of the matrix $\mathbf{APA}^{\dagger}$ for the null eigenvalue and they belong to the kernel of the corresponding application:

$$e_{i,\lambda_i=\lambda_{min}} \in Ker(\mathbf{APA}^{\dagger}) \tag{4.21}$$

The size of this subspace is equal to the multiplicity β of the corresponding eigenvalue λ_{min}. It is also equal to $N-r$, where $r = rank(\mathbf{APA}^{\dagger})$ and $r \leq D$ (in the general case).

Since it was assumed that all the column vectors of the matrix $\mathbf{A}$ were linearly independent, it follows that $rank(\mathbf{APA}^{\dagger}) = rank(\mathbf{P}) = r$. It means also that $Ker(\mathbf{APA}^{\dagger}) = Ker(\mathbf{PA}^{\dagger})$. Therefore:

$$rank(\mathbf{P}) = N - \beta \tag{4.22}$$

The N values given by 4.16 can be classified as follows:

$$\lambda_1 \geq \lambda_2 \geq \lambda_3 \geq \cdots \geq \lambda_r \geq \lambda_{r+1} = \lambda_{r+2} = \cdots = \lambda_N = \lambda_{min} \tag{4.23}$$

Two essential cases can be explained:

First Case The matrix $\mathbf{P}$ has the maximum rank ($r = rank(\mathbf{P}) = D$). This is the case when the algorithm MUSIC is fully operational. The D columns vectors of the matrix $\mathbf{P}$ are here linearly independent, i.e. that the D incident signals are not correlated, or are not fully correlated. The relation 4.23 can be written as:

$$N - \beta = D \tag{4.24}$$

Moreover, always in this first case, the condition of the rank of $\mathbf{P}$ implies that:

$$Ker(\mathbf{PA}^{\dagger}) = Ker(\mathbf{A}^{\dagger}) \tag{4.25}$$

Thus, the eigenvectors associated with λ_{min}, verifying the relation 4.20, equally verifies:

$$\mathbf{A}^{\dagger}\mathbf{e_i} = 0 \tag{4.26}$$

Associated with the minimum eigenvalue λ_{min}, the eigenvectors are orthogonal to the D modal vectors of the matrix $\mathbf{A}$, therefore they are orthogonal to G. The subspace (with β dimension), which is generated by these eigenvectors, is the Noise subspace previously introduced. The others eigenvectors, which are associated to the eigenvalues which has a higher level, belong to the Signal subspace (which has a dimension equal to $D = rank(\mathbf{P})$). The two subspaces Signal and Noise are orthogonal.

Second Case The matrix $\mathbf{P}$ has not a maximum rank ($r = rank(\mathbf{P}) < D$). $\mathbf{P}$ is singular here and some incident signals are correlated between them. The algorithm MUSIC encounters its fundamental limit and, in general, it cannot determine the parameters of the incident signals. The matrix $\mathbf{P}$ is singular, and the relation 4.27 is not accurate. It can be written as:

$$Ker(\mathbf{A}^{\dagger}) \subset Ker(\mathbf{PA}^{\dagger}) \tag{4.27}$$

Thus, the eigenvectors which are associated to λ_{min} and checking 4.20 (therefore belonging to $Ker(\mathbf{PA}^{\dagger})$), are not necessary included in $Ker(\mathbf{A}^{\dagger})$, and they are not orthogonal to the subspace Signal. The algorithm MUSIC searches the signals which are characterized by vectors whose the orthogonal projections on the subspace Noise is null: this algorithm can not be operational. In this second case the relationship 4.24 becomes:

$$N - \beta < D \tag{4.28}$$

The number of detected signals is less than the number of incident signals really present (it gets a lower limit for the number of signals).

To explain the algorithm, we now assume that we are in the first case which is described above: the number of signals is known and we search now their characteristics, including the direction of arrival.

4.3.4 Direction of Arrivals: calculation of MUSIC Spectrum

The signals are assumed uncorrelated, thus the minimum eigenvalues of $\mathbf{R}$ is $\beta = N - D$:

$$\lambda_{min} = \lambda_{D+1} = \cdots = \lambda_N \tag{4.29}$$

$\mathbf{V}_{D+1}$, $\mathbf{V}_{D+2}$, …, $\mathbf{V}_N$ are the β eigenvectors corresponding to the eigenvalue λ_{min}. All of them verify the relation $\mathbf{RV} = \lambda_{min}\mathbf{I_d}\mathbf{V}$. They generate a noise subspace which is orthogonal to G.

We introduce the $(N \times \beta)$ matrix $\mathbf{E_B}$ whose columns are formed by the eigenvectors of the noise space. $\mathbf{Y}$ is any vector in the space Ξ:

$$\mathbf{Y} = [Y_1 \ldots Y_N]^T \tag{4.30}$$

The projection of $\mathbf{Y}$ in the noise subspace is then $\mathbf{E_B}^\dagger$. A vector $\mathbf{Y}$ belong to the signal subspace when its projection is null. The square of the modulus of this projection is $\mathbf{Y}^\dagger\mathbf{E_B}\mathbf{E_B}^\dagger\mathbf{Y}$. We seek a vector orthogonal to noise.

Thus, the MUSIC algorithm looks for the modal vectors in the continuum which maximizes it and belongs to the subspace Signal which is determined by the eigenvectors $\mathbf{V_1}$, $\mathbf{V_2}$, …, $\mathbf{V_D}$ of the matrix $\mathbf{R}$. For example, if a single angular parameter ϕ is sought, we define the spectrum $P_{MUSIC}(\phi)$ as the following expression:

$$P_{MUSIC}(\phi) = \frac{\mathbf{a}^\dagger(\phi)\sigma_s^2\mathbf{I_d}\mathbf{a}(\phi)}{\mathbf{a}^\dagger(\phi)\mathbf{E_B}\mathbf{E_B}^\dagger\mathbf{a}(\phi)} \tag{4.31}$$

with $\mathbf{a}^\dagger(\phi)\sigma^2\mathbf{I_d}\mathbf{a}(\phi)$ which normalizes the expression. If the noise is strictly zero, the values of the spectrum P_{MUSIC} are infinite for all $\mathbf{a}(\theta)$ belonging to the subspace Signal. If there is noise, the subspace Signal is only located with a certain inaccuracy and we called it the estimated subspace Signal $\hat{G}$. Then, the spectrum presents maxima in the vicinity of the points where the vectors of the continuum Ω are almost orthogonal to the subspace Noise. The D values ϕ_i $(i = 1, 2, \ldots, D)$ of the positions of the picks on the graphic of the spectrum correspond to the incident angles of the D signals.

In practice, there is no access to the entire continuum Ω which contains an infinite number of modal vectors. The phase of calibration of the system only allows the receivers to determine a finite number. For example, M vectors $\mathbf{a}(\phi_k)$ $(k = 1, 2, \ldots, M)$. The maxima of the spectrum no longer correspond to the directions of the real incident waves, but among from the M calibrated directions ϕ_k, they correspond to those which are the closest. To get accurate directions of the incident signals, we follow the phase of research of the maxima (approached) of the spectrum by an interpolation phase to obtain the absolute maximum.

In the case of a continuum depending only on two angles in elevation θ and in azimuth ϕ, we define the spectrum by the function of two variables:

$$P_{MUSIC}(\theta, \phi) = \frac{\mathbf{a}^\dagger(\theta, \phi)\sigma_s^2\mathbf{I_d}\mathbf{a}(\theta, \phi)}{\mathbf{a}^\dagger(\theta, \phi)\mathbf{E_B}\mathbf{E_B}^\dagger\mathbf{a}(\theta, \phi)} \tag{4.32}$$

The principle of the calculation with the algorithm MUSIC is here quite similar to the previous case 4.31, except that the maxima are seek for two angular variables θ and

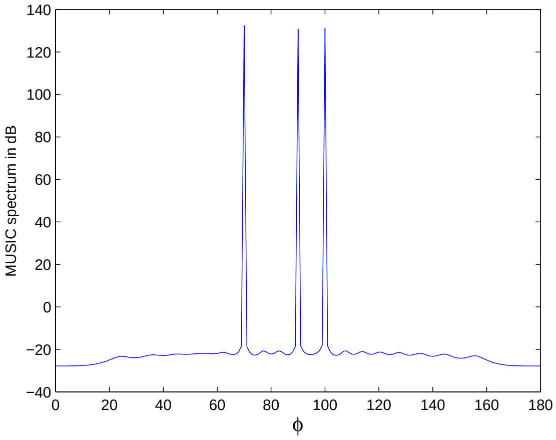

Figure 4.2: MUSIC Spectrum with three target in $\phi = 70°, 90°, 100°$

ϕ.

Fig. 4.3.4 represents an example of MUSIC spectrum in 2D.

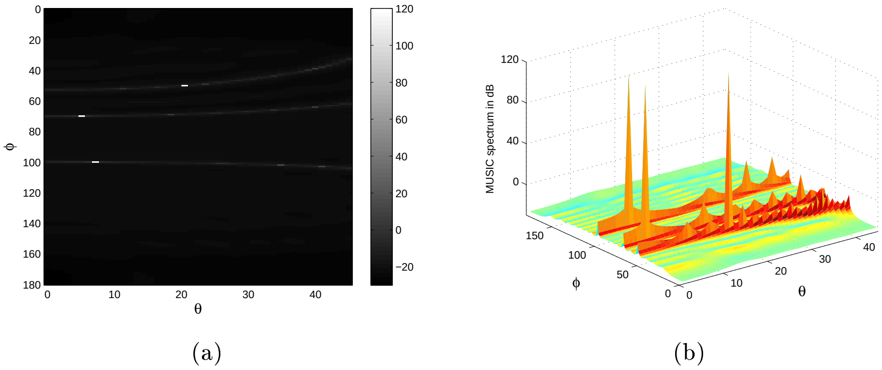

(a) (b)

Figure 4.3: MUSIC Spectrum in 2D with three target in $\phi = 70°, 90°, 100°$ and $\theta = 5°, 7°, 22°$

4.4 Improvement of MUSIC: Weiss Friedlander method

The method of Weiss-Friedlander is based on the MUSIC algorithm. However, it proposes to improve the robustness considering positioning errors of the antennas in the receiving array. It is particularly effective for low amplitudes errors.

This method offers a way to seek the iterative direction of arrivals of the targets and the unknown position of antennas in the receiving array.

4.4.1 Calibration using the optimization of a multidimensional fitness function

The method is based on the multidimensional algorithm MUSIC where we seek the vector of the Direction of Arrivals (DOA) $\hat{\phi} = [\hat{\phi}_1, \hat{\phi}_2, \ldots, \hat{\phi}_D]$ as:

$$\hat{\phi} = arg\min \sum_{p=1}^{D} ||\mathbf{E_B}^{\dagger}\mathbf{a}(\phi_p)||^2 \tag{4.33}$$

where $\mathbf{E_B}$ sizes $(N \times N - D)$ and $\mathbf{E_B}$ is the matrix of the eigenvectors which are associated with the minimum eigenvalue λ_{min}.

This method incorporates antenna position parameters into the model. If we include these parameters in an unknown variable, called ϵ, this method offers a fitness function whose the global minimum is reached for the real values of DOA $\hat{\phi} = [\hat{\phi}_1, \hat{\phi}_2, \ldots, \hat{\phi}_D]$ for the actual values of ϵ. This fitness function is defined as:

$$F(\phi_1, \phi_2, \ldots, \phi_D, \epsilon) = \sum_{p=1}^{D} ||\mathbf{E_B}^{\dagger}\mathbf{a}(\phi_p)||^2 \tag{4.34}$$

Then, the global minimization of this function is transformed in two minimizations carried out alternately, first in the space of the ϕ, then in the space of the ϵ, until the convergence of the algorithm.

So, we want to determine the unknown parameter ϵ. For example, it is represented here by a vector $\mathbf{r}$ comprising all the antennas coordinates. The different steps of the algorithm are:

- Guess value for the parameters of the antenna ϵ is defined: the initial form the receiving array, i.e. the initial position of each antenna (x_n, y_n) (cf Chapter 2), these coordinates are summerized into the vector $\mathbf{r_0}$,
- From this position $\mathbf{r_0}$, a first estimate of DOA $(\phi_{1,0}; \phi_{2,0}; \ldots; \phi_{D,0})$ is computed, minimizing the fitness function according to ϕ,
- Then, minimizing the fitness function for the parameter $\mathbf{r}$, which contains only the coordinates of the antennas, fixing in advance $(\phi_1, \phi_2, \ldots; \phi_D)$ to the previously obtained values $(\phi_{1,0}; \phi_{2,0}; \ldots; \phi_{D,0})$ respectively.
- it remains to do a second time a search for DOA using the new parameters of the receiving array, i.e. using the values of the coordinates of the antennas, until the convergence of the solution.

4.4.2 Linear approximation of the influence of the positions errors of antennas

To solve the third step of the algorithm (minimization of the fitness function to find an estimate of **r**), we could apply the Newton algorithm. However, in practice, **r** is a large size vector. Thus, Weiss and Friedlander method proposes to apply a linear approximation of the influence of errors of the positions on the directional vector. Taking the assumption that the approximate antennas coordinates (including positioning errors) are not too far from the initial coordinates, they proceed to a development in the first order of the elements $a_n(\phi_p, \mathbf{r})$ of the analysis vector (where ϕ_p is now known) in the vicinity of the initial position $\mathbf{r_0}$.

$$\begin{aligned} a_n(\phi_p, \mathbf{r}) &= \exp(j\pi\left[(x_n + \Delta x_n)\cos(\phi_p) + (x_n + \Delta x_n)\sin(\phi_p)\right]) \\ &\approx a_n(\phi_p, \mathbf{r_0})\left[1 + j\pi(\Delta x_n \sin(\phi_p) + \Delta y_n \cos(\phi_p)\right] \end{aligned} \tag{4.35}$$

where x_n and y_n are expressed here in half of wavelengths.

Extending the latter expression to all the elements of a vector $\mathbf{a}(\phi_p, \mathbf{r})$ which is then expressed as the sum of a initial term (x_n,y_n) and a term of disturbances $(\Delta x_m, \Delta y_m)$. Then, giving a matrix form of the obtained expression, we can write the following expression:

$$F(\phi_1, \phi_2, \ldots, \phi_D, r) = \sum_{p=1}^{D} ||\mathbf{z_p} - \mathbf{W_p}\delta_{xy}||^2 \tag{4.36}$$

with

$$\mathbf{W_p} = -j\pi\mathbf{E_B}^{\dagger}\left(diag\left[a(\phi_p, \mathbf{r_0})\cos(\phi_p)\right], diag\left[a(\phi_p, \mathbf{r_0})\sin(\phi_p)\right]\right) \tag{4.37}$$

and

$$\mathbf{z_p} = \mathbf{E_B}^{\dagger} a(\phi_p, \mathbf{r_0}) \tag{4.38}$$

The vector $\mathbf{z_p}$ and the vector $\mathbf{W_p}\boldsymbol{\delta_{xy}}$, which sizes $(N - D)$, represents respectively the nominal term projections and forward disturbance on the subspace noise. The vector $\mathbf{z_p}$ and matrix $\mathbf{W_p}$, which sizes $(N - P \times 2N - 2)$, depend on the estimation of DOA which is realized in the previous step. Finally, only:

$$\delta_{xy} = \left[\Delta x_2, \Delta x_3, \ldots, \Delta x_N, \Delta y_2, \Delta y_3, \ldots, \Delta y_N\right]^T \tag{4.39}$$

depends on the parameters of the antenna.

The real solution that minimizes the fitness function is given by:

$$\delta_{xy} = \left[\Re(\mathbf{W}^{\dagger}\mathbf{W})\right]^{-1} \Re(\mathbf{W}^{\dagger} Z) \tag{4.40}$$

where $\mathbf{W}$ and $\mathbf{Z}$ are defined by the following expressions:

$$\mathbf{W} = \left[\, W_1^T,\ W_2^T\ ,\ldots,\ W_D^T\right]^T \tag{4.41}$$

and

$$\mathbf{Z} = \left[\, Z_1^T,\ Z_2^T\ ,\ldots,\ Z_D^T\right]^T \tag{4.42}$$

4.5 Hypothesis for simulations of direction of arrival

The goal of the simulations is to verify the robustness of the algorithms MUSIC and Weiss Friedlander which are described in the previous sections, including positioning errors on each antennas.

The algorithms of DOA estimation are optimally when the position of each antenna is known. Considering floating antennas concept, as we have introduced in Chapter 2, each antenna would be placed on a buoy and will move with more or less freedom. To know the antenna position, each antenna can be equiped with a tracking system type as GPS (these points are detailed in Chapter 3). Unfortunatly, the knowledge of the position is not perfect and it provides an accuracy of a few meters. The residual error can be represented, for each position x, y and z, with a normal variance σ_e^2.

Moreover, for all the simulations, the following hypotheses are taken:

- A receiving array with a better angular resolution $\delta\phi = 5°$ than the receiving array defined in the previous chapters is defined (cf Chapter 1). So, a $N = 20$ antennas array is used with an identical spacing interelement equal to $\lambda/2$.
- The targets are distant from the receiving array and the signals emitted by the latter are supposed to be plane wave. The amplitudes of the signals are assumed equal and unitary.
- All sources of noise are represented by a Gaussian white noise with a variance σ_s^2 is arbritrary equal to 0.1.
- The number of measurements (for calculation of the correlation matrix) on each antenna is 24.
- For our study, we will assume that the continuum Ω, theoretically infinite, will be sufficiently representative of all the possible solutions of the directions of arrival, to overcome an interpolation. This is why, the continuum is discretized with a step of 0.1° for the simulations. This is quite satisfactory for the analysis of the performance of the algorithms.
- Positioning errors of the antennas will be taken into account on only 2 dimensions: longitudinal and transverse, not in the vertical dimension. We therefore consider

that the targets and the receiving array belong to a single plan. Each antenna is identified in the plan by its coordinates $\tilde{x}_n + \Delta\tilde{x}_n$ and $\tilde{y}_n + \Delta\tilde{y}_n$, with $\Delta\tilde{x}_n$ and $\Delta\tilde{y}_n$ the positoning errors (cf Chapter 2 and 3).

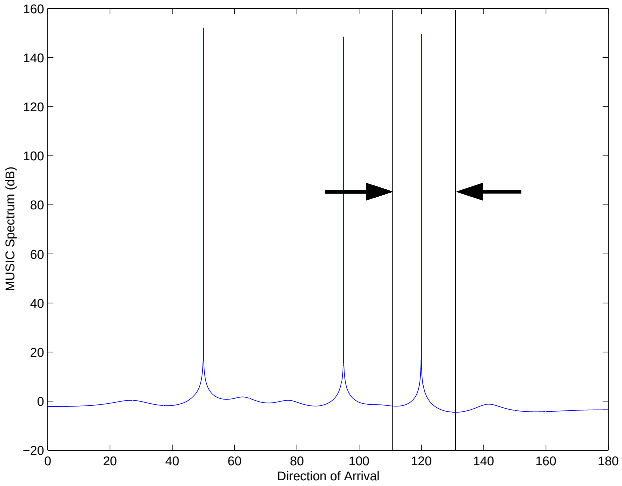

Figure 4.4: Window of 20° around the DOA 120° in the MUSIC Spectrum

For simulations of the algorithm MUSIC, the search of DOA is not performed on the whole angular spectrum $[-90°, 90°]$, but only in an angular window around the true value of targets DOA (it avoids too many false detections). This condition is legitimate: in practice, MUSIC is used as a High Resolution method, to limit the angular spectrum of search. After comparison with the performance of MUSIC, depending on the size of the angular window, the window will be made equal to 20°: MUSIC therefore tries to find a DOA in a window of 20° around the true direction of arrival, as shown for example in Fig. 4.4. Regarding the Weiss-Friedlander method, the angular spectrum will be analysed completely. This is a necessary step for the convergence of the algorithm.

Finally, the simulations must highlight the following points:

- with MUSIC: the robustness of the targets detection, introducing positioning errors in the antennas positions.
- with Weiss-Friedlander method: the robustness of the targets detection, introducing positioning errors of the antennas, checking the convergence of the algorithm toward the real DOA.

4.6 Programming of the algorithms

The program takes into account the hypothesis of simulation presented in the previous section. Nevertheless, for both programmed methods (MUSIC-Weiss and Friedlander method), the following parameters are variables and can be changed at will:

- the number of targets and their associated DOA
- the kind of errors which is added to the errors of the positions of the antennas,
- the number of realizations which are made from the random draws of the positioning errors, to mean the results of the algorithms for a given variance σ_e^2.

4.6.1 MUSIC programming

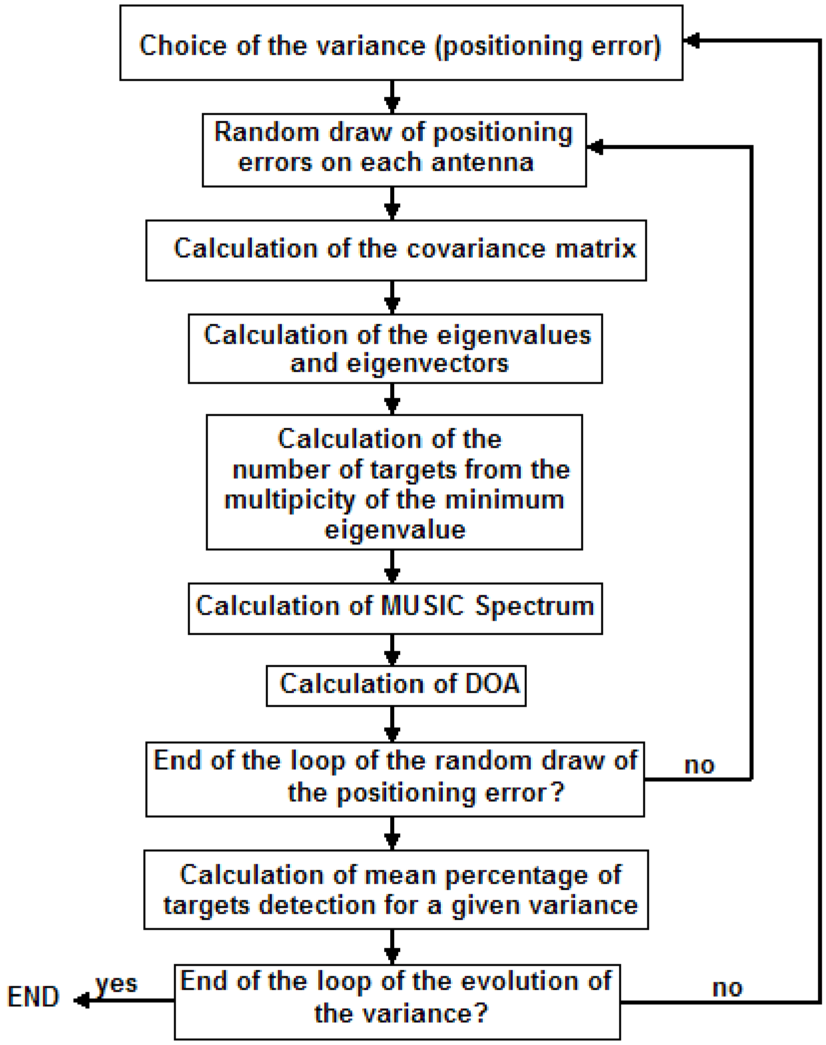

Figure 4.5: MUSIC algorithm

This program implements the MUSIC algorithm, performing several random draws of the positioning errors of the antennas (for a given variance). The functional organization chart of this method is represented in Fig. 4.5. It is presented as a graph showing of the percentage of detection of targets according to the magnitude of deformation of the receiving array (in dB) given by the relationship:

$$\Delta r = 20 \log \frac{\sigma_e}{d} \tag{4.43}$$

where Δr is the magnitude of the positioning antennas errors in the receiving array defined with σ_e^2.

4.6.2 Weiss-Friedlander programming

The programming of the Weiss-Friedlander method is the same as MUSIC, adding the double loop convergence of the estimation of the DOA and the antenna positions in the receiving array. The functional organization chart of this method is represented in Fig. 4.6.

4.7 Simulations and results

4.7.1 Performances of the MUSIC algorithm

The MUSIC algorithm obtains a spectrum on which the search of maxima results in the detection of targets and their DOA. If the detection is optimal and effective for a fixed antenna whose geometry is perfectly known, it is strongly deteriorated when the antennas position are not exactly identified. Fig. 4.7 represents the pseudo MUSIC spectrum in the case of the detection of 3 targets (with DOA equal to 50°, 95° and 120°) for an array without positioning errors, and for an array with two positioning errors (defined with a variance $\sigma_e^2 = 0.01\lambda^2$ and $\sigma_e^2 = 0.001\lambda^2$).

It is noted that the maxima with both positioning errors are far from the case without psoitioning errors and the amplitudes of the deformed array are lower: the detection of spectrum peaks is thus more difficult.

It is therefore interesting to quantify the limits of the functioning of the algorithm MUSIC, depending on the deformation of the receiving array. For this, we need to vary the magnitude of the deformation of the array (varying the variance of the normal distribution law, used to draw the random positioning errors). For each value of the variance σ^2, 200 random draws are made, to average the results. Then, we represent the evolution of detections according to the errors amplitudes, represented by Δr.

The detection of target will be considered successful if MUSIC provided a DOA estimated at $\pm 2°$ of the real DOA. When the number of target we want to detect is superior to one, detection will be considered successful if all DOA of the targets are correctly identified.

4.7.1.1 Impact on the size of windows on the detection of targets

Fig. 4.8 represents the pseudo MUSIC spectrum according Δr for different size of the window. It allows to compare the performance of MUSIC depending on the size of the observation window (for the detection of a target at 30°).

The use of a window, even if it is large (60°), significantly improves the detection capability of the algorithm. For the same purpose of detection, 4 dB in the additional deformation is tolerated. It means 0.02λ in the positioning of the antennas.

This reduction of the angular spectrum can be realized by another method which are dedicated to the DOA, as the beamforming (which is not a part of the High Resolution methods). This method has to be used before MUSIC and it would restrict the angular spectrum to a gap around the DOA which is searched.

In the following MUSIC simulations of MUSIC, the window will be equal to 20°.

4.7.1.2 Impact of the number of targets to detect

Fig. 4.9 gives the percentage of detection depending on the magnitude of deformation of the array, for a variable number of targets we want to detect. Four directions of targets were chosen at 50°, 95°, 120° and 160°. Observing the general shape of the curves, the detection of several targets is necessarily more burdensome than the detection of one for the algorithm (for $\Delta r = -20$ dB there is 70% of target detection with one target and only 15% with four targets).

To highlight this result, an example is taken. Considering floating antennas with a GPS to control their positions. The accuracy of the GPS is equal to a few meters: we assume that $\sigma_e = 3$ m. For an operating frequency $f = 10$ MHz, $\sigma_e = 3$ m corresponds to $\sigma_e = \lambda/10$ and $\Delta r = -14$ dB. So, we obtain:

- 47% for the detection of one target,
- 25% for the detection of two targets,
- 13% for the detection of three targets,
- 5% for the detection of four targets.

Considering our example, the algorithm MUSIC are reached relatively quickly. Indeed, if we want to detect a significant number of targets every time, deformations of the array must be minimal, i.e. below $\Delta r = -38$ dB for each antenna to have a detectoin of four antennas at 90%.

4.7.1.3 Detection of close targets

Fig. 4.10 shows the evolution of the detection of close targets, whose the angular gap is variable, depending on the magnitude of deformation of the receiving antenna. One case with two targets are introduced with the first target at 30° and the second target at 36°. We recall that we work with a 20-antenna array and thus its $\phi_{3dB} = 5°$.

This simulation shows that when the targets are close, the deformation of the receiving array has a degrading effect on the detection of the targets. For example, taking the example given in the previous section, at $\Delta r = -14$ dB, the number of detection is less than one target. However, if the deformation is weak (less than -30 dB), the number of detected targets is acceptable (1.8 targets).

It would appear that MUSIC is relatively robust against deformation of the array in relation to its ability to distinguish close targets. However, the MUSIC method needs some improvements to have good detection power when the targets are close and the positioning errors are large (>-30 dB).

4.7.2 Improvements with Weiss-Friedlander method

The Weiss-Friedlander algorithm is an iterative algorithm for the joint estimation of real antennas positions and targets DOA. It is usually applied as an antenna treatment when the deformations of the receiving array are small and more or less correlated between each antenna (deformations of the array in an arc for example). It is interesting, in the case of our study, to observe its behaviour with random deformation on each antenna. For example, Fig. 4.11 and Fig. 4.12 show the antennas positions estimated by this method and their real positions, for two values of the variance of the amplitude of the error $\sigma_e = 0.008\lambda$ and $\sigma_e = 0.08\lambda$.

The convergence of the algorithm is clear. The convergence of the algorithm is faster when the positioning errors are weak. However, the estimated antennas positions are slightly different from the real position.

This problem may be due to several factors:

- the method has been developed for small deformations in the receiving array. It operates a less powerfully for large deformation.
- the method was developed for correlated deformations between antennas (array deformation in an arc for example). The fact of introducing random independent errors for each antenna certainly makes the convergence of the method more difficult.
- the convergence criteria may be relative to the fitness function, the stagnation of estimated antennas positions during the iterations of the algorithm etc... The criteria we used is double: based on the fitness function and on the stagnation of the estimated antennas positions However, we have no guarantee to reach a global minimum with this criteria.

Fig. 4.13 allows to analyse the improvements of this method compared to the algorithm MUSIC. It represents the average number of targets identified in relation to these six targets (DOA equal to 30°, 60°, 80°, 100°, 130° and 160°) depending on the size of the deformation of the receiving array, and this for the algorithm MUSIC without windowing and the method Weiss-Friedlander without windowing (in its algorithmic part referring to MUSIC).

The improvements are clearly significant, especially for the deformations of the array which is between -10 dB and -32 dB, corresponding to the positioning errors from 0.025λ to 0.3λ. The Weiss-Friedlander method thus provides improvement of the performance in a range of error corresponding to our practical case (errors equal to few meters).

4.7.3 General Results of MUSIC and Weiss-Friedlander method

In the practical context of our study, we can consider positioning errors of antennas of few hundredth of λ (for example $0.1\lambda = 3$ m at $f = 10$ MHz corresponding to the GPS accuracy).

With the simulations presented in the preceding paragraph, we can emphasis the following results:

- the MUSIC algorithm, used without windowing, does not detect a target at 120° in 25% of cases at $\Delta r = -25$ dB (cf Fig. 4.8). A window of 20° can switch to 55%.
- the simultaneous detection of 4 targets (DOA equal to 50°, 95°, 120°, 160°) with MUSIC is assured in 30% of cases, having taken a window of 20° (cf Fig. 4.9).
- the Weiss-Friedlander method provides a good estimate of the antennas position defined with random errors, even if this method was first developed for errors and low correlation between receivers. The good knowledge of the position of antennas permits MUSIC to find DOA, reducing the errors of detection (cf Fig. 4.11 and Fig. 4.12).
- the simultaneous detection of 6 targets (DOA equal to 30°, 60°, 80°, 100°, 130° and 160°) is better with the method of Weiss-Friedlander: 3.8 targets will be detected versus 2.8 targets for MUSIC without windows (cf Fig. 4.13). The possibility to detect one more target is not negligible.

4.8 Conclusion of Chapter 4

The study carried out through this Chapter has analysed a few representative examples the robustness comparison of two processing algorithms aiming at detecting the direction of arrival of targets.

It appears that the MUSIC algorithm alone can not provide good performance in terms of detection. It requires an improvement in its performance, provided by two methods presented in this Chapter: imposing a windowing of 20° and the Weiss Friedlander method.

The first idea is to restrict the angular zone for research targets by MUSIC, this can be done by another method of detection, such as beamforming. The second is the Weiss Friedlander method, which improves the detection of targets over MUSIC algorithm and provides an estimate of the antennas positions of the receiving array. The latter point is very interesting as one the correction method of Chapter 3 was not robust to positioning errors.

The buoys are not free to move at will by the waves, tides and wind, failing which they drift apart from each other. Also, these buoys have a physical link (cable) between them (cf Chapter 2). Thus, the deformation of the array will no longer be completely random, but will be partially correlated.

Mechanical studies or experimentations conducted to identify the real feasibility of such systems would help to clarify the types of deformations in the receiving array and to adapt accordingly processing techniques antenna these strains for detecting DOA of targets. To validate these two last points, dynamic simulation need to be operated.

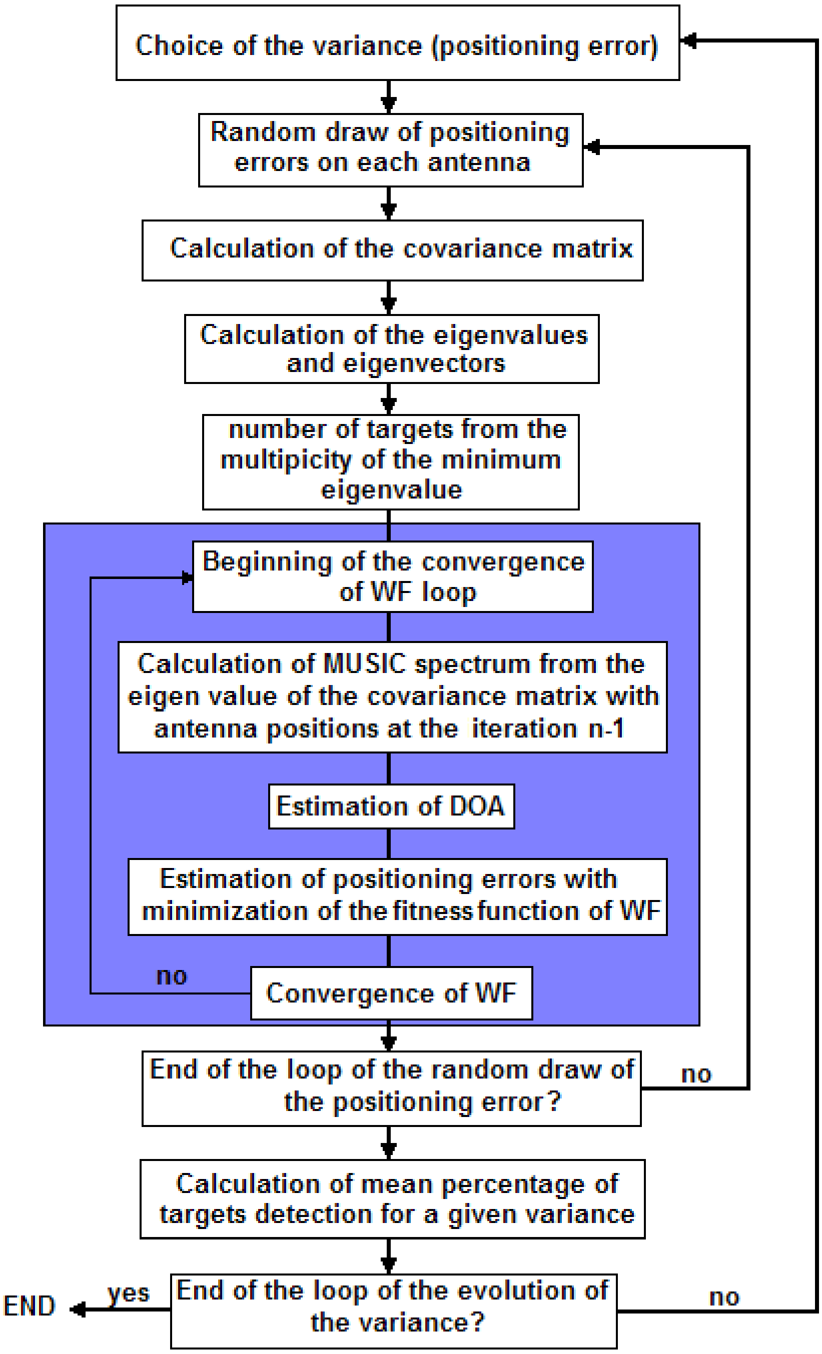

Figure 4.6: Weiss Frielander algorithm

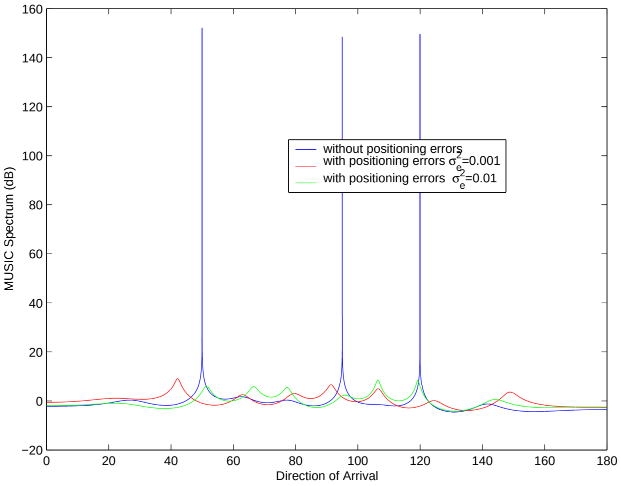

Figure 4.7: MUSIC spectrum with an array without positioning errors and with positioning errors

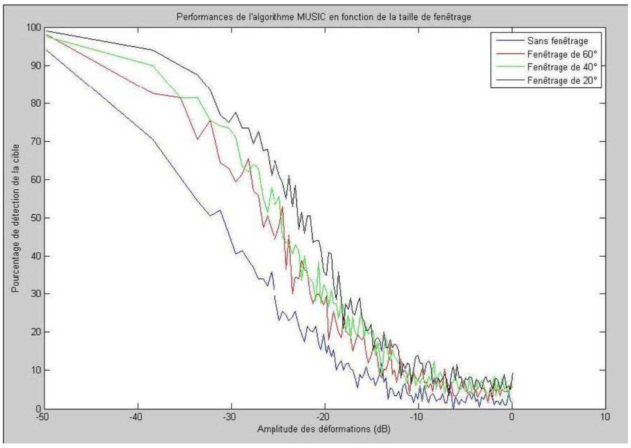

Figure 4.8: MUSIC Performance according to the size of the observation window for a target at 120°

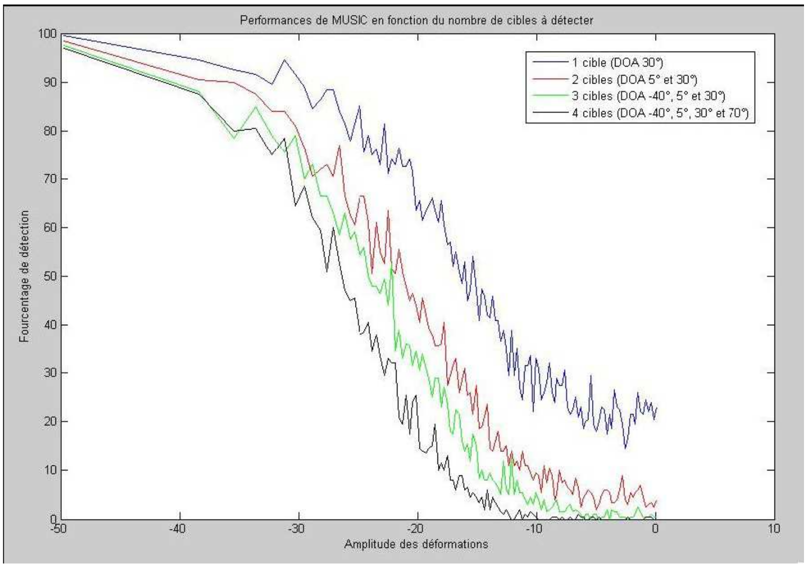

Figure 4.9: Robustness of MUSIC according to the number of targets we want to detect

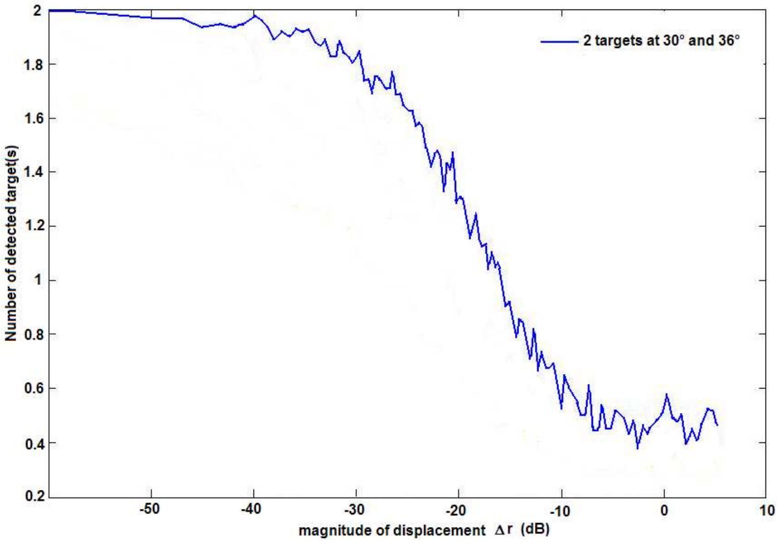

Figure 4.10: Robustness of MUSIC according to the detection of two close targets

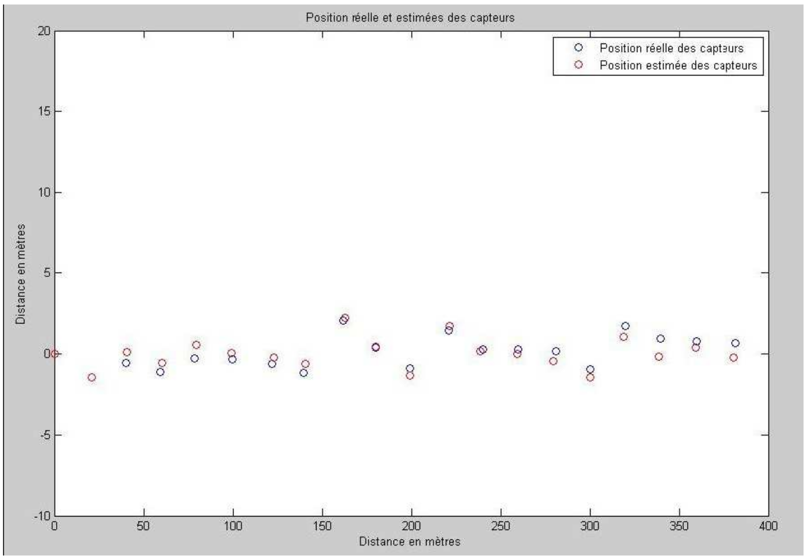

Figure 4.11: Real positions and estimated positions of antennas for a variance $\sigma_e = 0.008\lambda$

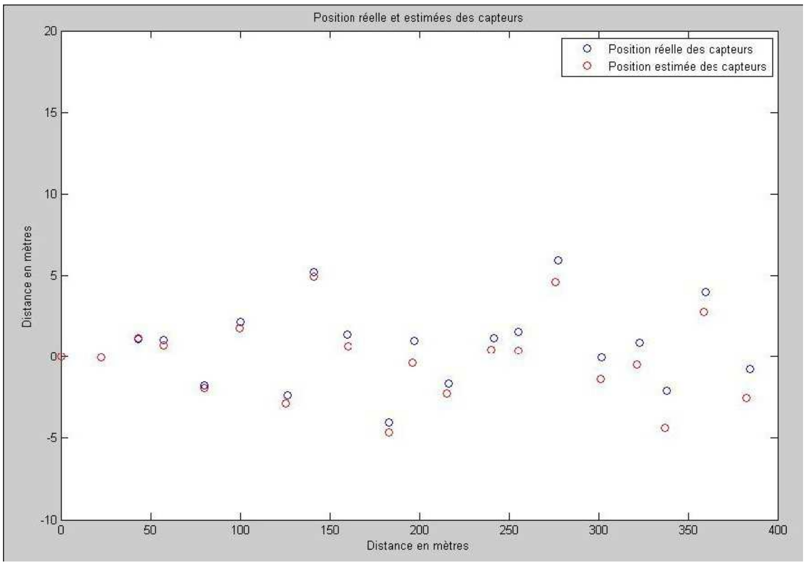

Figure 4.12: Real positions and estimated positions of antennas for a variance $\sigma_e = 0.08\lambda$

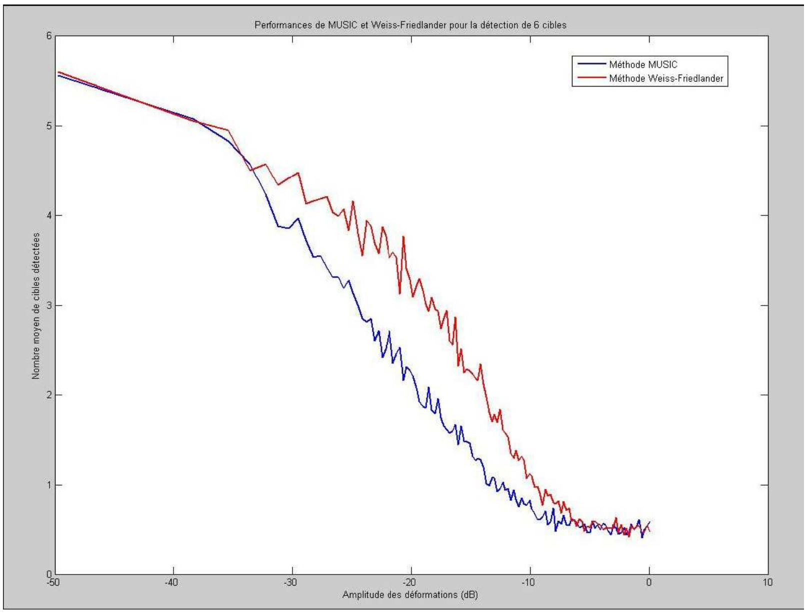

Figure 4.13: Robustness of MUSIC and Weiss Friedlander for the detection of six targets (DOA equal to 30°, 60°, 80°, 100°, 130° and 160°)

Chapter 5

Realization and measurement of a sea floating antenna

5.1 Introduction

In the previous chapters, we have seen that the movements of the buoys of the HFSWR alter the radiation pattern, resulting mainly in the increase of the SLL. We have proposed a correction method to attenuate these disturbances.

A second issue introduced by these movements relates to the modulation of the received signal on the moving antennas. In fact, the displacement of every elementary buoy on the sea surface, independently of the array deformation, generates some modulations in the received signal, introducing a spreading of the Bragg lines. As we have seen in Chapter 1, these Bragg lines determine some oceanographic parameters, such as the wind speed or the radial velocity of the surface currents. If the positions of the Bragg Lines cannot be determined with a good accuracy, it will be useless to put the antennas on buoys for oceanographic applications. In the same way, considering the monitoring of a sea area, targets are often detected by their Doppler shift. But targets can only be detected if their radial speed is different from the Doppler frequencies of the first order Bragg lines. If the Bragg lines are spread, it means that less targets could be detected.

Some theoretical studies have been carried out on this topic. Based on [37], the signal received by one buoy has been modelled in section 5.2 to give a first insight. An experimentation is then presented, with one buoy at sea. It has been conducted using an existing oceanographic radar, replacing one of the receiving antenna by a buoy.

5.2 Simulation of the spreading of the Bragg lines with a floating antenna

This section is directly inspired from [37] which presents the perspective to use a receiving array of antennas on barges. This article presents suitable results with a limited

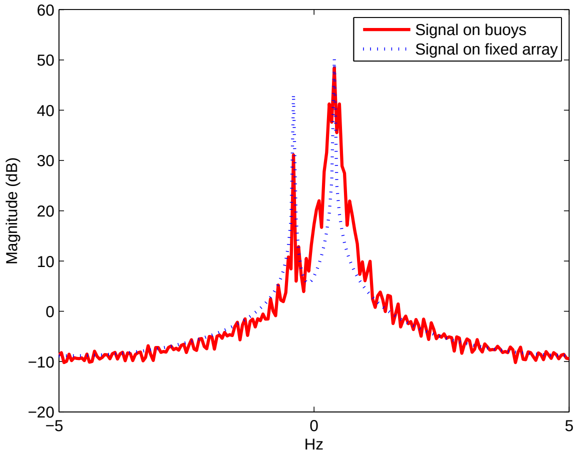

Figure 5.1: Comparison of a Doppler cut between a fixed antenna and a floating antenna.

spreading of the Bragg lines for a sea state 3.

The signal received on the floating antenna is studied taking into account the roll, the pitch and the displacement of all the antennas of the receiving array. The different degrees of freedom are defined using the modelling of the buoy movement presented in Chapter 2. The simulation was computed with a global acquisition time of 20 s, considering a pulsed radar transmitting at 15 MHz. Then, a range Doppler representation of the received signal is computed to quantify the disturbances.

Fig. 5.1 presents a cut of the range Doppler map. It compares the Bragg lines of one fixed antenna and the Bragg lines of one floating antenna. We can clearly see for the floating antenna a spreading of the positive Bragg line and a strong attenuation of the negative Bragg line. Both effects would totally alter the calculations of the corresponding oceanographic parameters. In addition, the spreading of the positive Bragg line would possibly hide some targets for the monitoring applications.

However, contrary to the modelling of the array in the previous chapters, the time evolution of the tilt angle is here the most important point defined in [37]. Obviously, it cannot be described with a fine accuracy in our model. As a consequence, we can only conclude that the disturbances generated by the roll, the pitch and the buoys displacements can strongly modify the Doppler representation and that a real measurement is needed.

The next parts of this chapter are thus focused on the experimentations we have realized with a floating antenna. They permit to quantify the disturbances generated by the movement of the sea and more particularly the spreading of the Bragg lines in real conditions.

5.3 Introduction to the experimentations

Next to the city of Porspoder in French Brittany (cf. Fig. 5.2), on the 'La Garchine' cape, the French navy hydrographic and oceanographic department (SHOM), in collaboration with the company Actimar, is operating an experimental HFSWR to measure the current in the Iroise sea. It has been in use for two years and will continue for at least two more years. It is therefore a reliable radar, allowing us to focus on the floating antenna concept. Furthermore, this experiment was conducted in collaboration with Prof Pierre Flament, from the University of Hawaii, who already knows the functioning of this particular radar. Finally, the logistic was quite easy there, there are many ports with all the necessary marine shops. The radar is a WERA system, built by Helzel messtechnik (Hamburg, Germany). It is a phased array system, in a quasi-monostatic configuration. The basic idea of this experiment was to replace one of the receiving antenna by a floating antenna (cf. Fig. 5.3). The term 'floating antenna' refers to the platform with the antenna and the other equipment. An additional long coaxial cable is used to link the floating antenna to the position of the fixed turned off antenna. This way, all the radar infrastructure can be reused.

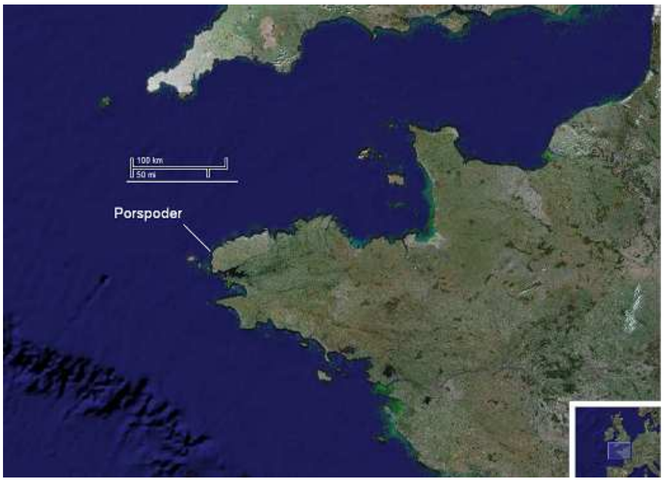

Figure 5.2: Localization of Porspoder in French Brittany

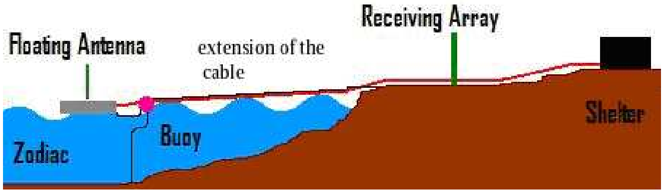

Figure 5.3: Presentation of the experimentation

5.4 WERA description

In the oceanographic domain, two oceanographic HFSWR are usually used: the first is the Costal Ocean Dynamics Applications Radar (CODAR) developed by Barrick [8]. The second one is the WERA system (WEllen RAdar) which is a shore based remote sensing phased array system, originally developped at the university of Hamburg by Klaus-Werner Gurgel et al. [15]. Both can be used to measure the ocean surface currents and the wind speed and direction. SHOM has chosen to operate a WERA.

5.4.1 Geometry of a WERA radar

Figure 5.4: Air picture of the Porspoder site

The geometry is illustrated in Fig. 5.4. The transmitting and receiving array are positioned along the coast. The radar operates in a frequency modulated continuous wave mode (FM-CW), it thus emits continuously a very low power, without any gating nor pulsing sequence. As a consequence, the receiver has to be located in a null of the transmitter to suppress the direct signal from the emitter.

A transmitting array of 4 antennas (cf. Fig. 5.5) is thus used. The shape of the array and the phases applied to the antennas form a main beam toward the sea with a zero in the orthogonal direction where the receiving array is located. Its array factor is plotted in Fig. 5.6.

Figure 5.5: Transmitting array of a WERA radar.

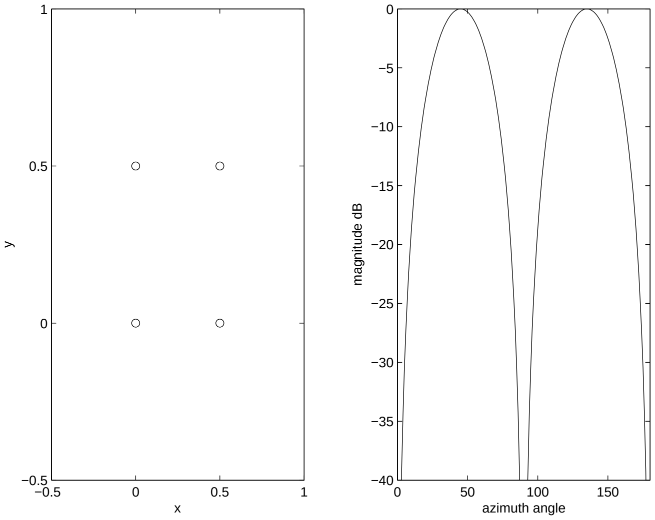

Figure 5.6: Antennas positions in wavelength of the transmitting array with its associated array factor.

The receiving array is a regular linear array of 16 antennas with half wavelength spacing. The receiver is continuously switched on. The signals from 16 antennas are processed in parallel. It has a typical azimuthal resolution of 3°.

By convention, antenna 1 is the nearest to the emitter, antenna 16 is the furthest.

The location of the floating antenna should be carefully chosen. This floating antenna will be linked by a cable to the fixed antenna it will replace. This cable should be as short as possible. Two locations are therefore possible, marked by a red dot and a white dot in Fig. 5.4. In addition, in order to suppress the direct signal, it must be located in the null of the transmit array. Only the red dot fullfills this last condition.

Consequently, the fixed antenna which will be disconnected is antenna 16 (to shorten the additional cable).

5.4.2 Shelter

The shelter houses all the electronics of the WERA (cf. Fig. 5.7), the receiving part as well as the transmitting part.

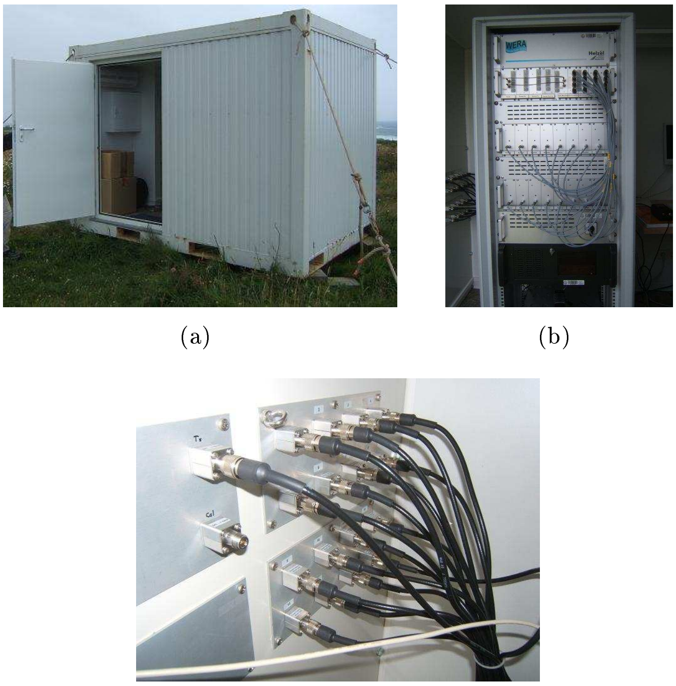

(a) (b)

(c)

Figure 5.7: Picture of the Shelter (a), acquisition system of the WERA (b) and the input of the transmitters and the outputs of the 16 receiving channels (c) which are inside the shelter

All separated received signals from the 16 antennas are digitally registered. So the signals of each antenna can be observed, independently of the others. In particular, the signal coming from the buoy will be extracted.

5.4.3 Signal Processing of WERA

The signal processing in WERA consists of the range Doppler analysis of the back scattered signals for each channel (or antenna) of the receiving array.

The range Doppler processing is illustrated in Fig. 5.8 and was explained in the first chapter. The transmitting signal is a frequency ramp. The time length for one chirp is T_r and there are N_{chirp} chirps. So, the total integration time is $T_r N_{chirp}$. The

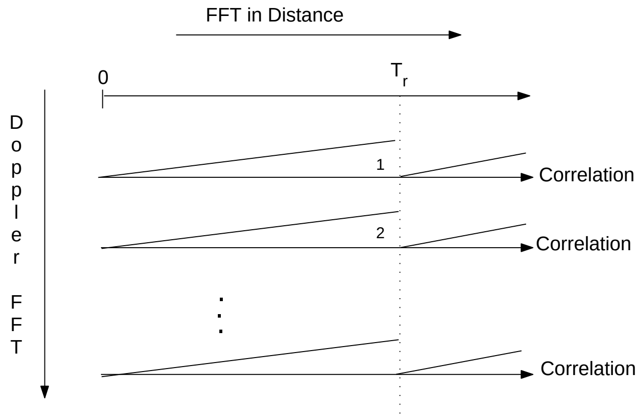

Figure 5.8: Range Doppler processing with a WERA

maximum Doppler frequency f_{max} is then:

$$f_{max} = \frac{1}{2T_r} \tag{5.1}$$

with a Doppler resolution Δf of:

$$\Delta f = \frac{1}{T_r N_{chirp}} \tag{5.2}$$

The range resolution is $\frac{c}{2B}$, with B the bandwidth of the chirp and c the celerity (cf. Chapter 1). Normally, a 100 kHz bandwidth is chosen, corresponding to a range resolution of 1.5 km. A typical work frequency is equal to 12.5 MHz. In order to observe the slow ocean parameters, the received signal is typically integrated over 10 min.

5.5 Building the floating antenna

5.5.1 Choice of the antenna

The disconnected antenna of the receiving array can not be used for the experimentation as it is too large. An active antenna is chosen instead. It is made by Rhode and Shwartz (cf. Fig. 5.9) and it is referenced “HE011 Aktivantenne” [3]. Its output power is the same as the passive antennas used in the WERA.

Figure 5.9: HE011 Rohde & Schwarz Aktivantenne

5.5.2 The floating antenna

The floating antenna is composed of two main elements, a hermetic box and a small boat.

(a)

(b)

Figure 5.10: (a) the hermetic box and (b) the zodiac.

The hermetic box protects all the electronics boarded on the floating antenna from the projections of sea water. Inside, we distinguish a GPS RTK and an inertial central (presented in the next section). The active antenna is attached outside the box (cf. Fig. 5.10(a)).

The zodiac is the platform which permits the hermetic box to float. The zodiac is not directly anchored to the seabed. A buoy is used to limit the mechanical tensions generated by the sea movement. It has to be noted that using this kind of boat as a measurement platform is not optimum because it is floating on top of the waves. Thus, it is subject to all the sea movements, even the high frequency ones.

5.5.3 The cable

A 300 m coaxial cable is used to link the floating antenna to antenna 16 in the receiving array. The first part of the cable is on the ground, between the free connector of antenna 16 and the edge of the rocks along the coast. The second part is between the rocks and the floating antenna. This last part will move with the sea elevation and the tide and it must therefore be protected. To this end, a floating electrical sheath is added. Each of the ends of the electrical sheath is filled with polyurethane foam, to prevent the sea water from entering into the sheath.

(a) (b)

Figure 5.11: The cable with its yellow sheath (a) when the sea is high (b) when the sea is low with a lot of rocks

A picture of the cable with its protection is in Fig. 5.11. We can see that the floating cable follows the sea elevation, limiting the frictions on the rocks generated by the sea movement.

5.5.4 The GPS

A GPS in RTK mode is used to know with accuracy the successive positions of the floating antenna. It is composed of two parts. The first one, called base, is fixed and is used as a reference and the second one, called mobile, is on the floating antenna. A UHF link between the base and the mobile permits to improve the accuracy of a normal GPS down to centimeter. Each part is composed of:

- a GPS antenna to receive the signals from the satellites,
- an independent battery which guarantee an autonomy of 10 hours at sea,

(a) (b)

Figure 5.12: (a) Picture of the GPS base near antenna 16 (b) Picture of the GPS module in the hermetic box of the floating antenna.

- an acquisition card,
- a VHF module for the communication between the mobile and the base.

An inertial central is used to measure the roll and the pitch of the floating antenna during the experimentation.

The next section presents the results of the first measurements

5.6 First measurements results

We will first have a look at the movements of the floating antenna in order to evaluate their magnitude.

5.6.1 Positions of the floating antenna

Fig. 5.13 shows the latitude and the longitude in degree of the floating antenna measured by the GPS RTK during all the experimentation, from the departure at the nearest beach (top right of the figure) to the return to the same beach. Fig. 5.14 is a zoom of the bottom left part of Fig. 5.13, representing the positions of the floating antenna when it is anchored during the radar acquisitions. The coordinates have been transformed to meters. The ways in (to deploy the floating antenna) and out (to bring back the floating antenna to the beach) are indicated. It clearly shows that the floating antenna has evolved in a 10m*10m square during the 4 hours of measurements.

Fig. 5.15 represents the altitude of the floating antenna. The reference time t=0h is when the GPS has been turned on on the beach before closing the hermetic box. Then, 3 hours were necessary to anchor the floating antenna and to deploy the floating cable

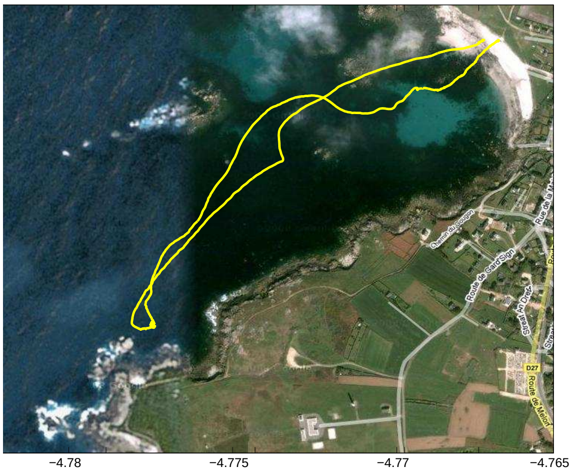

Figure 5.13: Latitude and longitude of the floating antenna during all the acquisition.

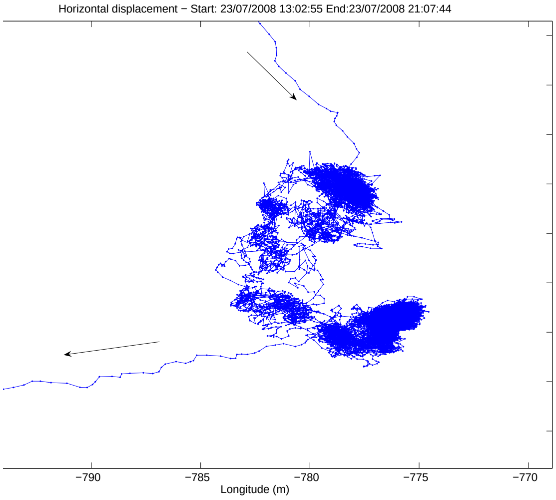

Figure 5.14: Positions of the floating antenna around its anchorage during the measurements.

for the measurement of the signal of the floating antenna. When the floating antenna was alone (after t=3h), it was no longer disturbed by a human activity, the curve becomes smooth. At the same time, we have started to record the signal. The continuous increase of the altitude of the floating antenna corresponds to the tide effect which has increased the sea elevation during the experimentation time. At the end of the recording

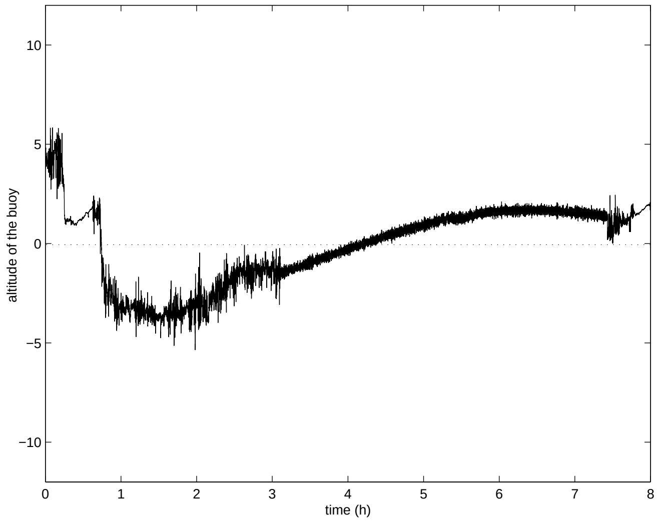

Figure 5.15: Altitude of the floating antenna in meter during all the acquisition.

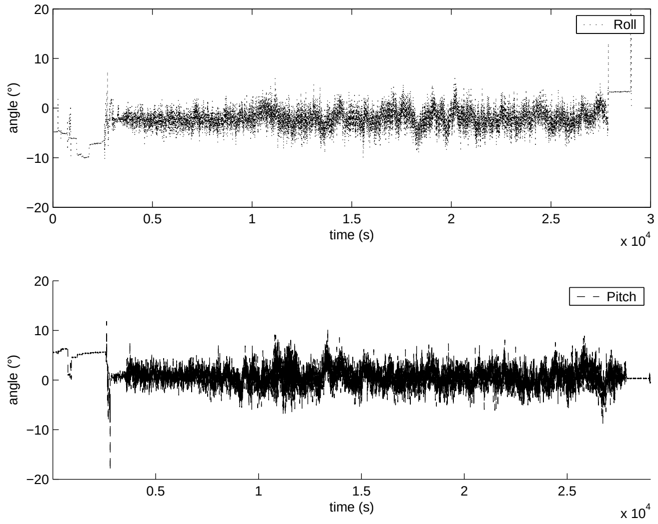

Figure 5.16: Pitch and Roll of the floating antenna

(t=7h), the curve of the altitude is no longer smooth because of the human activity to bring it back to the beach. The vertical motion during each measurement movements appears to have been very low, less than 1 meter.

In the same way, the pitch and roll were measured. Their curves are represented in Fig. 5.16. Their movements appears to be very weak, ±5°. This point is highly interesting for our problem as it implies that the modulation of the received signal should not be too strong. We can also notice that the pitch is centered around zero while the roll has a small shift, around 2°.

5.6.2 Radar measurements by the floating antenna

A first run was done with the standard parameters of the radar: 4096 chirps of 0.26s. Using Eq. 5.1 and Eq. 5.2, this corresponds to a maximum Doppler frequency f_{max} of 1.92 Hz and a Doppler resolution Δf of $9.40.10^{-4} Hz$. The central transmitting frequency was 12.48 MHz (automatically chosen by looking for a free part of the spectrum) with a bandwidth equal to 100 kHz. The 16 signals were processed as previously described. The range Doppler representation of the floating antenna is plotted in Fig. 5.18. The result of antenna 15 is also provided as a reference.

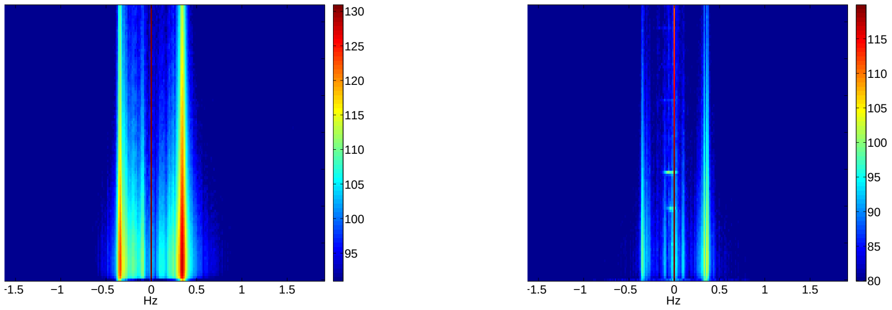

(a)

(b)

Figure 5.17: Range Doppler representation (a) of antenna 15 and (b) of the floating antenna.

A first look at the results shows that the signal of the floating antenna has a lower magnitude. As expected, we can see the first order Bragg lines and a zero Doppler component. Fig. 5.18 shows a cut at 70 km of these two results, along with the result of antenna 1. The difference in magnitude between antenna 15 and antenna 1 is also large. The signal (defined as the maximum of the negative Bragg line) to clutter (defined as the signal outside the Bragg lines) ratios of antenna 1 and of antenna 15 are roughly 25 dB while for the floating antenna it is only 15 dB. An 8-dB attenuation of the clutter between antenna 15 and antenna 1 is represented. The shelter is actually located near antenna 1, so there is some additional cable to link antenna 15 to the shelter. This explains the difference in magnitude between antenna 1 and antenna 15.

Considering the floating antenna, there is a 14-dB difference of the magnitude of the clutter with antenna 15 and a 22-dB difference of the level of the Bragg lines. Once again, the cable explains some of the difference: a 300 meters cable is used to link the position of antenna 16 to the floating antenna. This cable has an attenuation of about 12 dB (1.2 dB for 100 feets in a cable RG 213 at 30 MHz). There is also a few additionnal meters of cable between antenna 15 and antenna 16. But this does not explain the

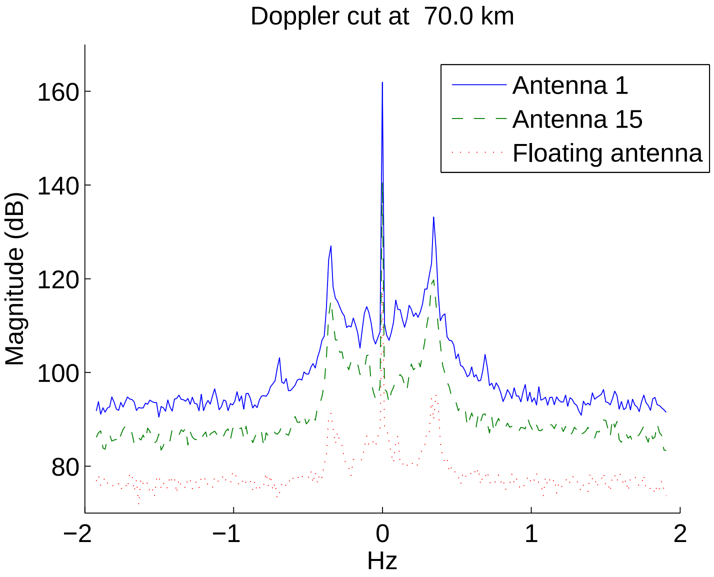

Figure 5.18: Doppler plot at 70km for antenna 1, antenna 15 and the floating antenna.

loss of signal to clutter ratio. The connections of the floating cable were not properly soldered and the edge connected to the floating antenna has been oxydized. Another possible reason we hadn't time to check is that the signal of the floating antenna might be too low for the radar, in other words the signal outside the Bragg lines is not the clutter but the radar noise.

So regarding the magnitude of the signal, the floating antenna shows some losses. But it seems to be able to correctly detect the Bragg lines. We have then normalized the signal of antenna 15 and of the floating antenna to the same reference for a thorough study of these Bragg lines. This is plotted in Fig. 5.19.

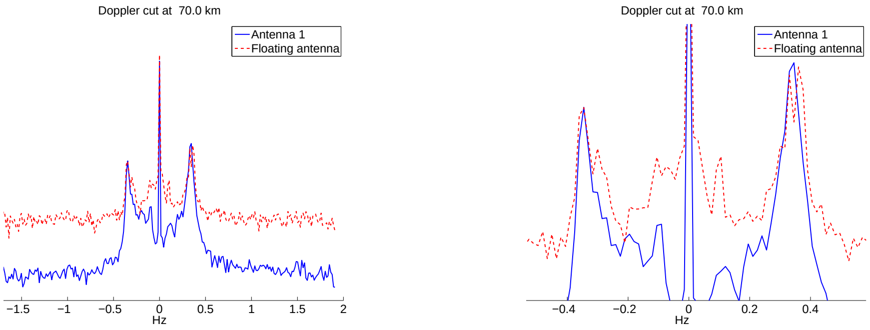

(a) (b)

Figure 5.19: (a) Normalized Doppler cut at 70 km, and (b) zoom on the first order Bragg lines.

A small spreading of these Bragg lines is visible (particularly on the negative line) but it is very limited. The positive line seems to be slightly splitted. But globally, the Bragg lines are found in both cases at $f_b = \pm 0.36$ Hz, corresponding to a frequency equals to 12.34 MHz, with roughly the same maximum. So, it appears that the floating antenna can find the correct location of the Bragg lines, along with the correct ratio of these two lines. It is therefore suitable for oceanographic applications. These Bragg lines are not broaden too much by the sea surface movements, so the floating antenna can also be used for monitoring applications. However, for the latter application, an indepth study has to be carried out on the signal to clutter ratio.

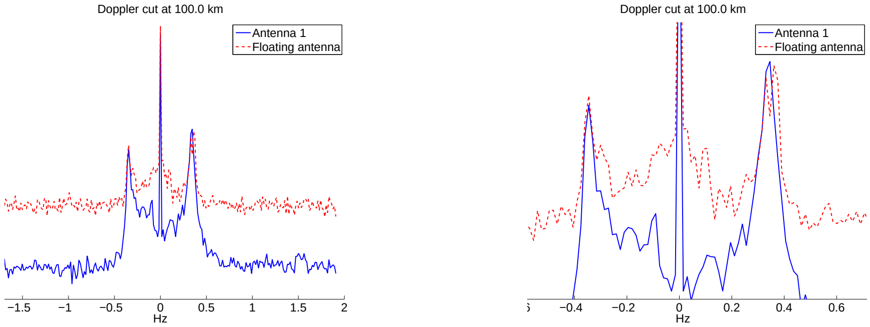

(a) (b)

Figure 5.20: (a) Normalized Doppler cut at 100 km, and (b) zoom on the first order Bragg lines.

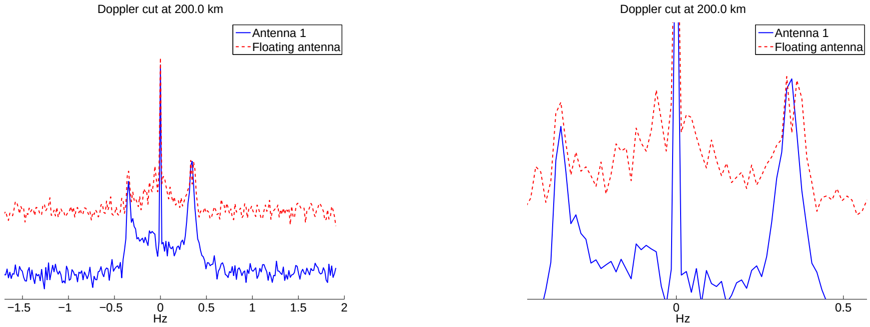

(a) (b)

Figure 5.21: (a) Normalized Doppler cut at 200 km, and (b) zoom on the first order Bragg lines.

Fig. 5.20 and Fig. 5.21 show two other cuts, at 100 km and 200 km respectively. The conclusions of the cut at 70 km also apply. It is interesting to note that the floating antenna performs still well at 200 km: although the signal to clutter ratio is only 5 dB, the Bragg lines can still be clearly identified.

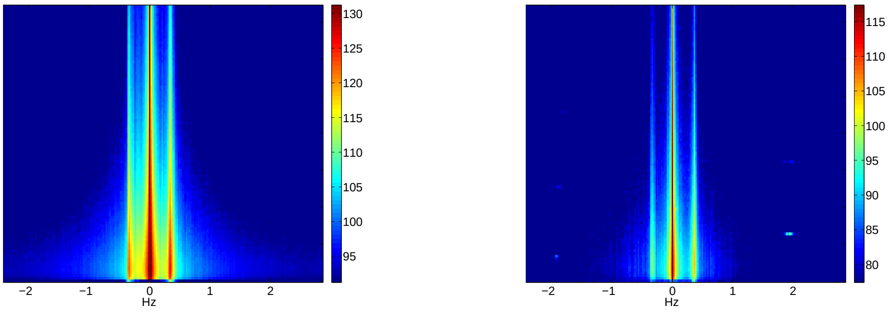

(a) (b)

Figure 5.22: For run 2, Range Doppler representation (a) of antenna 15 and (b) of the floating antenna.

Several other runs resulted in the same conclusions. In particular, the chirp length has been varied. In Fig. 5.22, the chirp length is 0.1733s. Following Eq. 5.1 and Eq. 5.2, the decrease of T_r permits to see higher Doppler frequencies $f_{max} = 2.89Hz$, but with a lower Doppler resolution $\Delta f = 1.41.10^{-3}Hz$. The Bragg lines are found at the same position.

This first measurement has validated the feasibility of the floating antenna. Measurements with stronger sea states are however needed. It will also be interesting to do them with improved platforms, such as the one on Fig. 5.23. The latter, realized during the Porspoder experimentation, is designed to cut the high frequency waves. But a heavy sea state has prevented us from putting it at sea.

(a) (b)

Figure 5.23: Floating platform and a tube of the platform which filled with polyurethane foam

5.7 Conclusion of Chapter 5

These experimentations have validated the feasibility of a sea floating antenna. A simple and cheap sea floating antenna has been realized and measured, with a calm sea. The measurements have shown that the sea floating antenna was able to correctly measure the Bragg lines and that it was thus suitable for oceanographic applications. It has also shown that the Bragg lines are only very slightly spread by the sea surface movements. The monitoring application can therefore be also envisaged. However, the signal to clutter ratio issue has to be further investigated. Other measurements with improved platforms and different sea states must be done. These future measurements have also to include the complete array of floating antennas. ——————————

Conclusion

The HFSWR is a sensor able to permanently monitor a large array, in particular the EEZ. This is true for applications ranging from the measurements of the wind to the detection of ships. This thesis has addressed the main drawback of these radars, its lack of azimuthal resolution. The large wavelength of the HF band along with the need to put the receiving array of the HFSWR near the sea surface to correctly excite the surface wave mode makes it difficult to find locations to deploy these radars. The solution investigated is to put the receiving array of a HFSWR where there is plenty of room: on the sea. Each antenna is then on a separate floating platform. However, as the sea surface movement is a highly complicated one, all the floating antennas will have some independent movements, whether one consider the horizontal, the vertical or the tilt movement. This has raised two main issues that were both addressed in this document.

The first issue has concerned the array and its associated radiation pattern. A phased array functions thanks to the addition in phase of the radiation patterns of all the elementary antennas. This can no longer work as the sea surface is continuously moving. Using a model of the movements of the buoys we have developed, we have analyzed the alteration of the radiation pattern and have presented some new corrections methods accordingly. From a physical point of view, the vertical movement introduces mainly a variation of the coupling between the elementary dipoles. This corresponds, from an analytical point of view, to a displacement away from the unit circle of the zeros of the associated polynomial. The vertical correction method thus aims at bringing these zeros back to the unit circle in order to lower the SLL while keeping a thin main beam.

The horizontal movement has the main source of disturbances in the deformation of the array, generating large increases of the SLL. The horizontal correction can be synthesized by forcing the nulls in the radiation pattern of a deformed array. The goal is to obtain the same zeros as in the initial undeformed array. Thanks to this detailed analysis, both corrections methods can be applied in serie. They give quickly a quite good result, except when the sea is too heavy.

We have then compared our correction methods to well known iterative algorithms, the GA and PSO methods. Both methods have given slightly better results, but in a very long time. They are therefore not suitable for our real time application.

The horizontal correction method uses the positions of the buoys. A robustness investigation of that method to positioning errors had thus been performed. It has shown that it requires a good knowledge of the positions of the buoys. Besides, we have also considered the robustness of a DOA algorithm, the MUSIC algorithm, to positioning errors; the same conclusion as for the horizontal correction method has been drawn. An improved version of the MUSIC algorithm, the Weiss-Friedlander method has then been studied. Through an iterative process, the latter algorithm permits to improve both the DOA estimation and the sensors positions estimation. It thus provides the positioning accuracy needed for the horizontal correction method and the DOAZ estimation.

The second issue addressed in this thesis is the modulation of the signal received on the floating antenna by the movements of the sea surface. If the Bragg lines are not at the correct positions or are attenuated, the oceanographic applications cannot be done. If the Bragg lines are spread, some targets can be hidden. Some simulations of this signal were first run but it quickly appeared that the model of the movements of the buoy we have developed was not suitable for them. Actually, for the modulation issue, the critical movement is the tilt movement, which cannot be properly rendered by our model of the movements of the buoy (it is a complicated mechanical issue).

We have therefore built a floating antenna and have measured it during a campaign at sea. We have replaced one of the receiving antennas of an existing HFSWR with our floating antenna. We were thus able to compare the measured signals of our floating antenna to a reference antenna in the same conditions. The Bragg lines were at the same Doppler frequency, with roughly the same magnitude. They were very slightly spread. So we can expect to do both oceanographic and monitoring applications.

Further work will include additional measurements in different sea states. First, the floating platform used has to be optimized: a better platform can be built to suppress the high frequency waves and thus to limit the movements of the platform. Then, an array of these floating platforms will be measured and our correction methods will be tested in real conditions.

Besides, some buoys-related sensors should be studied: towed buoys, antennas on a barge, Synthetic Aperture Radar at HF, along with their advantages/limitations. These studies will reuse the tools previously developed for the buoys studies. Then, by combining the advantages of all the HFSWR sensors configurations (fixed at coast, on buoys, on a barge, towed, SAR), a HFSWR with improved resolution could be defined.

Bibliography

[1] http://www.mathworks.fr.

[2] http://www.nec2.org.

[3] http://www.ratzer.at/pdf/he011.pdf, 2007.

[4] http://www.un.org/french/law/ los/unclos/part5.htm, 2007.

[5] http://www.shom.fr/frpage/fractoceano/vagues/vigicote/tempsreel.html, 2008.

[6] S.J. Anderson. Target classification, recognition and identification with hf radar. In *RTO SET Symposium on target identification and recognition using RF systems*, 2004.

[7] S.J. Anderson, P.J. Edwards, P. Marrone, and Y.I. Abramovitch. Investigations with secar - a bistatic hf surface wave radar. In *IEEE Radar 2003*, 2003.

[8] D. Barrick, M.W. Evans, and B.L. Weber. Ocean surface current mapped by radar. *Science 198*, 1977.

[9] D. Barrick, J.M. Headrick, and R.W. Bogle. Crombie, d.d. sea backscatter at hf: Interpretation and utilization of the echo. *Proceedings of the IEEE*, June 1974.

[10] A. Bourges, R. Guinvarc'h, B. Uguen, and R. Gillard. A simple pattern approach for deformed array on sea surface. In *Eucap*, 2006.

[11] A. Bourges, R. Guinvarc'h, B. Uguen, and R. Gillard. Swell compensation for high frequency antenna array on buoys. In *Antenna and Propagation Society*, 2006.

[12] E. Bronner. *Amélioration des performances des radars HF à ondes de surface par l'étude d'antenne compacte et filtrage adaptatif appliqué la réduction du fouillis de mer.* PhD thesis, Universitée Pierre et Marie Curie - Paris 6, 2005.

[13] R. S. Elliot. *Antenna Theory and Design.* Englewood Cliffs, NJ, Prentice Hall, 1981.

[14] T. Group. A matlab toolbox for analysis of random waves and loads. In *Lund Institute of Technology*, 2000.

[15] K.-W. Gurgel, G. Antonischti, H.-H. Essen, and T. Schlick. Wellen radar (wera): a new ground-wave hf radar for ocean remote sensing. In *Coastal Engineering*, 2000.

[16] D. E. Hasselmann, M. Dunkel, and J. A. Ewing. Directional wave spectra observed during jonswap. *Journal of Physical Oceanography*, 1980.

[17] R. L. Haupt. Unit circle representation of aperiodic arrays. *IEEE Transaction on Antennas and Propagation*, October 1995.

[18] R. L. Haupt. Particle swarm optimization in electromagnetics. *IEEE transaction on Antenna and Propagation*, February 2004.

[19] R. L. Haupt and S. E. Haupt. *Practical Genetic Algorithms*. Wiley, 2004.

[20] A. Huar. *Etude et minimisation de l'influence des phenomênes naturels sur les capacitées de détection d'un radar HF*. PhD thesis, Universitée de Rennes 1, 1999.

[21] F. Jangal. Utilisation des radars hf pour la surveillance du trafic maritime. In *Proceedings des Journées Scientifiques et Techniques du CETMEF*, 2004.

[22] C. Kerbiriou. *Developpement d'une méthode d'étalonnage d'un radar transhorizon basée sur une analyse fine du fouillis de mer*. PhD thesis, Universitée de Rennes 1, ONERA the French Aeropsace Lab, 2002.

[23] J. D. Kraus and R. J. Marhefka. *Antennas for all applications*. Mc Graw Hill Third Edition, 2002.

[24] B. Lipa and D. Barrick. Extraction of sea state from hf radar echoes : Mathematical theory and modeling. *Radio Science*, July 1986.

[25] M. Menelle. Utilisation des radars á ondes de surface pour la surveillance maritime. In *SEE OCOSS*, 2007.

[26] Institute of Marine Engineering. Eez management. In *Sciences and Technology. Proceedings of the second World Maritime Technology Conference*, 2006.

[27] W. J. Pierson and L. Moskovitz. A proposal spectrum form for fully developed wind seas based on the simulary theory of s.a. *Journal of Geophysical research*, 1964.

[28] W. J. Pierson and L. Moskowitz. A proposed spectral form for fully developped wind seas based on the similarity theory of kiataigorodkii. *Journal of Geophysical Research*, 1964.

[29] M.A. Richard. *Fundamentals of Radar Signal Processing*. Mc Graw-Hill, 2005.

[30] S. Schelkunoff. A mathematical theory of linear arrays. *Bell System Tech.*, 1943.

[31] R.O. SCHMIDT. *A Signal Subspace Approach to Multiple Source Locaiton and Spectral Estimation*. PhD thesis, Stanford University, 1981.

[32] L. Sevgi. Complex electromagnetic problems and numerical simulation approaches. In *Wiley-Interscience & IEEE Press*, 2003.

[33] L. Sevgi, A. Ponsford, and H. Huan. An integrated maritime surveillance system based on high frequency surface wave radar. *IEEE antennas and propagation Magazine*, october 2001.

[34] E.D.R. Shearman. A review of methods of remote sensing of sea-surface conditions by hf radar and design consideration for narrow-beam systems. *IEEE Journal of Oceanic Engineering*, April 1986.

[35] L. Thourel. Propagation des ondes électromagétiques. In *Ecole Nationale Supérieure de l'Aéronautique et de l'espace*, 1970.

[36] J.R. Wait. Electromagnetic wave propagation. In *John Willey & sons*, 1987.

[37] J. Wang, R. Dizaji, and A.M Ponsford. An analysis of phase array radar system on a moving platform. In *IEEE*, 2005.

[38] Weber and Barrick. On the non linear theory of gravity waves on the oceans surface. *J. Phy. ocean*, 1977.

[39] Weber and Barrick. A three-dimensionnal analysis of marine radar images for the determination of ocean waves directionality and surface currents. *Journal oF Geophysical research*, January 1985.

[40] A.J. WEISS and B. FRIEDLANDER. Array shape calibration using sources in unknown locations - a maximum likelihood approach. In *Proceedings of ICASSP*, 1988.

[41] F. Ziemer. An instrument for the survey of the directionality of ocean wave fields. In *WMO/IOC Workshop on Operational Ocean Monitoring using Surface Based Radar*, 1995.